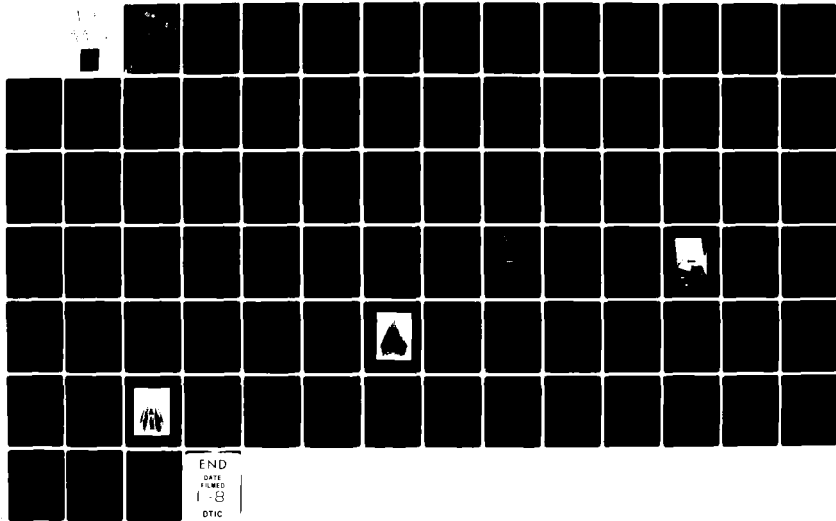


AD-A091 776 ROYAL AIRCRAFT ESTABLISHMENT FARNBOROUGH (ENGLAND) F/G 20/4  
LOW-SPEED MEASUREMENTS OF THE STATIC PRESSURE DISTRIBUTION AND --ETC(U)  
MAY 80 P J BUTTERWORTH, D G DOBNEY

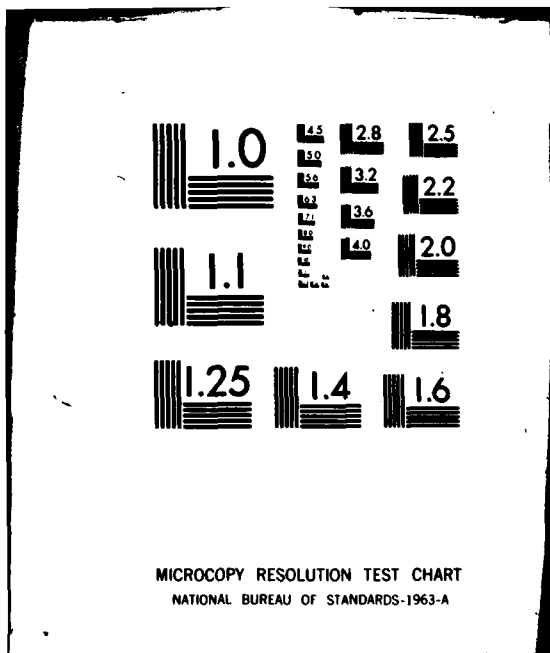
UNCLASSIFIED RAE-TR-80066

DRIC-BR-75504

NL



END  
1-8  
DTIC



AD A091776

UNLIMITED



ROYAL AIRCRAFT ESTABLISHMENT

Technical Report 60066

May 1960

DTIC  
ELECTED  
MAY 20 1960  
S C D

LOW-SPEED MEASUREMENTS OF THE  
STATIC PRESSURE DISTRIBUTION AND  
OVERALL FORCES ON A CAMBERED AND  
A SYMMETRIC MILD GOTHIc WING  
OF ASPECT RATIO 1.4

by

P.J. Butterworth

D.G. Dobney

Research Department, Ministry of Defence

Farnborough, Hants

UNLIMITED

UDC 533.693.3 : 533.6.043.1 : 533.6.013.67 : 533.6.082.3

(18) DTIC

(19) BR-7504

ROYAL AIRCRAFT ESTABLISHMENT

(9) Technical Report 80066 ✓

Received for printing 22 May 1980

(14) RAE-TR-84011

LOW-SPEED MEASUREMENTS OF THE STATIC PRESSURE DISTRIBUTION AND OVERALL FORCES  
ON A CAMBERED AND A SYMMETRIC MILD GOTHIC WING OF ASPECT RATIO 1.4.

by

(10) P. J. Butterworth  
D. G. Dobney

(11) May 80

(12) 80

SUMMARY

A cambered wing of aspect ratio 1.4 has been tested in a low-speed wind tunnel to determine its surface static pressure distribution at its designed, attached-flow incidence for comparison with the theoretical loading.

To enable the effects of camber on the separated-flow characteristics of this planform to be isolated, the corresponding symmetric wing was also included in the test programme and the results for the two wings are compared and empirical relationships found.

The lift, drag and pitching moment characteristics of each wing have also been measured over a range of Reynolds number for comparison with the results of the earlier force tests and those derived by integration of the measured pressure distributions.

Departmental Reference: Aero 3482

Copyright  
©  
Controller HMSO London  
1980

Accession For

FTIS ST&I  
DTIC T-3  
Unannounced

Justification

By \_\_\_\_\_  
Distribution/  
Availability Codes \_\_\_\_\_  
Avail and/or  
Dist Special

A

310450

5c A

LIST OF CONTENTS

	<u>Page</u>
1      INTRODUCTION	3
2      DESCRIPTION OF EXPERIMENTS	5
2.1 Model details	5
2.2 Test conditions and data reduction	7
3      ANALYSIS OF OVERALL FORCE MEASUREMENTS	8
3.1 Lift and normal force	8
3.2 Drag	10
3.3 Pitching moment	11
4      ANALYSIS OF PRESSURE MEASUREMENTS AT THE ATTACHMENT INCIDENCE	13
5      ANALYSIS OF PRESSURE MEASUREMENTS WITH SEPARATED FLOW	15
5.1 General details of flow	15
5.2 Local normal force	16
5.3 Vortex characteristics	19
6      CONCLUSIONS	22
Appendix A Detailed description of the models	25
Appendix B Correction of results for support interference	27
Appendix C Description of the pressure measurement system	32
Tables 1 to 8	33
List of symbols	45
References	47
Illustrations	Figures 1-33 inside back cover
Report documentation page	

## 1 INTRODUCTION

Putting arbitrary camber on a sharp-edged slender wing results, at low incidence, in vortex separations occurring on both surfaces of the wing from different parts of the leading edge. If, however, the camber surface is designed so that the flow is attached all along the leading edge at same angle of incidence then at incidences above and below this an orderly pattern of vortices exists on only one surface of the wing. This leads to lower drag and better controlled movement of the centre of pressure than would be observed on the wing with arbitrary camber. Furthermore the drag at a given value of lift is in general less than for the plane wing of the same planform.

Davies has developed a linear method<sup>1</sup> for the design of such camber surfaces in subsonic flow. In this method the camber surface and its angle of incidence for attached flow are derived from a specified loading distribution for attached leading-edge flow which has the correct form near the edges of the planform. Suitable loading distributions can be linearly combined to produce different camber shapes and Davies shows several examples (of a mild gothic planform) having different design lift coefficients and centres of pressure. Some of these surfaces (designed for lift coefficients of 0.1 and 0.2) with thickness added have been tested over a range of Reynolds and Mach numbers at RAE Farnborough<sup>2</sup>. Although attached flow appeared to be achieved very close to the design incidence and lift coefficient, there was a discrepancy between the theoretical and experimental centres of pressure of about 3% of the centreline chord. It was not clear whether the cause was primarily inviscid (arising from the assumptions involved in the linearisation) or viscous (arising from the displacement effects of the boundary layer).

Intuitively it seems likely that the camber surface which generates least drag at a low lift coefficient (*eg* aircraft cruise) will be different from that which minimises the drag at higher values of lift coefficient (*eg* take-off). Indeed both theoretical<sup>3</sup> and experimental<sup>4</sup> work suggest that the minimum value of the lift-dependent drag factor (K) of a cambered slender wing occurs at a lift coefficient about double the attached-flow value. This is because the suction induced by the leading-edge vortices not only produce a nonlinear increase in lift but also, on a cambered wing with forward facing surfaces, produce a significant forward thrust - thus reducing the drag. Hence whether he wishes to predict the performance around a likely optimum operating condition or to make the best compromise between the conflicting requirements of high- and low-speed flight for a slender wing with fixed geometry, the designer needs

information about the development of leading-edge vortices on cambered slender wings. The spanwise position and intensity of the suctions induced by the leading-edge vortices are also important for structural design.

For these reasons one cambered and one symmetric wing of mild gothic planform have been tested in the No.2 11½ ft × 8½ ft low-speed wind tunnel at RAE Farnborough. The shape chosen for the cambered wing was the same as that on which previous force measurements<sup>2</sup> had been made at various Reynolds and Mach numbers. The shape of the symmetric model had also been tested but only at the lowest Reynolds number<sup>2</sup>. These two models were provided with a large number of surface pressure tappings so that the static pressure distributions (and hence loading distributions) could be determined at both design and off-design conditions.

The combined effect of the strut mounting system and the mean inclination of the tunnel airflow on the pressure distributions was evaluated by analysis of the pressure distribution on the symmetric wing at zero angle of incidence and this was obviously an important factor in making a detailed comparison between the theoretical and experimentally measured loadings at the design incidence of the cambered wing.

The objectives of this experiment, then, were as follows:

- (i) to obtain further evidence of the drag reductions which can be obtained by the use of camber at a higher Reynolds number than had been achieved before;
- (ii) to make a detailed comparison between the theoretical and experimental loading distributions at the attached-flow incidence and explore the reasons for any discrepancies;
- (iii) to examine the differences in development of the leading-edge vortices on cambered and symmetric slender wings in the hope that this might lead to improved methods of predicting the performance of cambered slender wings over a range of lift coefficients, and
- (iv) to use the symmetric model and a dummy strut and fairing to determine the corrections that needed to be applied to account for support interference and flow misalignment in the tunnel so that the comparison to be made in (ii) is valid.

## 2 DESCRIPTION OF EXPERIMENTS

### 2.1 Model details

The mild gothic planform and centreline thickness distribution of the models are shown in Fig 1 and defined in Table 1.

The design of the cambered wing<sup>1</sup> begins with the specification of a non-zero loading distribution which is suitable for attached flow all along the leading edges. (This loading distribution has to tend to zero at the leading and trailing edges of the planform as the square root of the distance from the edge.) Integration of this loading distribution yields the design lift coefficient ( $C_{L_{des}}$ ) and the centre of pressure position ( $(x_{cp})_{des}$ ); the values of these for the selected loading distribution are 0.1 and 0.533c respectively.

The local slope of the camber surface is derived from the loading distribution and hence the surface shape is obtained by integration and specification of a straight trailing edge. For the design (attached-flow) condition the angle of incidence ( $\alpha_{des}$ ) of the line joining the apex to the centre of the trailing edge is 5.32°. Since the loading distribution is specified in the x-y plane, the centreline chord and area of the cambered wing are greater than those of the planform by a factor sec 5.32° (see Table 1). The symmetric wing can be thought of in this notation as a cambered wing for which  $C_{L_{des}} = 0.0$  at an attached-flow incidence  $\alpha_{des} = 0.0^\circ$ . This is the way it will be treated in this Report.

The thickness distribution is added normal to the camber surface<sup>1</sup> and typical spanwise sections of the two wings are shown in Fig 2. Fig 3 shows the cambered wing mounted in the tunnel. A detailed description of the construction of the models and the test procedure is given in Appendix A.

There is, however, one aspect of the arrangement of the pressure plotting holes which it is important to note here: the pressure plotting holes on the symmetric wing are located at the same values of x/c on both upper and lower surfaces - in other words, one above the other at the design incidence. The pressure difference between them gives the local loading:

$$\lambda(n) = C_{p_L} - C_{p_U}$$

where  $C_{p_U}$  = pressure coefficient on the upper surface

and  $C_{p_L}$  = pressure coefficient on the lower surface.

Hence following the idea expressed earlier in this section, the pressure holes on the cambered wing were also drilled so as to be one above the other at the design incidence of  $5.32^\circ$ . Integration of the pressure distribution at the design incidence then leads directly to the evaluation of the lift coefficient - a value which we want to compare with the theoretical value of 0.1.

If we define the local loading  $\lambda(n)$  as above for each wing, then we may further define the local normal force coefficient:

$$c_{N(c)}\left(\frac{x}{c}\right) = \frac{1}{2} \int_{-1}^{+1} \lambda(n) dn ,$$

the overall normal force coefficient:

$$\bar{c}_N = \frac{2sc}{S} \int_0^1 \left\{ \frac{s(x/c)}{s} c_{N(c)}\left(\frac{x}{c}\right) \right\} d\left(\frac{x}{c}\right)$$

and the chordwise position of the centre of pressure:

$$\frac{x_{cp}}{c} = \frac{c_{m_{apex}}}{\bar{c}_N} = \frac{\int_0^1 \left\{ \frac{x}{c} \frac{s(x/c)}{s} c_{N(c)}\left(\frac{x}{c}\right) \right\} d\left(\frac{x}{c}\right)}{\int_0^1 \left\{ \frac{s(x/c)}{s} c_{N(c)}\left(\frac{x}{c}\right) \right\} d\left(\frac{x}{c}\right)} .$$

Defining in this way means that:

$$\bar{c}_N = c_L \text{ at the design incidence for both wings,}$$

and more generally:

$$\bar{c}_N = c_L \cos(\alpha - \alpha_{des}) + c_D \sin(\alpha - \alpha_{des})$$

thus producing a framework within which results from both the cambered and symmetric wings can be compared on a unified basis. The more usual definition of overall normal force coefficient is:

$$\bar{c}_N = c_L \cos \alpha + c_D \sin \alpha$$

and for a cambered wing this is clearly dependent upon the datum which is chosen to determine the model incidence. The definition of the incidence datum which is used in this Report (the line joining the centre of the trailing edge to the apex) is the same for both the cambered and symmetric wings.

## 2.2 Test conditions and data reduction

For both wings, lift, drag and pitching moment were measured at speeds of 76, 46 and  $22.6 \text{ m s}^{-1}$  giving Reynolds numbers of  $6.7 \times 10^6$ ,  $4.0 \times 10^6$  and  $2.0 \times 10^6$  based on the planform centreline chord. The measurements were made over incidence ranges of  $-5^\circ$  to  $20^\circ$  for the symmetric wing and  $0^\circ$  to  $25^\circ$  for the cambered wing; they were taken basically at  $1^\circ$  intervals but with extra intermediate points for  $5^\circ$  either side of the design incidence at the highest wind speed. All these measurements were reduced to coefficient form<sup>5</sup> and were corrected for;

- (i) the wind tunnel boundaries using established methods<sup>6</sup>,
- (ii) the tare loads of the support system measured in the absence of the model, and
- (iii) the interference effects of the strut mounting system on the model.

The interference effects of the strut mounting system were determined, as described in Appendix B, from tests on the models upright, inverted and inverted with a dummy strut (see Fig 4). These corrections are given in Table 2 and the fully corrected results are given in Tables 3 to 5 for both wings.

At the highest Reynolds number,  $R = 6.7 \times 10^6$ , pressure measurements were made at the incidences given in Table 6 using the system described in Appendix C. These measurements were reduced to coefficient form using a standard method<sup>7</sup> and the pressure distributions were integrated using a planimeter to give  $C_N(x/c)$ . A successful computer programme<sup>8</sup> for performing this integration has been developed but at the time of this analysis it did not operate adequately.

Since one of the objectives of this experiment is a comparison between experimental and theoretical loading distributions on the cambered wing, it was particularly important to remove, from the measurements of pressure, the interference effects of the model support system and of any non-uniformities in the wind tunnel flow. This was achieved by consideration of the pressure distribution on the symmetric wing as described in Appendix B.

The correction procedure is described in detail partly because it is so important to the conclusions and partly because the corrections were large and affected a larger area of the slender wings than had been anticipated considering the size of the strut. In an attempt to reduce the locally high velocities at the sides of the circular main strut, some fairings were made to fit around the strut/model junction giving an aerofoil shape of 30% t/c. These were tested at various incidences, but their use was abandoned because flow visualisation and pressure measurement showed that the area of the model affected by the flow around the faired strut was larger, even though the magnitude of the interference close to it was reduced.

### 3 ANALYSIS OF OVERALL FORCE MEASUREMENTS

#### 3.1 Lift and normal force

Fig 5 shows a comparison of the  $C_L \sim \alpha$  curves with those from previous tests<sup>2</sup>. The results at the two highest Reynolds numbers agree very well but the results at the lowest Reynolds number lie below these at the higher incidences. The comparison with the previous results<sup>2</sup> ( $R = 2 \times 10^6$ ) is good for the cambered wing but there are slight differences between the results for the symmetric wing.

For the cambered wing, the experimental values of  $C_L$  at  $\alpha = 5.32^\circ$  (written  $(C_L)_{\alpha_{des}}$  and given in Table 7) are very close to the theoretical value of 0.1. Using the values of  $(C_L)_{\alpha_{des}}$  given in Table 7, it is possible to compare the separated-flow characteristics of the cambered and symmetric wings as shown in Fig 6 for the highest Reynolds number tests ( $R = 6.7 \times 10^6$ ). The maximum difference in  $[C_L - (C_L)_{\alpha_{des}}]$  between the results for the two wings is approximately 5% and is most noticeable in the region  $10^\circ < [\alpha - \alpha_{des}] < 15^\circ$ . This is the incidence range in which vortex breakdown affects the wings (see below and section 5.3) and it occurs at a lower value of  $[\alpha - \alpha_{des}]$  on the cambered wing than on the symmetric. This result agrees well with the results of Ref 2.

To examine this loss of lift in detail, it is most convenient to consider the normal force characteristic ( $\bar{C}_N$ ) and split it into its linear and nonlinear components<sup>9</sup>, ie

$$\bar{C}_N - (\bar{C}_N)_{\alpha_{des}} = \bar{C}_{N_{\text{linear}}} + \bar{C}_{N_{\text{nonlinear}}} = a(\alpha - \alpha_{des}) + \bar{C}_{N_{nl}} .$$

96

Division by  $(\alpha - \alpha_{des})$  gives:

$$\frac{\bar{C}_N - (\bar{C}_N)_{\alpha_{des}}}{(\alpha - \alpha_{des})} = a + \frac{\bar{C}_N_{nl}}{(\alpha - \alpha_{des})}$$

where 'a' is determined by the limiting value of

$$\frac{\bar{C}_N - (\bar{C}_N)_{\alpha_{des}}}{\alpha - \alpha_{des}}$$

as  $\alpha$  tends to  $\alpha_{des}$ . Because of experimental scatter, there is always some uncertainty in the evaluation of 'a'. For a cambered wing, the determination of 'a' is further complicated by the accuracy of determination of  $(\bar{C}_N)_{\alpha_{des}}$ . Despite these potential errors, some variation of

$$\frac{\bar{C}_N - (\bar{C}_N)_{\alpha_{des}}}{\alpha - \alpha_{des}}$$

with Reynolds number can be seen in Fig 7.

Ignoring, for the moment, the kinks at values of  $(\alpha - \alpha_{des}) \approx 3^\circ$  in some of the curves, there is a tendency for the value of 'a' to increase with Reynolds number. For  $(\alpha - \alpha_{des}) < 10^\circ$  the slope of the lines (which is obviously related to  $\bar{C}_N_{nl}$ ) also increases with Reynolds number. Vortex breakdown causes an inflection of the curves near  $13.5^\circ$  for the symmetric wing and  $16.5^\circ$  for the cambered wing at the highest Reynolds number. With decreasing  $R$ , this inflection becomes less severe but occurs at a lower value of  $\alpha$ . As vortex breakdown is also associated with the nonlinear lift, it appears that both the linear and nonlinear components of  $\bar{C}_N$  are slightly Reynolds-number dependent.

The cause of the kink in some of the curves at low incidences is unknown and whilst it has been observed previously on thick wings<sup>10</sup> and on a thinner cambered wing with and without bodies<sup>11</sup> it is not evident in the results of Ref 2. Although the kink appears quite large relative to the extrapolated (straight) curve shown dotted in Fig 7, in terms of  $\bar{C}_N$  it is less than 0.004 (see inset on Fig 7). Without further evidence, this kink must be attributed to some flow condition which is caused possibly by increasing Reynolds number (transition effects) and/or surface curvature (since it occurs at all speeds on the cambered wing).

### 3.2 Drag

On slender wing models without roughness bands for artificially fixing boundary layer transition, laminar flow can exist over a range of incidence around the attachment condition<sup>10</sup>. When this happens, the drag polars clearly exhibit a laminar drag bucket which is unlikely to occur at full scale Reynolds number. The existence of this drag bucket introduces complications into the analysis of drag. Hence for this task it is important to consider only results for which boundary layer transition has been artificially fixed. At the two highest Reynolds numbers ( $R = 6.7 \times 10^6$  and  $4.0 \times 10^6$ ) the adhesive tape covering the surface static pressure tappings ensured transition was fixed but at the lowest Reynolds number ( $R = 2.0 \times 10^6$ ) extra roughness was required (see Appendix A).

The drag polars are plotted in Fig 8 with, for comparison, results from Ref 2. The inset on this figure shows that (for  $R = 6.7 \times 10^6$ )  $C_D$  for the cambered wing is less than for the symmetric wing for values of  $C_L > 0.065$  and at the design value of  $C_L (= 0.1)$  the reduction is about 8%. As  $C_L$  increases to 1.0, the reduction in  $C_D$  decreases to approximately 5%.

If we define a lift-dependent drag factor:

$$K = \frac{\pi A (C_D - C_{D_0})}{C_L^2}$$

(where  $C_{D_0}$  is the minimum value of  $C_D$  for the symmetric wing\*). This may be used to characterise the reduction in drag that can be achieved by the use of camber.  $K$  is plotted against  $C_L$  in Fig 9. Fig 9a compares the two sets of results for which extra roughness was required to fix transition ( $R = 2.0 \times 10^6$  and Ref 2). Fig 9b compares the results of the tests at the three Reynolds numbers. Despite detailed differences in the curves for the cambered or symmetric wing, the dominant feature is the large reductions in  $K$  evident for the cambered wing.

For the cambered wing at  $R = 2.0 \times 10^6$ ,  $K$  has a minimum value near  $C_L = 0.2$  (ie double the design value of  $C_L$  - see Refs 3 and 4) and in this respect agrees well with the results of Ref 2. However, this minimum occurs at  $C_L \approx 0.3$  at  $R = 4.0 \times 10^6$  and is virtually non-existent at  $R = 6.7 \times 10^6$ ; at this highest Reynolds number the value of  $K$  continues to fall until at the

\* A method for determining  $C_{D_0}$  is given in the Appendix to Ref 12 and the values deduced in this way for the present results are given in Tables 3 to 5.

attachment value of  $C_L$  of 0.1 K attains the theoretical attached-flow value of 1.1<sup>1,13</sup>. Whilst this may appear inconsistent, since it does not agree with any other tests on this wing shape<sup>2</sup>, values of  $K = 1.1$  have been obtained on an aspect ratio 2.0 wing with the same camber distribution as this wing<sup>11</sup> at  $R = 1.7 \times 10^6$ .

The percentage reductions in K achieved by the cambered wing are shown in Fig 10. For  $C_L > 0.6$  (ie after vortex breakdown) the agreement between the different sets of results is good but at lower values of  $C_L$  smaller reductions in K are obtained at the lowest Reynolds number and wind speed ( $R = 2.0 \times 10^6$ ,  $V = 22.6 \text{ m s}^{-1}$ ). The cause of this must be attributed to the roughness bands, used to fix transition, affecting the development of the leading-edge vortices. This is not incompatible with the better correlation after vortex breakdown when peak suctions on the wing surface are reduced and distributed over a larger proportion of the local span (see section 5.3).

Using K as defined, Figs 9 and 10 indicate performance gains for the cambered wing in relation to the symmetric wing but this definition of K does not show whether they are primarily due to a shift of the minimum point of the drag polar of the cambered wing or to a change of shape of the polar. To see this, it is necessary to consider an alternate definition of a lift-dependent drag factor for a cambered wing which is analogous to K for a symmetric wing, namely:

$$K' = \pi A (C_D - C_{Dm}) / (C_L - C_{Lm})^2$$

where  $(C_{Lm}, C_{Dm})$  defines the minimum point of the drag polar of the cambered wing\*. (For a symmetric wing,  $K' = K$  since  $C_{Lm} = 0$  and  $C_{Dm} = C_{D0}$ .)  $K'$  is plotted against  $(C_L - C_{Lm})$  in Fig 11 which shows that at  $R = 6.7 \times 10^6$  the cambered wing gives values of  $K'$  up to 5% higher than those of the symmetric wing. So despite higher values of  $K'$ , the cambered wing achieves the performance gains shown in Fig 8 because of the favourable shift of the minimum point of its drag polar.

### 3.3 Pitching moment

The reference point for the pitching moments is on the line joining the apex to the centre of the trailing edge 0.54c from the apex. (This is physically

---

\* A method for determining  $C_{Lm}$  and  $C_{Dm}$  is given in the Appendix to Ref 12 and the values obtained in this way for the present tests are shown in Tables 3 to 5.

the same point as the model pivot point.) The moments are non-dimensionalised with respect to the wing area and centreline chord.

It was estimated from previous work on the effects of planform<sup>9</sup> and thickness<sup>10</sup> that for the symmetric wing at zero incidence, the aerodynamic centre would be 0.533c downstream of the apex and this point was chosen for the design centre of pressure position of the cambered wing. At the design condition where  $C_L = 0.1$ , the theoretical value of  $C_m$  (about 0.54c) is therefore 0.0007.

$C_m$  is plotted against  $C_L$  in Fig 12a for the symmetric wing and in Fig 12b for the cambered wing. This latter figure shows that the theoretical value of  $C_m$  at  $C_{L_{des}}$  is substantially lower than the experimental value. This discrepancy represents a difference of 3% centreline chord between the theoretical and experimental centres of pressure and is one of the reasons for the present investigation of the attached-flow loading distribution on the cambered wing.

For the symmetric wing, the results for  $R = 2.0 \times 10^6$  show a marked reduction in static stability margin compared with those at higher Reynolds numbers but the results for the cambered wing do not show a similar reduction. Below their respective attachment conditions (ie  $C_L = 0$  for the symmetric wing and  $C_L = 0.1$  for the cambered wing) both wings show a reduction in  $C_m$  at  $R = 4.0 \times 10^6$ . Although no transition effects on  $C_L$  or  $C_D$  are noticeable at this Reynolds number, the effect on the cambered wing is similar to that shown in previous tests<sup>2</sup>. These showed that with free transition, a laminar separation occurs on the upper surface of the cambered wing aft of the region of maximum wing thickness. The comparable behaviour of both wings in the present tests suggests that on the symmetric wing a separation occurs on the upper surface but not on the lower, possibly due to the presence of the strut mounting system. This means that at  $R = 4.0 \times 10^6$  the strips of adhesive tape covering the surface static pressure measurement holes were not as effective in fixing transition below the design incidence as had been assumed.

The kinks in the  $C_m$  curves at values of  $C_L$  in the range 0.5 to 0.6 are caused by a loss in loading near the trailing edge as the breakdown of the leading-edge vortices moves upstream (see section 5.3).

The locus of the centre of pressure is not presented here since the results at the three wind speeds are practically indistinguishable but for  $R = 6.7 \times 10^6$  a comparison of the results from force and pressure tests is shown in Fig 24.

#### 4 ANALYSIS OF PRESSURE MEASUREMENTS AT THE ATTACHMENT INCIDENCE

The flow visualisation tests in Ref 2 showed that at the theoretical attached flow incidence of  $5.32^\circ$ , the flow was attached along the leading edges on both surfaces of the cambered wing. Fig 13 shows that in the present investigation (for  $R = 4.0 \times 10^6$ ) the flow is attached on the upper surface of the model. The analysis of this section assumes that the flow is attached along the leading edges on both surfaces at the design incidence of  $5.32^\circ$ .

Fig 14 shows, in isobar form, the theoretical loading distribution; the corresponding experimentally determined distribution is shown in Fig 15. This shows clearly that the local loading near the apex is greater than the design distribution whilst the loading near the trailing edge is less. The discussion in this section is aimed at establishing the origin of these discrepancies. To this end the experimental measurements have been compared with results from two theoretical methods,

- (i) Linear theory<sup>1</sup> which is the basis of the wing design. This theoretical loading distribution ( $\lambda$ ) is that which was specified at the start of the design. The theoretical pressure distribution was derived by combining this loading distribution with the calculated pressure coefficients ( $C_{p_{vol}}$ ) due to the thickness distribution<sup>14</sup>, so that:

$$C_{p_U} = C_{p_{vol}} - \lambda/2$$

$$C_{p_L} = C_{p_{vol}} + \lambda/2 .$$

- (ii) A nonlinear, inviscid, incompressible theory due to Roberts and Rundle<sup>15</sup>. This theoretical method calculates pressure distributions on the upper and lower surfaces of the wing and hence the loading distribution ( $\lambda$ ) is derived from:

$$\lambda = - \left( C_{p_U} - C_{p_L} \right) .$$

Before proceeding to detailed comparisons of pressure and loading distributions, it is interesting to compare the experimental and theoretical values of lift and centre of pressure position at the theoretical attachment incidence ( $5.32^\circ$ ).

Parameter	Linear theory <sup>1</sup>	Nonlinear theory <sup>15</sup>	Force tests $R = 6.7 \times 10^6$	Pressure measurement tests $R = 6.7 \times 10^6$
$C_L$	0.100	0.109	0.100	0.099
$\frac{x_{cp}}{c}$	0.533	0.556	0.504	0.509

This table shows that the integrated results from the pressure measurement tests confirm the values obtained from the overall force measurements. It is also clear that the two theoretical methods predict very different centre of pressure positions and that the experimental position is significantly further forward than either of them.

Fig 16 which compares the experimental and theoretical spanwise loading distributions at various chordwise stations shows clearly that:

- (i) there are large differences between the experimental results and linear theory<sup>1</sup> over the entire wing,
- (ii) the nonlinear calculations are in good agreement with the experimental results over the forward part of the wing ( $x/c < 0.40$ ).

The pressure distributions corresponding to these loading distributions are shown in Fig 17. As would be expected from above, the linear theory<sup>1</sup> gives a poor prediction of the pressure distribution over nearly all the wing. Over the forward part of the wing ( $x/c < 0.40$ ) the nonlinear calculations<sup>15</sup> of pressure distribution are in good agreement with the experimental results. However, over the aft part of the wing ( $x/c > 0.60$ ) there are major differences between calculation and experiment on the lower surface and near the centreline on the upper surface. It seems likely that these differences arise from boundary layer effects since the longitudinal pressure gradient on the lower surface and the spanwise pressure gradient on the upper surface become adverse on this area of the wing.

Pressure distributions from linear theory<sup>1</sup> are derived by the addition of a specified loading distribution and the theoretical pressure distribution due to the addition of thickness ( $C_{pvol}$ ). If we invert this procedure, an estimate can be made of the experimental pressure distribution due to the thickness by averaging the appropriate values of the upper and lower surface pressure

coefficients  $[C_{pU} + C_{pL}/2]$ . Fig 18 compares these estimates from both wings with the theoretical distribution and shows that, particularly for  $x/c = 0.06$ , there are significant differences between them. Ref 1 explains that the theoretical values<sup>14</sup> are not valid close to the edges of the planform but the difference between the two experimental distributions suggests that there is an important interaction between camber and thickness.

Thus it would appear that the differences between the experimental and design loading and pressure distributions<sup>1</sup> arise from:

- (i) neglect of nonlinear terms in the design of the camber surface,
- (ii) the interaction between camber and thickness but this is less important than the previous cause.

It seems likely that the differences between the experimental results and the nonlinear, inviscid calculations<sup>15</sup> are due to boundary layer effects over the rear part of the wing ( $x/c \geq 0.60$ ).

## 5 ANALYSIS OF PRESSURE MEASUREMENTS WITH SEPARATED FLOW

### 5.1 General details of flow

On a symmetric, slender wing with sharp leading edges, attached flow conditions can only exist on both surfaces at zero incidence. If the incidence is increased, the flow separates at the leading edges and the resultant vortex sheets roll up to form the primary leading-edge vortices. Near each leading edge, another stream surface, influenced by this vortex, attaches to the wing surface inboard of the vortex. The airflow over the wing inboard of this attachment line remains attached but that outboard is affected by the spanwise outflow beneath the vortex and as it approaches the leading edge another flow separation occurs forming a smaller secondary vortex sheet. On the lower surface of the wing, the flow is attached everywhere. For a cambered wing designed for attached flow along the entire length of the leading edges at  $\alpha_{des}$ , the flow state similar to that described above occurs when the incidence is increased from  $\alpha_{des}$ . Typical spanwise pressure distributions and a schematic spanwise cross section of this type of flow are shown in Fig 19 for both wings ( $x/c = 0.30$ ).

This figure shows that for the symmetric wing (Fig 19a) the upper surface pressure coefficient ( $-C_{pU}$ ) increases slightly with increasing  $\eta$  until at about the point where the flow attaches it drops. Influenced by the primary vortex  $-C_p$  rises steeply to  $-C_{pmin}$  and then begins to fall. The secondary

vortex causes a smaller suction peak which when combined with the decrease from  $-C_{p_{min}}$  produces the hump in the distribution close to the leading edge.

Two effects of increasing incidence can be seen:

- (i)  $-C_{p_U}$  increases uniformly over the inboard part of the wing and  $-C_{p_L}$  decreases similarly but over a greater part of the span,
- (ii) strengthening of the primary leading-edge vortex gives an increase in  $-C_{p_{min}}$  and a decrease in  $\eta - C_{p_{min}}$ .

Broadly speaking, the effects on loading caused by (i) can be thought of as the linear component of normal force and (ii) as the nonlinear part (cf section 3.1)

For the cambered wing (Fig 19b) the same trends are seen relative to the attached-flow pressure distribution but the inboard section shows a curious kink in  $-C_{p_U}$  at incidences above  $10^\circ$ . Flow visualisation patterns such as that shown in Fig 20 suggest that weak vortices caused by separations near the wing apex are swept downstream close to the centreline and they presumably are the cause of these kinks in the pressure distributions.

### 5.2 Local normal force

The local normal force coefficient  $C_N(x/c)$  was determined at all incidences and chordwise stations by spanwise integration of the pressure distributions. The values are given in Table 8 and plotted in Figs 21 and 22.

For the symmetric wing at low incidences ( $\alpha = 2.5^\circ$  and  $5^\circ$ )  $C_N(x/c)$  is constant for  $0 \leq (x/c) \leq 0.4$  implying a conical flow development. For this range of  $x/c$ , the local semispan  $s(x/c)$ , is approximately  $1.25(x/c)s$  and therefore  $ds(x/c)/d(x/c)$  is independent of  $x/c$ . However, the local thickness/span ratio of the wing is large and variable and this evidence of conical flow is unexpected. Increasing incidence destroys this 'conical' flow and  $C_N(x/c)$  has a maximum for each incidence near  $x/c = 0.20$ .

The cambered wing shows a different chordwise development of  $C_N(x/c)$ . For this wing, the camber surface is non-conical and  $C_N(x/c)$  decreases monotonically to the trailing edge.

At the higher incidences on both wings, the  $C_N(x/c)$  characteristics develop hollows in the range  $0.6 \leq (x/c) \leq 1.0$ . These are particularly noticeable for the symmetric wing and are due to vortex breakdown which is discussed in section 5.3.

In Fig 22, that part of  $C_N(x/c)$  due to increasing incidence is compared for the two wings, ie  $C_N(x/c)$  for the symmetric wing is compared with  $C_N(x/c) - (C_N(x/c))_{\alpha_{des}}$  for the cambered wing (where  $(C_N(x/c))_{\alpha_{des}}$  is the local normal force coefficient at the design incidence  $\alpha_{des} = 5.32^\circ$ ).  $C_N(x/c) - (C_N(x/c))_{\alpha_{des}}$  is plotted against  $x/c + 0.04(\alpha^0 - \alpha_{des}^0)$  so that the results for the cambered wing can be interpolated for values of  $(\alpha - \alpha_{des})$  equal to the incidences of the symmetric wing. These interpolated values are joined by the chain dashed lines and are to be compared with the crosses. Before doing this however, it is worth noting that for the cambered wing, the lowest curve ( $\alpha = 7.5^\circ$ ) is constant for  $x/c < 0.4$  which is comparable with the symmetric wing at  $\alpha = 2.5^\circ$ . This implies that the change in flow caused by increasing the incidence from the attachment incidence is, in some sense, nearly conical over the front part of the wing.

Interpolated values of  $C_N(x/c) - (C_N(x/c))_{\alpha_{des}}$  are given in Fig 22 for  $(\alpha - \alpha_{des}) = 5^\circ, 10^\circ, 15^\circ$  and  $20^\circ$  and these differ by less than  $\pm 6\%$  from the symmetric wing results. Consistently,  $C_N(x/c)$  for the symmetric wing changes more near the apex but further aft agreement is very good until the wings are affected by vortex breakdown (indicated by a jink in the constant  $x/c$  lines for  $x/c \geq 0.70$  between  $\alpha - \alpha_{des} = 10^\circ$  and  $15^\circ$ ). Despite this, the results shown in Fig 22 suggest that within a family of cambered wings, the local normal force characteristics of the symmetric wing could be used to make a reasonably accurate estimate of the characteristics of one of the cambered members.

Multiplying  $C_N(x/c)$  by  $s(x/c)/s$  and integrating with respect to  $x/c$  determines  $\bar{C}_N$  which is compared with the results of the force measurement tests in Fig 23. It is immediately evident that the slope of the curve derived by integration of the loading distribution is less than that from the force tests. Generally, the integrated pressure results are about 3% less than the forces results except in the regions where vortex breakdown affects lift development ( $13.5^\circ$  for the symmetric wing and  $16.7^\circ$  for the cambered wing). Ref 16 shows vortex breakdown to be sensitive to the details of the experimental procedure. It is possible that some difference in procedure between force and pressure measurement tests in this investigation is responsible for the difference in  $\bar{C}_N$  near vortex breakdown.

The position of the centre of pressure on the wings ( $x_{cp}/c$ ) derived from the pressure measurement tests is shown in Fig 24. The agreement with the force test results ( $\pm 0.005$ ) is very good and it should be noted that at vortex

breakdown (seen as a dip in the curves for  $\bar{C}_N \approx 0.5$ ) the position of the centre of pressure derived from the pressure measurement tests is further forward than that derived from the force tests.

The integration for  $x_{cp}/c$  (section 2.1) cannot be evaluated for the symmetric wing at  $\alpha = 0^\circ$  since both integrands tend to zero as  $\alpha$  tends to zero. However the integrals may be rewritten:

$$\frac{x_{cp}}{c} = \frac{\int_0^1 \frac{x}{c} \frac{s(x/c)}{s} \frac{C_N(x/c)}{\alpha} d\left(\frac{x}{c}\right)}{\int_0^1 \frac{s(x/c)}{s} \frac{C_N(x/c)}{\alpha} d\left(\frac{x}{c}\right)}$$

where, as  $\alpha$  tends to zero,  $C_N(x/c)/\alpha$  tends to a finite limit  $(C_N(x/c)/\alpha)_0$ . Extrapolation of  $C_N(x/c)/\alpha$  to  $\alpha = 0$  enables not only  $(x_{cp}/c)_0$  but also  $(\bar{C}_N/\alpha)_0$  ( $= a$ ) to be evaluated for comparison with the results derived from the force measurement tests. Fig 24 shows that the value of  $(x_{cp}/c)_0$  so derived ( $= 0.549$ ) to be very close to the result from the force tests (0.547).

Jones<sup>17</sup> predicts (in the notation of this Report):

$$\left( \frac{C_N(x/c)}{\alpha} \right)_0 = 2\pi \frac{ds(x/c)}{dx} .$$

In Fig 25 this prediction is compared with the extrapolated values of  $(C_N(x/c)/\alpha)_0$  for the symmetric wing and  $\left[ (C_N(x/c) - (C_N(x/c))_{ades}) / (\alpha - \alpha_{ades}) \right]_{\alpha_{ades}}$  for the cambered wing. It should be noted that Jones' prediction only goes to zero at  $x/c = 1$  on planforms (such as that tested) which have streamwise tips. Fig 25 shows that the prediction is too high everywhere and that the centre of lift is too far aft. Comparing the experimental results for the two wings, those for the cambered wing are higher near the apex but lower near the trailing edge. Integration of  $(C_N(x/c)/\alpha)_0$  to yield values of the parameter 'a' (defining the linear component of normal force) gives the following results:

Wing	'a'		
	Pressure test	Force test	Jones <sup>17</sup>
Symmetric	1.643	1.666	
Cambered	1.644	1.635	} 2.175

The agreement between the force test results and the pressure measurement tests is encouraging in view of the disappointing comparison of the normal force characteristics in Fig 23 and the uncertain accuracy with which  $(C_N(x/c)/\alpha)_0$  can be determined.

### 5.3 Vortex characteristics

Two major parameters of the pressure distribution which are dependent upon the strength and position of the leading-edge vortices are  $-C_{p_{min}}$  and  $n-C_{p_{min}}$  (see Fig 19a).

$-C_{p_{min}}$  is plotted against  $x/c$  in Fig 26 for both wings. As the incidence increases from the attached-flow value,  $-C_{p_{min}}$  increases approximately linearly until the breakdown of the leading-edge vortices crosses the trailing edge. To compare the values of  $-C_{p_{min}}$  for the cambered wing with those for the symmetric wing it is necessary to interpolate for values at similar angles above the attachment incidence. It is also necessary to allow for the difference in  $C_{p_U}$  at the attachment incidence for the cambered wing ( $\alpha_{des} = 5.32^\circ$ ) compared with that for the symmetric wing at  $\alpha_{des} = 0.0^\circ$ . Although it was shown in section 4 that  $C_{p_U} \neq C_{p_{vol}} - (\ell/2)$ , it is a sufficiently accurate estimation to permit the following comparison:

$-C_{p_{min}} - (\ell_{att}/2)$  interpolated for  $\alpha - \alpha_{des} = 5^\circ, 10^\circ, 15^\circ, 20^\circ$  for the cambered wing

with  $-C_{p_{min}}$  at  $\alpha = 5^\circ, 10^\circ, 15^\circ, 20^\circ$  for the symmetric wing.

( $\ell_{att}$  is the measured attachment incidence loading on the cambered wing at  $n-C_{p_{min}}$ .) This comparison is shown in Fig 27 which shows that the interpolated values for the cambered wing are higher over the forward part of the wing, but the pattern of behaviour is confused at the higher incidences just ahead of the trailing edge. To explain this it is necessary to examine the effects of vortex breakdown on  $-C_{p_{min}}$ .

For the wing in Ref 16 it was possible to see the forward progression of vortex breakdown over the wing by plotting  $C_N(x/c)$  against incidence (see Ref 16, Fig 14). This was possible because  $C_N(x/c)$  could be evaluated at 1 degree intervals of incidence in the range of interest. Since the present data is only available at intervals of  $2.5^\circ$  it is not sufficiently detailed to allow such analysis directly and, even when  $-C_{p_{min}}$  is plotted against incidence, no definite trend for the effect of vortex breakdown can be seen. Everywhere on the upper surface of the wing it has therefore been necessary to consider  $C_{p_U}$  as being composed of two component:

- (i) a linear component associated with the linear component of normal force;
- (ii) a nonlinear component associated with the leading-edge vortices (and hence the nonlinear component of normal force).

For the symmetric wing at a given chordwise station, the linear component of  $C_{p_U}$  is  $-\alpha(C_N(x/c)/\alpha)_0/2$ . The nonlinear component on the upper surface is therefore  $C_{p_U} + \alpha(C_N(x/c)/\alpha)_0/2$  and we may consider in particular  $C_{p_{min}} + \alpha(C_N(x/c)/\alpha)_0/2$ . This can be approximated by  $C_{p_{min}} + (\alpha a/2)$  where 'a' is as defined and evaluated previously (see section 5.2). For the cambered wing, the corresponding quantity is:

$$C_{p_{min}} + \frac{\lambda_{att}}{2} + \frac{a(\alpha - \alpha_{des})}{2} .$$

These quantities are plotted in Fig 28 which shows that the curves quite definitely peak and the value of  $\alpha$  at the peak ( $\alpha_{VB}$ ) is quite accurately defined. At values of  $\alpha$  greater than  $\alpha_{VB}$  the behaviour on the two wings is different; the curves for the symmetric wing tending to decline more slowly before increasing again.  $\alpha_{VB}$  is plotted against  $x/c$  in Fig 29. For the symmetric wing, vortex breakdown crosses the trailing edge at  $10.4^\circ$  and moves forward linearly with increasing incidence. For the cambered wing, the trailing edge is crossed at  $14.7^\circ$  and the curve is initially steeper but nonlinear. Therefore since vortices do not occur on the upper surface of this wing until  $\alpha = 5.32^\circ$ , the breakdown of the leading edge vortices crosses the trailing edge after an increase in incidence of  $9.4^\circ$ . Further forward (eg  $x/c = 0.6$ ) vortex breakdown occurs relatively  $2.6^\circ$  earlier on the cambered wing. This difference in vortex breakdown behaviour is the cause of the curves for the two wings crossing in Fig 27.

Using Fig 29 it is possible to identify the  $x/c$  value of vortex breakdown at which the force measurements are affected. From Fig 7 it can be seen that the generalised form of  $C_N/\alpha$  has a local maximum near  $\alpha = 13.5^\circ$  for the symmetric wing and near  $\alpha = 16.7^\circ$  for the cambered wing. Fig 29 shows that at these incidences, vortex breakdown is affecting both wings aft of  $x/c = 0.82$ . Obviously force measurement tests only show vortex breakdown characteristics when a significant part of the wing is so affected but the fact that the pressure measurement tests give the rearmost 18% of the centreline chord for both wings is interesting since this implies that 30% of the wing area is so affected.

The spanwise position of the peak suction  $\eta_{C_p \min}$ , is plotted in Fig 30. The accuracy with which  $\eta_{C_p \min}$  can be determined is itself determined by the spanwise distribution of pressure measurement points on the upper surface of the wing. On the forward part of the wing ( $x/c \leq 0.50$ ) the distribution near the leading edge is such that it should be possible to determine  $\eta_{C_p \min}$  to within 2% (see Fig 1). For  $x/c > 0.55$  however this figure is likely to be greater due to the sparser distribution of pressure measurement points. Therefore when discussing  $\eta_{C_p \min}$  as plotted in Fig 30, the possible inaccuracy of it has to be remembered.

Fig 30a&b shows that at comparable angles above the attachment incidence  $\eta_{C_p \min}$  is significantly greater for the cambered wing than for the symmetric wing for forward stations. In the apex region, which is most cambered, the differences in  $\eta_{C_p \min}$  are most obvious but the local span is small and hence large differences between  $\eta_{C_p \min}$  for the cambered and symmetric wings represent only small differences in terms of  $y$ .

Barsby<sup>3</sup> has calculated the position of the centre of the leading-edge vortex core above conically cambered wings of circular arc spanwise section. The cambered wing of this Report is neither conically cambered nor of circular arc cross-section but it is possible to use the results of Ref 3 to give a theoretical estimate of the changes in vortex position solely due to camber.

The ratio  $\eta_c/\eta_s$  characterises this change - where  $\eta_c$  is the predicted spanwise position of the vortex above the cambered wing which depends on the local spanwise camber shape and  $(\alpha - \alpha_{des})$ , and  $\eta_s$  is the corresponding quantity for the symmetric wing. To evaluate  $\eta_c$  it is necessary to approximate the camber surface (at all values of  $x/c$ ) by a circular arc as shown schematically in Fig 31. This determines a parameter  $p$  which varies along the chord as shown. For each required value of  $(\alpha - \alpha_{des})$  and  $p$ ,  $\eta_c$  is obtained from

the results of Ref 3 by interpolation. Division of  $n-C_{p\min}$  for the cambered wing by the relevant value of  $n_c/n_s$  gives a set of 'pseudo-symmetric wing' results which are plotted in Fig 30c and can be compared directly with those in Fig 30a;  $n-C_{p\min}$  (Fig 30a) and  $n-C_{p\min}/(n_c/n_s)$  (Fig 30c) decrease approximately linearly with increasing  $(\alpha - \alpha_{des})$ . For  $(\alpha - \alpha_{des}) \approx 20^\circ$  the difference is less than  $\pm 2\%$  of local semispan (which is the accuracy of determination of  $n-C_{p\min}$ ).

The effect of vortex breakdown on  $n-C_{p\min}$  can only be seen in Fig 30a as an inflection of the  $x/c = \text{constant}$  curves. At incidences above that at which a given chordwise station is so affected,  $n-C_{p\min}$  decreases more rapidly. This is due to the diffusion of the vortex core which occurs when the tightly rolled vortex bursts<sup>18</sup> with a consequent reduction in axial velocity.

In conclusion, methods of analysis have been developed which correlate the values of the peak suctions ( $-C_{p\min}$ ) and their spanwise positions ( $n-C_{p\min}$ ) for the cambered and symmetric wings. Use of these methods would enable a designer to make reasonable predictions of these characteristics of the leading-edge vortices of a cambered wing from a knowledge of those of the corresponding symmetric wing. Confident prediction of vortex breakdown on the cambered wing is not possible though an estimate can be obtained from the results of the present series of tests.

## 6 CONCLUSIONS

Two slender wings of mild gothic planform have been tested in a low-speed wind tunnel. One of the wings was symmetric and the other incorporated a camber surface designed using a linear theory to give attached flow along the leading edges at a specified loading distribution. Force measurement tests on the two wings confirm the general relationships, found in earlier tests, between their longitudinal characteristics. In particular, at twice the design lift coefficient, the lift-dependent drag of the cambered wing is about 20% lower than that of the symmetric wing due to the favourable shift of the minimum point of the drag polar caused by the addition of camber. At higher values of the lift coefficient this reduction in lift-dependent drag is less due to the unfavourably-changed shape of the cambered wings drag polar.

The principal aims of the investigation were to determine the validity of the design theory for the cambered wing and also to provide information on the effects of camber on the development of the flow when it separates along the leading edges of the wing.

Flow visualisation tests and the form of the measured pressure distribution near the leading edges of the cambered wing at its design incidence confirm that the flow is attached along the leading edges. The loading distribution, derived from the measured pressure distributions on the cambered wing at its design incidence, explains the discrepancy shown between the theoretical position of the centre of pressure and that determined by the force measurement tests. It shows that the area of the wing ahead of the trailing edge carries less load and that near the apex, more load than specified in the design loading. This is due, primarily, to the neglect of nonlinear terms in the design method though the interaction between camber and thickness does have a minor effect. This redistribution of load has little effect on the overall lift of the wing but is significant in moving the centre of pressure forward.

A comparison has also been made between the measured loading distribution at the design incidence and a nonlinear, inviscid calculation. Over the forward part of the wing these calculated pressures and loadings agree with the measured values but boundary layer development over the rear part of the wing produces significant differences particularly to the pressure distribution on the lower surface of the wing.

When the flow separates along the leading edge, it has been shown that if the pressure (or loading) distribution is treated as consisting of linear and nonlinear components then it is possible to correlate the local normal force coefficients on the cambered and symmetric wings. Furthermore it has been shown that the peak suctions under the leading-edge vortices on the two wings can be correlated and theoretical work on leading-edge vortices above conically cambered wings can be used to correlate the spanwise position of these peak suctions. The limit of this ability to predict the characteristics of the cambered wing from those of the symmetric wing is determined by the phenomenon of vortex breakdown. Whilst the streamwise variation of vortex breakdown with incidence has been well defined on both wings it has not been possible to correlate the results.

### Appendix A

#### DETAILED DESCRIPTION OF THE MODELS

The sandwich-like construction of the models, with laminated teak bonded either side of a metal and fibreglass spine, was chosen to ensure that the pitching moment load which is taken from the model near the trailing edge would not distort the model and also to give the areas near the leading and trailing edges added strength since, in some places, they are very thin.

For measuring the surface static pressures, hypodermic tubes (1.22 mm o/d, 0.71 mm i/d) were recessed into the model and 0.4 mm diameter holes drilled into them. In order to facilitate comparisons with theory, the pressure holes in the cambered wing were drilled (at the chordwise stations shown in Fig 1) with the model set at the design incidence of  $5.32^\circ$ , and for the symmetric wing the holes were drilled with the model horizontal. The distribution of the tubes in the upper surface is shown in Fig 1. Two points which should be noticed in this figure are the different spanwise distributions up- and downstream of  $x/c = 0.5$  and the fact that there are separate sets of tubing for the two regions. The different distributions were chosen because for the cambered wing the forward part of the wing is more cambered than the rearward part and the chosen distribution gives a more uniform distribution of tubes over the upper surface for  $x/c < 0.5$ . However, not all the tubes in the forward part of the upper surface could be extended as far forward as  $x/c = 0.10$  and 0.06 due to their close proximity to each other and to the leading edge.

Since the lower surfaces of the models are less affected by steep pressure gradients, the distribution of tubes in the lower surface is less comprehensive and does not differ up- and downstream of  $x/c = 0.5$  though, as on the upper surface, there are two sets of tubes. The spanwise positions of the tubes in the lower surface are  $\eta = 0, \pm 0.1, \pm 0.2, \pm 0.3, \pm 0.4, \pm 0.5, \pm 0.6, \pm 0.7, \pm 0.8, \pm 0.875$  and  $\pm 0.95$ . At  $x/c = 0.95$ ,  $\eta = \pm 0.95$  either the upper or lower surface tube had to be discarded since the model is not thick enough there for both. However since both port and starboard sides of the models were inlaid with hypodermic tubes, it was possible to obtain values of static pressure on both surfaces at  $x/c = 0.95$ ,  $\eta = 0.95$  though on different sides of the model.

Between  $x/c = 0.5$  and 0.55 the tubes in both surfaces converge on the area around the central main strut pivot. Beneath the plate covering the pivot, the ends of the 96 hypodermic tubes (54 from the upper surface, 42 from the lower surface) were connected to a cluster of hypodermic tubes housed inside the

circular main strut using small bore plastic tubing. This arrangement avoided having bundles of tubing in the airstream which can affect leading-edge vortex development and breakdown<sup>16</sup>. From underneath the tunnel, the tubes were extended with larger bore plastic tubing to the pressure measuring system (described in Appendix C).

For the force measurement tests the cluster of tubing inside the circular main strut and the connections to the pressure measuring system were removed since they would have caused errors in the measurement of the forces by making a partial connection between the measuring parts of the balance and 'earth'. In addition all the surface static pressure measurement tappings were covered with adhesive tape aligned along constant values of  $n$ . At the higher Reynolds numbers ( $R = 6.7 \times 10^6$  and  $4.0 \times 10^6$ ) this ensured that transition of the boundary layer was fixed but at the lowest Reynolds number ( $R = 2.0 \times 10^6$ ) extra roughness (in the form of small glass balls 0.6 mm diameter placed in narrow bands close to the leading edges) was needed to prevent separation of the laminar boundary layer on the upper surface at the design incidence. The results of the force tests at this lowest Reynolds number indicate that whilst the roughness bands do fix transition around the attachment incidence they also adversely affect the development of the leading-edge vortices (section 3).

To enable the interference of the main strut on the wing to be determined a dummy main strut was used so that measurements could be made with a near symmetric mounting system. A perfectly symmetric mounting system was not possible because a dummy incidence strut could not be supported from the model. The dummy main strut, when used, became an integral part of the main strut as shown in Fig 4.

A selection of plates were made to fit around the main and dummy struts at fixed wing incidences to prevent air flow from one surface of the model to the other. When the dummy strut was not used, a blanking plate was used on the upper surface and the hole in the lower surface plate was elongated to allow a range of incidence to be tested without repeatedly changing the plates.

The cambered wing could be mounted either way up on the strut system so that the strut interference effects on the overall forces could be estimated.

Both models were pivotted on the main strut at a point on the line joining the apex and centre of the trailing edge 0.54c from the apex and the incidence was controlled by the incidence strut which was attached on the model centreline at  $x/c = 0.94$ .

## Appendix B

### CORRECTION OF RESULTS FOR SUPPORT INTERFERENCE

#### B.1 Correction of overall force measurements

At each of the three Reynolds numbers, force measurements were made with the model:

- (i) upright;
- (ii) inverted;
- (iii) inverted with the dummy strut.

A first order estimate of the interference effects between the model and the main strut was made from the differences between the runs with the model inverted with and without the dummy strut. For both models the values so determined at the three Reynolds numbers were combined to give a weighted mean result (weighted according to the relevant dynamic pressure,  $\frac{1}{2}\rho V^2$ , which are roughly in the ratio 1:4:11). No correction for the interference effects of the incidence strut can be deduced from this series of tests so that derived elsewhere<sup>19</sup> has been used.

The requirement that the drag polar of the symmetric wing should be symmetric enabled a mean tunnel flow angle to be determined. The force results for both models were corrected for this. A similar requirement for the lift and pitching moment curves of the symmetric wing to pass through the origin determined final small corrections to  $C_L$  and  $C_m$ . The values of these corrections are given in Table 2.

At the lowest Reynolds number ( $R = 2.0 \times 10^6$ ), where roughness was needed to prevent a laminar boundary layer separation on the upper surface, it proved impossible to make the drag polar of the symmetric wing symmetric by a realistic correction for tunnel mean flow inclination. An estimate was therefore made by extrapolation of the values determined at the two higher Reynolds numbers but maintaining consistency with the known tunnel characteristics<sup>20</sup>.

#### B.2 Correction of pressure measurements

##### B.2.1 General discussion

The values of the static pressure coefficient,  $C_p$ , were obtained from the raw data using an existing computer programme<sup>7</sup> which included a correction for tunnel blockage but corrections still had to be found for the effects of:

- (i) inclination of the tunnel flow;
- (ii) the interference of the strut supports.

Since one of the principal aims of the experiment is to compare the experimental and theoretical loading distributions at the design incidence for the cambered wing, a correction for inclination of the tunnel flow cannot be applied as a correction to the wing incidence. Rather a combined correction is applied for both the above effects by subtracting from the load at each point on the wing the corresponding load on the symmetric wing at  $\alpha = 0^\circ$ . In many cases this does not have to be done explicitly, it is necessary only to correct the value of the local normal force coefficient:

$$C_N(x/c) = \frac{1}{2} \int_{-1}^1 l(n) dn$$

where  $n = y/s(x)$

by subtracting the corresponding integrated loading distribution on the symmetric wing at  $\alpha = 0^\circ$ .

#### B.2.2 Corrections at the attachment incidence

For each wing, the attachment incidence is the only incidence for which a fully corrected pressure distribution has been derived. The corrections to the pressure distribution at the attachment incidence for the cambered wing are clearly very important to the validity of the comparison of the experimental and theoretical distributions. Hence it is important to describe the derivation of the corrections in order to assess their accuracy and validity.

As described below, data from tests on the symmetric wing at  $\alpha = 0^\circ$ , with and without the dummy strut, have been used to determine a corrected pressure distribution on that wing such that at zero incidence the load is zero everywhere. The differences between this pressure distribution and that measured on the upper and lower surfaces of the model are considered as suitable corrections for the cambered wing's upper and lower surface pressure distributions at the design incidence of  $\alpha = 5.32^\circ$ .

Fig 32 shows the measured chordwise load distribution  $\left[ \frac{s(x/c)}{s} C_N(x/c) \right]$  on the symmetric wing at  $\alpha = 0^\circ$ . Also shown is the additional chordwise load produced by adding the dummy strut  $\left[ \frac{s(x/c)}{s} \Delta C_N(x/c) \right]$ . Since the main and dummy

struts are fitted on opposite surfaces of the model, the sign of one of these quantities has been changed to simplify their comparison. If it is assumed that the measured chordwise load distribution on the symmetric wing at  $\alpha = 0^\circ$  is due to:

- (i) interference of the main strut support
- (ii) interference of the incidence strut near the trailing edge, and
- (iii) inclination of the tunnel flow,

then the difference between the two curves in Fig 32 is primarily a combination of the last two of these.

For  $0.45 \leq x/c \leq 0.75$ , the differences shown in Fig 32 must be due to minor differences between the main and dummy struts but the similarity between the curves over the forward part of the wing suggests that the major effect of the main strut can be derived from the effect of adding the dummy strut.

The first step in deriving the corrected pressure distribution on the symmetric wing at  $\alpha = 0^\circ$  was to subtract from the measured distribution the incremental distribution on the opposite surface of the model due to the addition of the dummy strut. In the region around the main strut (where small physical differences between the main and dummy struts can cause large differences in the pressure distributions),  $C_p$  (with the initial correction for the main strut effect) was plotted against  $x/c$  and  $n$ . From these plots, small secondary corrections were determined which made the resulting pressure distributions realistic. Fig 33a shows how the overall correction which was applied for the effect of the main strut differs from the effect of the dummy strut for a spanwise station ( $x/c = 0.45$ ) close to the strut.

For that part of the wing which is affected by the incidence strut ( $0.80 \leq x/c \leq 0.95$ ), the effect of the strut was assumed to be confined to the inboard part of the lower surface. Once again, by plotting  $C_p$  against  $x/c$  and  $n$  and considering the gradients of the pressure distribution on the upper surface of the model, a correction to the pressure distribution was determined to compensate for the presence of the incidence strut.

After corrections had been applied for the effects of the main and incidence struts, the residual load on the wing was considered to be the result of tunnel flow inclination. It is assumed that (for small positive angles of flow inclination), at any point on the wing, the magnitude of the decrease in upper surface pressure is equal to the increase on the lower surface. Therefore, the

fully corrected pressure distribution on the symmetric wing at  $\alpha = 0^\circ$  was obtained by averaging the upper and lower surface pressure distributions after correcting for the main and incidence strut interferences.

The corrected pressure distributions on the cambered wing at its design incidence ( $\alpha = 5.32^\circ$ ) were then obtained by subtracting from the measured distributions the sum of the corrections applied for the symmetric wing at  $\alpha = 0^\circ$ .

However, before the cambered wing pressure distributions were corrected, it was noticed that on the lower surface in the region of the incidence strut the pressure coefficient  $C_{pL}$  did not vary as was expected from:

- (i) measurements at higher incidences, and
- (ii) corresponding measurements on the symmetric wing.

For four points on the lower surface, the measured variation of  $C_{pL}$  with incidence is shown in Fig 33b together with the expected linear variation. The nonlinearities shown in this figure near the attachment incidence are too localised (in terms of model incidence) to be associated with the variation of strut interference with incidence shown in Table 2. Rather it must be attributed to some mutual interference between the main and incidence struts which is peculiar to the cambered wing near its attachment incidence. It was therefore believed that in the region affected ( $0.65 \leq x/c \leq 0.95$ ,  $0 \leq |\eta| \leq 0.6$ ) the pressure distribution on the lower surface should be corrected for this effect before the main corrections (determined from the symmetric wing tests) were applied.

#### B.2.3 Corrections at non-attachment incidences

When the flow separates at the leading edges and rolls up to form leading-edge vortices above the upper surface of the wing, the characteristics of the pressure distributions which are of interest are:

- (i) the value and position of the peak suction induced by the leading-edge vortex, and
- (ii) the local normal force coefficient,  $C_N(x/c)$ .

No corrections were applied to the measured distributions for the first of these for two reasons:

- (i) the corrections (determined as described in section B.2.2) are small compared to  $C_{p\min}$  at  $\eta = \eta_{-C_{p\min}}$ , and

(ii) the corrections which have been determined are probably not applicable throughout the incidence range.

The corrected local normal force coefficient,  $C_N(x/c)$  was determined for all stations and incidences by subtracting from the uncorrected value the uncorrected value at the same station on the symmetric wing at  $\alpha = 0^\circ$ . Although the strut interferences (Table 2) vary through the incidence range, no estimate can be made of the effect of this variation on the correction applied to  $C_N(x/c)$ .

Appendix CDESCRIPTION OF THE PRESSURE MEASUREMENT SYSTEM

The system for measuring the model surface static pressures used four 'Scanivalve' rotary pressure switches and pressure transducers. The system was designed to allow a reasonable settling time after switching pressures to the transducers before reading, but to minimise the time taken to sample all the pressures, the 'Scanivalves' were switched in a ripple sequence. The output from the four  $\pm 17 \text{ kN m}^{-2}$  ( $\pm 2.5 \text{ psi}$ ) transducers was displayed on a digital voltmeter and also output via a paper-tape punch. The corrected values of the static pressure coefficient,  $C_p$ , were computed from this raw data output, transducer calibrations and tunnel reference pressures using an established computer programme<sup>7</sup>.

Whilst each 'Scanivalve' has 48 measuring ports, to eliminate any hysteresis of the transducers, alternate ports were connected to a gauge pressure higher than any measured in the tests [ $14 \text{ kN m}^{-2}$  ( $+2 \text{ psi}$ )]. Thus on each 'Scanivalve' there are 24 ports available for measuring pressures and these were measured relative to the wind-tunnel nozzle section static pressure by feeding that pressure to the reference side of the transducers.

In order to measure the transducer zero on each scan, the first available port was also connected to the nozzle static pressure tapping. The tunnel maximum section static pressure tapping was connected to the second available port as a check on the tunnel conditions during the run and a reference pressure of  $-17 \text{ kN m}^{-2}$  ( $-2.5 \text{ psi}$ ) was connected to the third port. This third reading is used on each scan as a calibration of the transducer slope and it is assumed that all nonlinearities scale with this.

Using this system, there were 84 ports (21 per 'Scanivalve') available for measuring the surface static pressures. This is less than the number of hypodermic tubes in the model but, owing to their spacing, some near the centreline on both surfaces were discarded without loss of definition of the surface pressure distributions.

Table 1MODEL GEOMETRY

	<u>Symmetric wing</u>	<u>Cambered wing</u>
Centreline chord c	1.270 m	1.275 m
Trailing edge span b (= 2s)	1.026 m	1.026 m
Wing area s	0.760 m <sup>2</sup>	0.763 m <sup>2</sup>
Aspect ratio A	1.385	1.380
Max thickness t/c	0.0902	0.0894
Pivot point	0.54c (on line joining apex and centre of trailing edge)	0.54c
$\alpha_{des}$	0.0°	5.32°
$c_{L_{des}}$	0.000	0.100
$\left(\frac{x_{cp}}{c}\right)_{des}$	-	0.533
Planform equation:	$\frac{y}{s} = \frac{5(x/c) - (x/c)^5}{4}$	
Thickness distribution:	$z = \pm B\left(\frac{x}{c}\right) \left(1 - \frac{y^2}{s^2} (x/c)\right)$	

where  $B\left(\frac{x}{c}\right)$  is the centreline thickness distribution:

$$\begin{aligned} \frac{B(x/c)}{c} = 0.09 \frac{x}{c} \left(1 - \frac{x}{c}\right) & \left[ 3.2471 - 7.5777 \frac{x}{c} + 17.8647 \left(\frac{x}{c}\right)^2 \right. \\ & \left. - 19.2073 \left(\frac{x}{c}\right)^3 + 7.6754 \left(\frac{x}{c}\right)^4 \right] \end{aligned}$$

Table 2CORRECTIONS FOR STRUT TARES, MODEL ASYMMETRY AND STRUT INTERFERENCESStrut tares $V = 76 \text{ m/s}$ 

$\alpha$	$\Delta C_L$	$\Delta C_D$	$\Delta C_m$
-5	0.002	0.0119	$\bar{0.0018}$
0	0.002	0.0118	$\bar{0.0018}$
5	0.002	0.0117	$\bar{0.0018}$
10	0.002	0.0116	$\bar{0.0018}$
15	0.002	0.0115	$\bar{0.0018}$
20	0.002	0.0115	$\bar{0.0018}$
25	0.002	0.0115	$\bar{0.0018}$

 $V = 46 \text{ m/s}$ 

$\alpha$	$\Delta C_L$	$\Delta C_D$	$\Delta C_m$
-5	0.002	0.0117	$\bar{0.0018}$
0	0.002	0.0115	$\bar{0.0018}$
5	0.002	0.0114	$\bar{0.0018}$
10	0.002	0.0114	$\bar{0.0018}$
15	0.002	0.0114	$\bar{0.0018}$
20	0.003	0.0114	$\bar{0.0018}$
25	0.003	0.0114	$\bar{0.0018}$

 $V = 22.6 \text{ m/s}$ 

$\alpha$	$\Delta C_L$	$\Delta C_D$	$\Delta C_m$
-5	0.004	0.0167	$\bar{0.0022}$
0	0.004	0.0167	$\bar{0.0023}$
5	0.004	0.0167	$\bar{0.0024}$
10	0.004	0.0167	$\bar{0.0024}$
15	0.004	0.0167	$\bar{0.0024}$
20	0.004	0.0165	$\bar{0.0024}$
25	0.004	0.0163	$\bar{0.0024}$

MODEL ASYMMETRY AND WIND TUNNEL PITCH

$$V = 76 \text{ m/s} \quad \Delta C_L = 0.003, \quad \Delta C_m = 0.005, \quad \Delta \alpha_p = \bar{0.07}^\circ$$

$$V = 46 \text{ m/s} \quad \Delta C_L = 0.003, \quad \Delta C_m = 0.005, \quad \Delta \alpha_p = \bar{0.01}^\circ$$

$$V = 22.6 \text{ m/s*} \quad \Delta C_L = 0.000, \quad \Delta C_m = 0.005, \quad \Delta \alpha_p = \bar{0.14}^\circ$$

\* Accuracy of these corrections is poor

Table 2 (concluded)STRUT INTERFERENCES (weighted mean corrections)Main strut interference (applied at each speed)

## Symmetric wing

$\alpha$	$\Delta C_L$	$\Delta C_D$	$\Delta C_m$
-5	0.001	0.0016	0.0028
0	0.005	0.0004	0.0026
5	0.008	0.0012	0.0026
10	0.012	0.0037	0.0029
15	0.015	0.0066	0.0035
20	0.014	0.0055	0.0041
25	0.019	0.0142	0.0044

## Cambered wing

$\alpha$	$\Delta C_L$	$\Delta C_D$	$\Delta C_m$
0	0.005	0.0004	0.0026
5	0.008	0.0020	0.0020
10	0.012	0.0044	0.0024
15	0.015	0.0066	0.0031
20	0.014	0.0078	0.0039
25	0.019	0.0087	0.0048

## Pitch strut interference (both wings)

$\alpha$	$\Delta C_L$	$\Delta C_D$	$\Delta C_m$
-5	0.002	0.0000	0.0008
0	0.002	0.0001	0.0008
5	0.002	0.0002	0.0008
10	0.002	0.0003	0.0008
15	0.002	0.0004	0.0008
20	0.002	0.0005	0.0008
25	0.002	0.0006	0.0008

Table 3  
SYMMETRIC WING V = 76 m/s  
 $C_{D_0} = 0.0074$

$\alpha$	$C_L$	$C_D$	$C_m$	$\bar{C}_N$	$\bar{C}_N/\alpha$	K	$x_{cp}/c$
-5.26	-0.186	0.0197	0.0036	0.187	2.037	1.547	0.5593
-4.71	-0.166	0.0173	0.0032	0.167	2.030	1.563	0.5592
-4.10	-0.142	0.0147	0.0025	0.143	1.994	1.575	0.5575
-3.63	-0.122	0.0130	0.0020	0.123	1.935	1.637	0.5563
-3.07	-0.101	0.0112	0.0017	0.101	1.893	1.620	0.5568
-2.52	-0.083	0.0100	0.0012	0.083	1.895	1.642	0.5545
-1.91	-0.062	0.0088	0.0007	0.062	1.868	1.584	0.5513
-1.50	-0.044	0.0080	0.0002	0.044	1.688	1.348	0.5445
-0.84	-0.025	0.0073	0.0002	0.025	1.712		0.5480
-0.36	-0.011	0.0070	0.0001	0.011	1.758		0.5491
0.03	0.001	0.0070	0.0001	0.001	1.917		
0.51	0.014	0.0073	0.0001	0.014	1.580		0.5471
1.00	0.032	0.0077	0.0002	0.032	1.841	1.274	0.5463
1.57	0.049	0.0082	0.0007	0.049	1.796	1.449	0.5543
2.09	0.069	0.0090	0.0007	0.069	1.899	1.462	0.5501
2.60	0.088	0.0100	0.0013	0.088	1.947	1.460	0.5548
3.22	0.108	0.0114	0.0017	0.108	1.930	1.492	0.5557
3.86	0.129	0.0131	0.0021	0.130	1.924	1.490	0.5562
4.26	0.145	0.0148	0.0026	0.146	1.960	1.531	0.5578
4.86	0.165	0.0170	0.0031	0.166	1.955	1.534	0.5587
5.08	0.178	0.0184	0.0034	0.179	2.018	1.510	0.5590
6.04	0.215	0.0242	0.0043	0.216	2.052	1.581	0.5599
7.16	0.263	0.0318	0.0054	0.265	2.120	1.534	0.5604
8.18	0.308	0.0407	0.0064	0.311	2.176	1.527	0.5606
9.36	0.360	0.0545	0.0074	0.364	2.229	1.581	0.5603
10.47	0.408	0.0663	0.0085	0.413	2.261	1.539	0.5606
11.56	0.455	0.0806	0.0092	0.462	2.289	1.538	0.5559
12.48	0.501	0.0965	0.0097	0.510	2.341	1.544	0.5590
13.59	0.547	0.1152	0.0095	0.559	2.356	1.567	0.5570
14.66	0.586	0.1323	0.0087	0.600	2.347	1.582	0.5545
15.65	0.629	0.1529	0.0092	0.647	2.368	1.600	0.5542
16.75	0.681	0.1794	0.0102	0.704	2.407	1.613	0.5545
17.75	0.723	0.2004	0.0113	0.750	2.420	1.606	0.5551
18.91	0.772	0.2292	0.0124	0.805	2.438	1.619	0.5554
19.71	0.814	0.2553	0.0134	0.852	2.478	1.627	0.5557
20.97	0.867	0.2937	0.0148	0.915	2.499	1.657	0.5562
22.12	0.921	0.3300	0.0164	0.977	2.532	1.654	0.5568
22.95	0.968	0.3635	0.0175	1.033	2.579	1.653	0.5569
24.00	1.020	0.4072	0.0188	1.097	2.620	1.672	0.5571
25.03	1.070	0.4514	0.0200	1.160	2.656	1.687	0.5572
26.01	1.110	0.4899	0.0207	1.212	2.671	1.703	0.5571

Table 3 (concluded)

CAMBERED WING V = 76 m/s

$C_{Dm} = 0.0093$

$C_{Lm} = 0.041$

$\alpha$	$C_L$	$C_D$	$C_m$	$\bar{C}_N$	$\frac{\bar{C}_N - (\bar{C}_N)_{\alpha_{des}}}{\alpha - \alpha_{des}}$	K	K'	$x_{cp}/c$
-0.05	-0.090	0.0156	0.0073	0.091	2.039			0.6211
0.50	-0.072	0.0137	0.0073	0.071	2.028			0.6414
0.99	-0.053	0.0122	0.0070	0.054	2.035			0.6721
1.47	-0.033	0.0109	0.0065	0.034	1.989			0.7370
2.05	-0.012	0.0099	0.0060	0.013	1.972			1.0400
2.59	0.008	0.0091	0.0055	0.008	1.940			0.1475
3.23	0.028	0.0088	0.0051	0.028	1.983			0.3579
3.64	0.038	0.0086	0.0048	0.038	2.123	3.598		0.4137
4.08	0.059	0.0087	0.0043	0.059	1.904	1.561		0.4671
4.56	0.076	0.0089	0.0039	0.076	1.819	1.124		0.4887
5.11	0.094	0.0094	0.0034	0.094	1.647	1.003		0.5038
5.62	0.111	0.0105	0.0036	0.111	2.111	1.086	1.061	0.5076
6.26	0.128	0.0118	0.0037	0.128	1.717	1.172	1.431	0.5113
6.75	0.144	0.0132	0.0035	0.144	1.774	1.207	1.592	0.5159
7.28	0.162	0.0146	0.0034	0.162	1.824	1.192	1.568	0.5191
7.72	0.177	0.0163	0.0031	0.178	1.851	1.225	1.639	0.5226
8.28	0.194	0.0180	0.0029	0.195	1.833	1.221	1.610	0.5251
8.76	0.209	0.0199	0.0027	0.210	1.829	1.244	1.627	0.5271
9.21	0.226	0.0220	0.0024	0.227	1.870	1.237	1.607	0.5294
9.77	0.246	0.0247	0.0019	0.247	1.895	1.241	1.587	0.5323
10.29	0.266	0.0278	0.0015	0.267	1.930	1.248	1.583	0.5344
11.30	0.304	0.0345	0.0004	0.306	1.973	1.270	1.578	0.5387
12.22	0.345	0.0429	0.0007	0.348	2.056	1.292	1.575	0.5420
13.33	0.391	0.0542	0.0022	0.395	2.108	1.327	1.587	0.5456
14.43	0.439	0.0671	0.0037	0.444	2.164	1.343	1.580	0.5484
15.56	0.485	0.0815	0.0047	0.492	2.192	1.364	1.586	0.5496
16.51	0.524	0.0957	0.0047	0.533	2.215	1.392	1.604	0.5489
17.61	0.563	0.1131	0.0049	0.574	2.211	1.444	1.650	0.5486
18.66	0.610	0.1336	0.0070	0.624	2.252	1.469	1.663	0.5513
19.76	0.661	0.1571	0.0092	0.679	2.299	1.484	1.665	0.5536
20.74	0.708	0.1801	0.0109	0.730	2.342	1.492	1.663	0.5550
21.82	0.758	0.2072	0.0126	0.786	2.381	1.506	1.667	0.5561
22.82	0.806	0.2356	0.0145	0.840	2.421	1.521	1.675	0.5574
23.79	0.855	0.2659	0.0165	0.895	2.466	1.532	1.677	0.5585
24.86	0.907	0.3005	0.0185	0.955	2.508	1.543	1.682	0.5595
26.11	0.958	0.3381	0.0204	1.016	2.523	1.561	1.694	0.5602

Table 4

SYMMETRIC WING V = 46 m/s

$$C_{D_0} = 0.00675$$

$\alpha$	$C_L$	$C_D$	$C_m$	$\bar{C}_N$	$\bar{C}_N/\alpha$	K
-5.18	0.176	0.0182	0.0024	0.177	1.958	1.554
-4.15	0.141	0.0142	0.0017	0.142	1.960	1.563
-3.19	0.104	0.0108	0.0004	0.104	1.868	1.539
-2.13	0.066	0.0083	0.0004	0.066	1.775	1.416
-1.15	0.032	0.0067	0.0006	0.032	1.594	
-0.09	0.001	0.0055	0.0006	0.001		
0.97	0.027	0.0068	0.0001	0.027	1.595	
2.07	0.062	0.0079	0.0007	0.062	1.716	1.437
2.94	0.096	0.0099	0.0013	0.096	1.871	1.584
3.94	0.133	0.0131	0.0026	0.134	1.949	1.634
5.12	0.176	0.0176	0.0035	0.177	1.981	1.577
6.10	0.220	0.0240	0.0047	0.221	2.076	1.593
7.25	0.268	0.0324	0.0059	0.270	2.134	1.589
8.30	0.313	0.0417	0.0069	0.316	2.181	1.582
9.24	0.355	0.0518	0.0079	0.359	2.226	1.582
10.39	0.400	0.0642	0.0088	0.405	2.233	1.586
11.31	0.445	0.0774	0.0097	0.452	2.290	1.573
12.36	0.492	0.0926	0.0101	0.500	2.318	1.562
13.39	0.537	0.1102	0.0100	0.548	2.345	1.578
14.46	0.581	0.1299	0.0090	0.595	2.358	1.603
15.46	0.629	0.1512	0.0099	0.647	2.398	1.603
16.75	0.677	0.1756	0.0104	0.699	2.391	1.617
17.71	0.717	0.1976	0.0116	0.743	2.404	1.628
18.69	0.765	0.2232	0.0121	0.796	2.440	1.622
19.81	0.815	0.2543	0.0136	0.853	2.467	1.633
20.82	0.862	0.2870	0.0145	0.908	2.499	1.652
21.92	0.916	0.3238	0.0163	0.971	2.538	1.654
22.85	0.966	0.3607	0.0172	1.030	2.583	1.660
23.99	1.018	0.4049	0.0180	1.095	2.615	1.681
24.91	1.068	0.4462	0.0194	1.157	2.661	1.685
25.94	1.113	0.4933	0.0201	1.217	2.688	1.718

Table 4 (concluded)

CAMBERED WING V = 46 m/s

$\alpha$	$C_L$	$C_D$	$C_m$	$\bar{C}_N$	$\frac{\bar{C}_N - (\bar{C}_N)_{\alpha_{des}}}{\alpha - \alpha_{des}}$	K
-0.18	0.091	0.0158	0.0063	0.092	2.012	
0.85	0.054	0.0126	0.0060	0.055	1.997	
1.88	0.018	0.0102	0.0051	0.019	1.992	
2.85	0.020	0.0086	0.0042	0.020	1.888	
3.89	0.057	0.0081	0.0034	0.057	1.772	1.839
5.05	0.094	0.0088	0.0026	0.094	1.494	1.011
5.92	0.120	0.0115	0.0033	0.120	1.825	1.420
7.10	0.154	0.0143	0.0033	0.154	1.718	1.388
8.07	0.188	0.0179	0.0028	0.189	1.826	1.370
9.24	0.226	0.0227	0.0021	0.227	1.842	1.354
10.27	0.262	0.0281	0.0013	0.263	1.880	1.347
11.23	0.299	0.0344	0.0004	0.301	1.938	1.338
12.19	0.339	0.0425	0.0007	0.342	2.007	1.346
13.25	0.385	0.0530	0.0022	0.389	2.078	1.351
14.41	0.433	0.0657	0.0037	0.438	2.124	1.361
15.41	0.476	0.0787	0.0048	0.482	2.166	1.375
16.43	0.517	0.0927	0.0051	0.525	2.188	1.392
17.43	0.557	0.1094	0.0048	0.568	2.207	1.433
18.51	0.602	0.1300	0.0068	0.616	2.236	1.473
19.58	0.651	0.1519	0.0088	0.668	2.280	1.483
20.64	0.696	0.1745	0.0109	0.717	2.305	1.500
21.66	0.747	0.2024	0.0127	0.774	2.359	1.519
22.77	0.799	0.2324	0.0145	0.832	2.400	1.531
23.83	0.850	0.2644	0.0165	0.890	2.442	1.545
24.87	0.901	0.2982	0.0187	0.949	2.485	1.524
25.77	0.946	0.3318	0.0201	1.002	2.525	1.573

Table 5

SYMMETRIC WING V = 22.6 m/s TRANSITION FIXED

$$C_{D_0} = 0.0092$$

$\alpha$	$C_L$	$C_D$	$C_m$	$\bar{C}_N$	$\bar{C}_N/\alpha$	K
-5.36	0.187	0.0216	0.0036	0.188	2.010	1.542
-4.26	0.143	0.0170	0.0024	0.144	1.937	1.659
-3.33	0.107	0.0144	0.0014	0.108	1.858	1.976
-2.25	0.075	0.0119	0.0007	0.075	1.910	2.088
-1.34	0.041	0.0101	0.0005	0.041	1.753	2.329
<hr/>						
-0.26	0.008	0.0098	0.0000	0.008	1.763	
0.83	0.022	0.0100	0.0000	0.022	1.519	
1.89	0.058	0.0101	0.0002	0.058	1.758	1.164
2.80	0.090	0.0120	0.0008	0.090	1.842	1.504
3.90	0.129	0.0145	0.0015	0.130	1.910	1.385
<hr/>						
4.82	0.167	0.0182	0.0023	0.168	1.997	1.404
5.96	0.209	0.0244	0.0031	0.210	2.019	1.514
6.98	0.254	0.0320	0.0044	0.256	2.101	1.537
8.13	0.303	0.0413	0.0054	0.306	2.157	1.521
9.24	0.350	0.0526	0.0062	0.354	2.195	1.541
<hr/>						
10.26	0.395	0.0653	0.0070	0.401	2.239	1.564
11.30	0.442	0.0789	0.0077	0.449	2.277	1.552
12.32	0.483	0.0936	0.0077	0.492	2.288	1.574
13.34	0.524	0.1107	0.0071	0.535	2.298	1.608
14.29	0.570	0.1301	0.0075	0.585	2.346	1.619
<hr/>						
15.57	0.616	0.1517	0.0079	0.634	2.333	1.634
16.58	0.660	0.1734	0.0087	0.683	2.360	1.640
17.55	0.707	0.1956	0.0099	0.733	2.393	1.622
18.54	0.749	0.2214	0.0106	0.781	2.414	1.645
19.48	0.805	0.2536	0.0120	0.843	2.479	1.641
<hr/>						
20.78	0.859	0.2876	0.0131	0.905	2.495	1.641
21.75	0.907	0.3203	0.0141	0.961	2.532	1.645
22.78	0.959	0.3581	0.0154	1.023	2.573	1.650
23.90	1.006	0.4005	0.0160	1.082	2.594	1.682
24.97	1.052	0.4423	0.0171	1.140	2.616	1.702
<hr/>						
25.86	1.097	0.4784	0.0176	1.196	2.650	1.696

Table 5 (concluded)CAMBERED WING V = 22.6 m/s TRANSITION FIXED

$\alpha$	$C_L$	$C_D$	$C_m$	$\bar{C}_N$	$\frac{\bar{C}_N - (\bar{C}_N)_{\alpha_{des}}}{\alpha - \alpha_{des}}$	K
-0.11	0.084	0.0171	0.0068	0.085	1.912	
0.99	0.047	0.0144	0.0065	0.048	1.905	
1.85	0.013	0.0124	0.0057	0.013	1.812	
2.89	0.021	0.0116	0.0051	0.020	1.780	
3.90	0.051	0.0111	0.0043	0.051	1.827	
4.91	0.083	0.0119	0.0040	0.083	1.829	1.697
5.80	0.115	0.0133	0.0037	0.115	2.281	1.343
6.94	0.144	0.0160	0.0035	0.144	1.712	1.420
8.00	0.182	0.0190	0.0033	0.183	1.853	1.281
9.01	0.216	0.0232	0.0026	0.217	1.880	1.300
10.12	0.254	0.0282	0.0017	0.255	1.904	1.276
11.14	0.293	0.0347	0.0005	0.295	1.959	1.286
12.15	0.335	0.0439	0.0006	0.338	2.028	1.339
13.20	0.375	0.0536	0.0020	0.379	2.056	1.367
14.26	0.419	0.0665	0.0033	0.424	2.104	1.414
15.26	0.459	0.0787	0.0041	0.467	2.131	1.429
16.34	0.500	0.0934	0.0040	0.509	2.145	1.459
17.29	0.540	0.1103	0.0054	0.551	2.179	1.502
18.47	0.590	0.1302	0.0071	0.604	2.214	1.505
19.41	0.634	0.1509	0.0089	0.652	2.260	1.527
20.60	0.692	0.1772	0.0108	0.714	2.318	1.519
21.63	0.742	0.2042	0.0131	0.769	2.366	1.534
22.65	0.793	0.2342	0.0148	0.827	2.416	1.550
23.87	0.846	0.2660	0.0170	0.887	2.442	1.554
24.94	0.896	0.3021	0.0190	0.945	2.481	1.580
25.69	0.937	0.3321	0.0203	0.994	2.526	1.593

Table 6INCIDENCES FOR PRESSURE MEASUREMENTS

Symmetric wing:  $\alpha = (-5^\circ), 0^\circ, 2.5^\circ, 5^\circ, 7.5^\circ, 10^\circ, 12.5^\circ, 15^\circ, 17.5^\circ, 20^\circ, (25^\circ)$

$\alpha = -5^\circ, 0^\circ, 5^\circ$  with dummy main strut.

Cambered wing:  $\alpha = (4^\circ), 5.32^\circ, (6^\circ), 7.5^\circ, 10^\circ, 12.5^\circ, 15^\circ, 17.5^\circ, 20^\circ, 25^\circ$

Incidences in brackets indicate that complete analysis has not been done and results are not included.

Table 7CAMBERED WING

$$\alpha_{des} = 5.32^\circ \quad (C_L)_{des} = 0.1 \quad (x_{cp}/c)_{des} = 0.533$$

$$V = 76 \text{ m/s} \quad (C_L)_{\alpha_{des}} = 0.100 \quad (x_{cp}/c)_{\alpha_{des}} = 0.504$$

$$V = 46 \text{ m/s} \quad (C_L)_{\alpha_{des}} = 0.101$$

$$V = 22.6 \text{ m/s} \quad (C_L)_{\alpha_{des}} = 0.096$$

Table 8

 $C_N(x/c)$  FOR SYMMETRIC WING  $V = 76 \text{ m/s}$ 

$x/c$	$2.5^\circ$	$5^\circ$	$7.5^\circ$	$10^\circ$	$12.5^\circ$	$15^\circ$	$17.5^\circ$	$20^\circ$
0.06	0.1180	0.2454	0.3954	0.5367	0.7117	0.8808	1.1001	1.3275
0.10	0.1184	0.2483	0.4038	0.5533	0.7317	0.9089	1.1271	1.3497
0.15	0.1231	0.2559	0.4031	0.5684	0.7424	0.9379	1.1524	1.3932
0.20	0.1195	0.2514	0.4030	0.5732	0.7516	0.9448	1.1562	1.3792
0.25	0.1206	0.2535	0.4013	0.5685	0.7439	0.9382	1.1533	1.3685
0.30	0.1220	0.2578	0.4042	0.5617	0.7313	0.9285	1.1279	1.3385
0.35	0.1245	0.2464	0.3874	0.5529	0.7181	0.9088	1.0883	1.3013
0.40	0.1168	0.2425	0.3845	0.5361	0.7029	0.8761	1.0495	1.2517
0.45	0.1128	0.2390	0.3733	0.5251	0.6810	0.8452	1.0172	1.2056
0.50	0.1122	0.2371	0.3692	0.5251	0.6763	0.8303	0.9973	1.1735
0.55	0.1100	0.2333	0.3654	0.5194	0.6742	0.8190	0.9882	1.1241
0.60	0.0976	0.2166	0.3420	0.4868	0.6298	0.7704	0.8946	1.0135
0.65	0.0923	0.2010	0.3088	0.4465	0.5719	0.7071	0.8043	0.9039
0.70	0.0784	0.1834	0.2822	0.3982	0.5105	0.6286	0.6775	0.8295
0.75	0.0693	0.1580	0.2500	0.3532	0.4482	0.5329	0.5872	0.7580
0.80	0.0563	0.1327	0.2094	0.3002	0.3830	0.4420	0.5342	0.6656
0.85	0.0494	0.1126	0.1713	0.2486	0.3174	0.3571	0.4698	0.5667
0.90	0.0388	0.0822	0.1362	0.1910	0.2416	0.2889	0.3850	0.4701
0.95	0.0220	0.0579	0.0852	0.1301	0.1565	0.2017	0.2661	0.3162
$\bar{C}_N$	= 0.0783	0.1680	0.2641	0.3771	0.4820	0.5969	0.7068	0.8478
$x_{cp}/c$	= 0.5509	0.5630	0.5600	0.5607	0.5589	0.5489	0.5541	0.5557

$$\bar{C}_N = \frac{2sc}{S} \int_0^1 \frac{s(x/c)}{s} C_N\left(\frac{x}{c}\right) d\left(\frac{x}{c}\right)$$

$$\frac{x_{cp}}{c} = \frac{\int_0^1 \frac{x}{c} \frac{s(x/c)}{s} C_N\left(\frac{x}{c}\right) d\left(\frac{x}{c}\right)}{\int_0^1 \frac{s(x/c)}{s} C_N\left(\frac{x}{c}\right) d\left(\frac{x}{c}\right)}$$

Table 8 (concluded)

 $C_N(x/c)$  FOR CAMBERED WING  $V = 76 \text{ m/s}$ 

$x/c$	$\alpha = 5.32^\circ$	$7.5^\circ$	$10^\circ$	$12.5^\circ$	$15^\circ$	$17.5^\circ$	$20^\circ$	$25^\circ$
0.06	0.2843	0.3910	0.5371	0.6991	0.8341	0.9736	1.1735	1.5371
0.10	0.2582	0.3685	0.5098	0.6410	0.8151	0.9690	1.1415	1.5081
0.15	0.2254	0.3381	0.4793	0.6122	0.7814	0.9269	1.1046	1.5224
0.20	0.2028	0.3107	0.4461	0.5888	0.7522	0.9186	1.0998	1.5032
0.25	0.1818	0.2903	0.4220	0.5562	0.7253	0.8893	1.0807	1.4803
0.30	0.1683	0.2684	0.4024	0.5394	0.7419	0.8551	1.0503	1.4509
0.35	0.1611	0.2676	0.3973	0.5278	0.6893	0.8452	1.0317	1.4343
0.40	0.1549	0.2556	0.3838	0.5049	0.6665	0.8090	0.9871	1.3755
0.45	0.1447	0.2562	0.3719	0.4855	0.6523	0.7925	0.9819	1.3042
0.50	0.1403	0.2491	0.3568	0.4781	0.6287	0.7915	0.9571	1.2738
0.55	0.1333	0.2286	0.3506	0.4767	0.6066	0.7750	0.9259	1.2477
0.60	0.1188	0.2034	0.3185	0.4424	0.5863	0.7217	0.8535	1.1771
0.65	0.1046	0.1661	0.2799	0.3932	0.5361	0.6476	0.7865	1.0814
0.70	0.0970	0.1638	0.2621	0.3528	0.4775	0.5772	0.6824	0.9537
0.75	0.0876	0.1469	0.2298	0.3388	0.4258	0.4889	0.5892	0.8515
0.80	0.0640	0.1105	0.1877	0.2620	0.3582	0.4040	0.5260	0.7362
0.85	0.0522	0.0856	0.1511	0.2200	0.2859	0.3176	0.4370	0.6378
0.90	0.0330	0.0611	0.0984	0.1541	0.2184	0.2384	0.3430	0.5027
0.95	0.0184	0.0423	0.0693	0.0967	0.1404	0.1863	0.2412	0.3459
$\bar{C}_N = 0.099$		0.1658	0.2537	0.3444	0.4602	0.5535	0.6836	0.9509
$x_{cp}/c = 0.5090$		0.5222	0.5304	0.5408	0.5495	0.5419	0.5518	0.5538

$$\bar{C}_N = \frac{2sc}{S} \int_0^1 \frac{s(x/c)}{s} C_N\left(\frac{x}{c}\right) d\left(\frac{x}{c}\right) \left[ = C_L \cos(\alpha - \alpha_{des}) + C_D \sin(\alpha - \alpha_{des}) \right]$$

$$\frac{x_{cp}}{c} = \frac{\int_0^1 \frac{x}{c} \frac{s(x/c)}{s} C_N\left(\frac{x}{c}\right) d\left(\frac{x}{c}\right)}{\int_0^1 \frac{s(x/c)}{s} C_N\left(\frac{x}{c}\right) d\left(\frac{x}{c}\right)}$$

### LIST OF SYMBOLS

$a$	linear component of normal force
$A$	aspect ratio = $b^2/S$
$b$	wing span at trailing edge
$B(x/c)$	centreline thickness at $x/c$
$c$	wing centreline chord
$C_D$	drag coefficient = drag/ $qS$
$C_{D_0}$	minimum drag coefficient of symmetric wing
$C_{D_m}$	minimum drag coefficient of cambered wing
$C_L$	lift coefficient = lift/ $qS$
$C_{L_m}$	value of $C_L$ at which $C_D = C_{D_m}$
$C_m$	pitching moment coefficient = $PM/qSc$ . Moment about 0.54c
$\bar{C}_N$	modified normal force coefficient = $C_L \cos(\alpha - \alpha_{des}) + C_D \sin(\alpha - \alpha_{des})$
$C_N(x/c)$	local normal force coefficient = $\frac{1}{l} \int_{-l}^l \lambda(\eta) d\eta$
$C_p$	pressure coefficient
$C_{p_{min}}$	peak suction on wing upper surface (see Fig 19a)
$K$	induced drag factor = $\pi A(C_D - C_{D_0})/C_L^2$
$K'$	drag polar parameter = $\pi A(C_D - C_{D_m})/(C_D - C_{L_m})^2$
$\lambda, \lambda(\eta)$	local loading = $-(C_{p_U} - C_{p_L})$
$p$	parameter for approximating local camber surface by circular arc (see Fig 30)
$q$	dynamic pressure = $\frac{1}{2} \rho V^2$
$R$	Reynolds number based on planform centreline chord
$s(x/c)$	wing local semispan
$s$	(= $s(1)$ ) wing trailing-edge semispan
$S$	wing area
$V$	tunnel wind velocity
$x$ $y$ $z$	cartesian coordinates. Origin at apex of symmetric wing. $x$ positive downstream, $y$ positive to starboard, $z$ positive upwards
$\alpha$	wing angle of incidence (defined by line joining apex and centre of the trailing edge)
$\Delta C_p$	correction to $C_p$ derived from symmetric wing $\alpha = 0^\circ$ results
$\Delta C_N(x/c)$	correction to $C_N(x/c)$ derived from symmetric wing $\alpha = 0^\circ$ results
$\eta$	non-dimensionalised spanwise coordinate = $y/s(x/c)$
$\eta - C_{p_{min}}$	spanwise position of peak suction $C_{p_{min}}$
$\rho$	density of air

LIST OF SYMBOLS (concluded)Subscripts

att experimental value at design attachment incidence for cambered wing  
des theoretical value at design attachment incidence for cambered wing  
cp centre of pressure  
U upper surface  
L lower surface  
VB vortex breakdown  
vol due to volume (thickness) distribution  
 $\alpha_{des}$  at the theoretical design incidence

REFERENCES

<u>No.</u>	<u>Author</u>	<u>Title, etc</u>
1	Patricia J. Davies	The design of a series of warped slender wings for subsonic speeds. RAE Technical Report 71173 (ARC CP No.1263) (1971)
2	P.J. Butterworth P. Lee	Wind tunnel tests on cambered wings of mild gothic planform. ARC R & M No.3827 (1978)
3	J.E. Barnesby	Flow past conically-cambered slender delta wings with leading-edge separation. RAE Technical Report 72179 (ARC R & M No.3748) (1972)
4	P.B. Earnshaw	Low-speed wind-tunnel tests on a series of cambered ogee wings. RAE Technical Note Aero 2928 (1963)
5	D.A. Lovell	A generalised programme for the processing of low-speed wind-tunnel mechanical-balance force and moment data. RAE Technical Report 70174 (1970)
6	H.C. Garner (Editor)	Subsonic wind tunnel wall corrections. AGARDograph 109 (1966)
7		Catalogue of digital computer programs in fluid dynamics. ESDU 500.201 (1972)
8	D.S. Woodward	Further work on the integration of closed loops specified only as discrete data points. RAE Technical Report 73177 (1974)
9	D.A. Kirby	An experimental investigation of the effect of planform shape on the subsonic longitudinal stability characteristics of slender wings. ARC R & M No.3568 (1967)
10	D.A. Kirby D.L.I. Kirkpatrick	An experimental investigation of the effect of thickness on the subsonic longitudinal stability characteristics of delta wings of 70 deg sweep-back. ARC R & M No.3673 (1969)

REFERENCES (concluded)

<u>No.</u>	<u>Author</u>	<u>Title, etc</u>
11	P.J. Butterworth	Unpublished work.
12	P.J. Butterworth	Low-speed wind-tunnel tests on a family of cambered wings of mild gothic planform of aspect ratio 1.4. ARC CP No.1163 (1970)
13	Patricia J. Davies	An assessment of the accuracy of subsonic linearised theory for the design of warped slender wings. RAE Technical Report 73159 (1974)
14	M.P. Carr	The calculation of warp to produce a given load and pressures due to a given thickness on thin slender wings in subsonic flow. Handley Page APRO Report 99 (1968)
15	A. Roberts K. Rundle	Computation of incompressible flow about bodies and thick wings using the spline mode system. ARC 33775, BAC Report Aero MA19 (1972)
16	D.L.I. Kirkpatrick	Analysis of the static pressure distribution on a delta wing in subsonic flow. ARC R & M No.3619 (1968)
17	R.T. Jones	Properties of low-aspect-ratio pointed wings at speeds below and above the speed of sound. NACA Technical Note 1032 (1946)
18	N.C. Lambourne D.W. Bryer	The bursting of leading-edge vortices - Some observations and discussion of the phenomenon. ARC 22775, FM 3085 (1961)
19	D.J. Kettle	Unpublished work.
20	D.J. Kettle	Private communication.

Fig 1

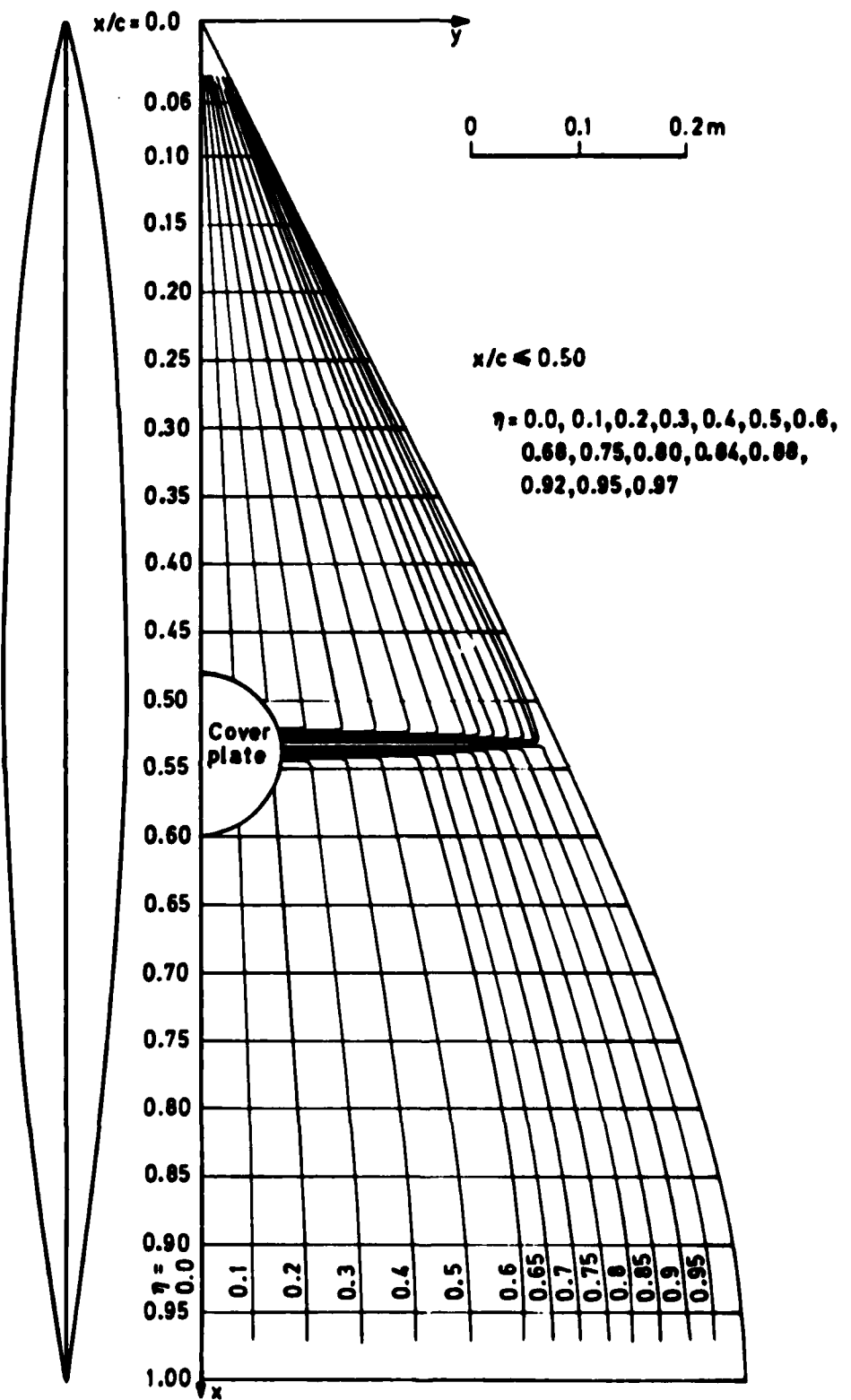
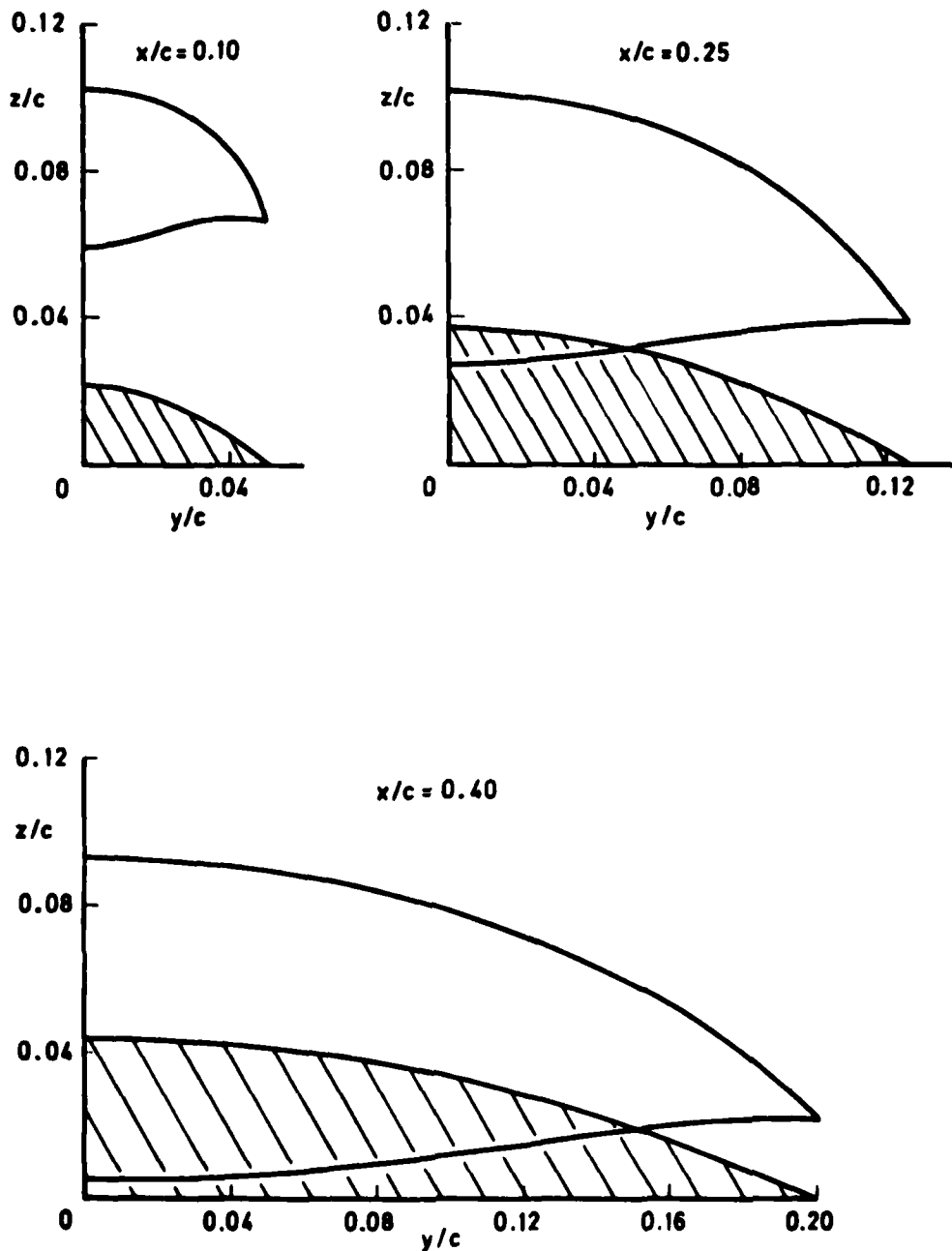


Fig 1 Planform, centre line thickness distribution and location of hypodermic tubes on upper surface of models

Fig 2a



Hatched areas denote upper half of symmetric wing  $[z = B(x/c)(1 - (y/s(x))^2)]$   
Cambered wing sections at attachment incidence

Fig 2a Typical spanwise sections of cambered wing and thickness distribution

Fig 2b

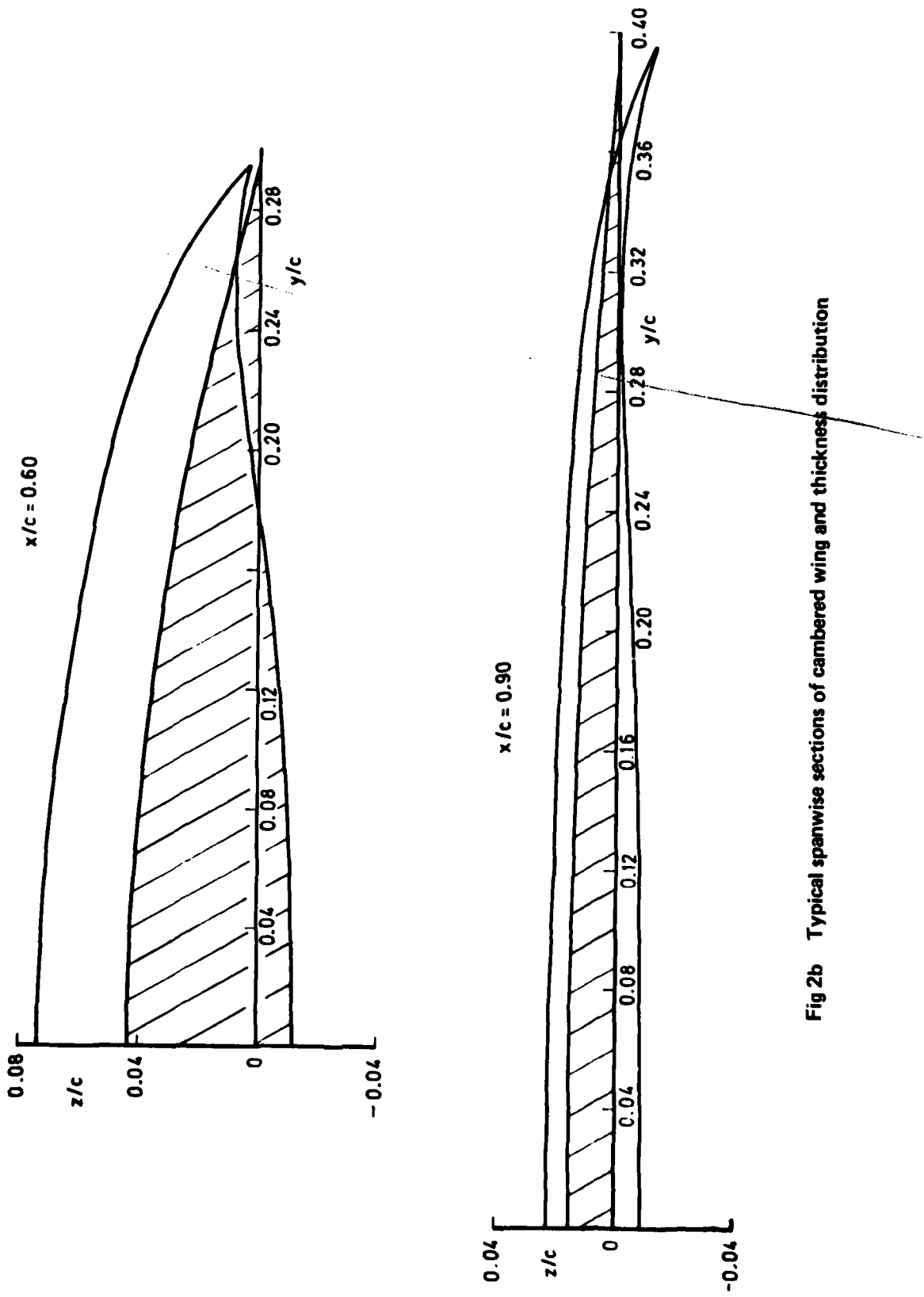
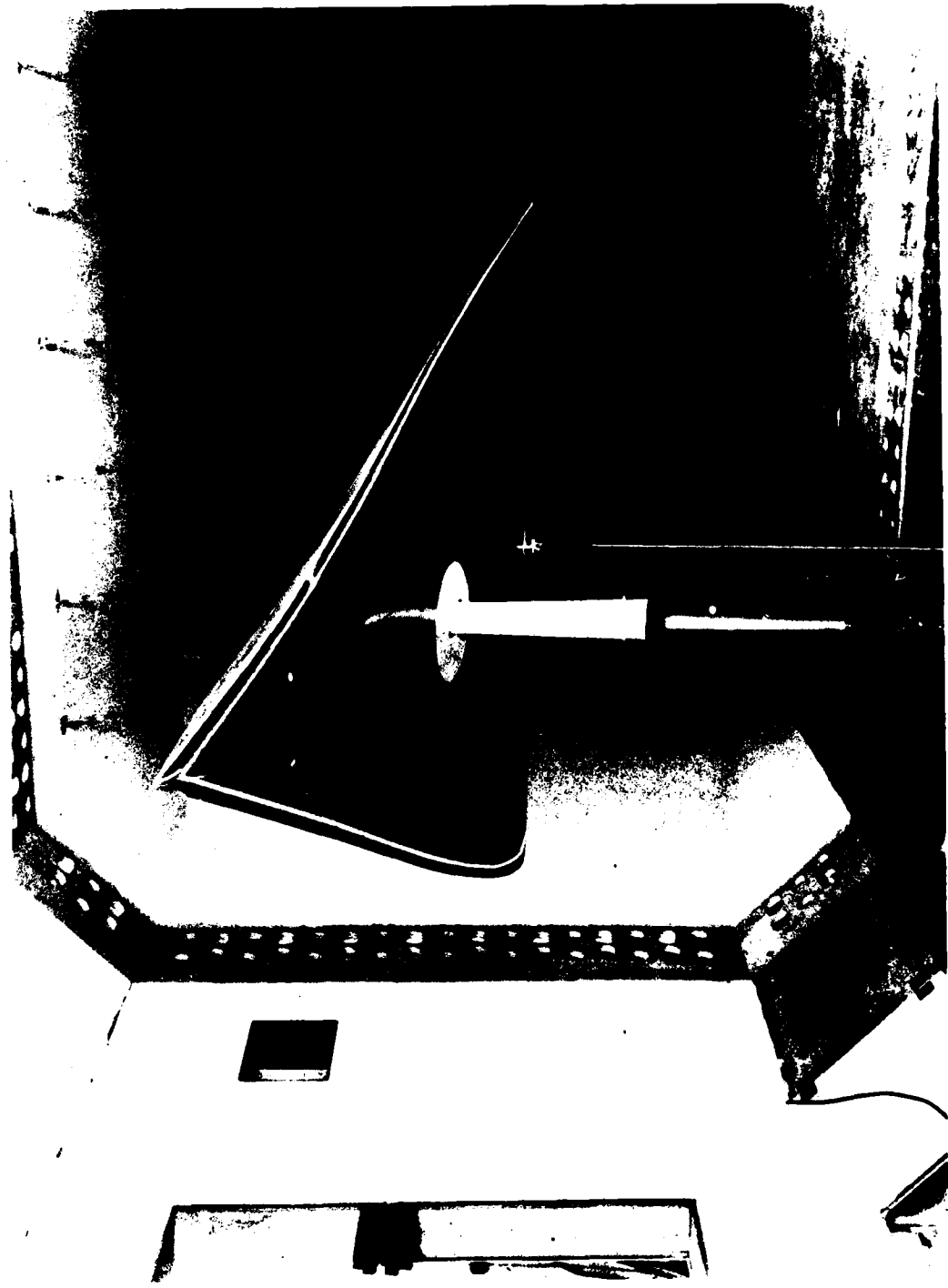


Fig 2b Typical spanwise sections of cambered wing and thickness distribution

**Fig 3**



**Fig 3** The cambered wing mounted in the No.2 11½ ft × 8½ ft low-speed wind tunnel

Fig 4a&b

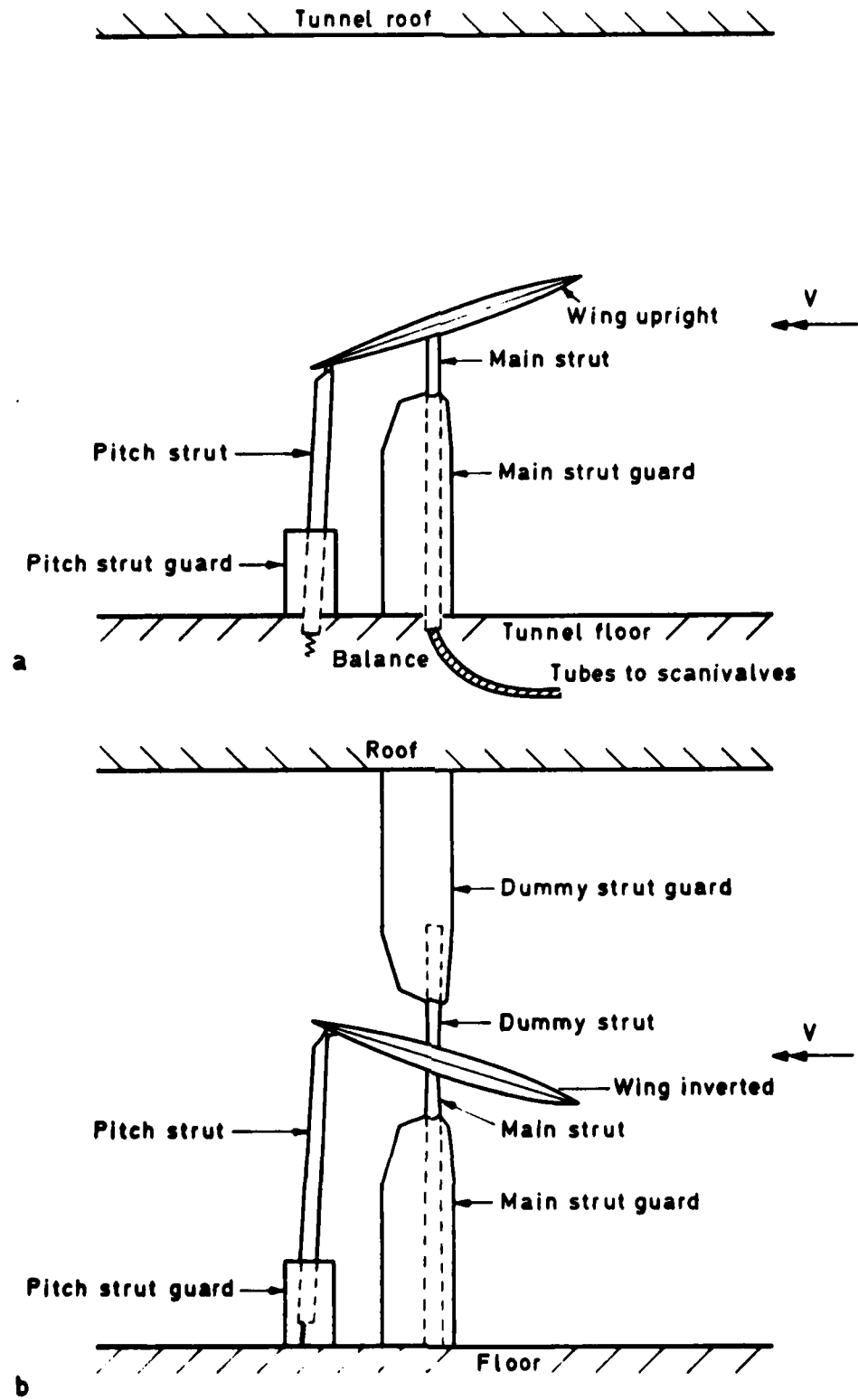


Fig 4a&b Schematic arrangement of model mounted in tunnel

Fig 5

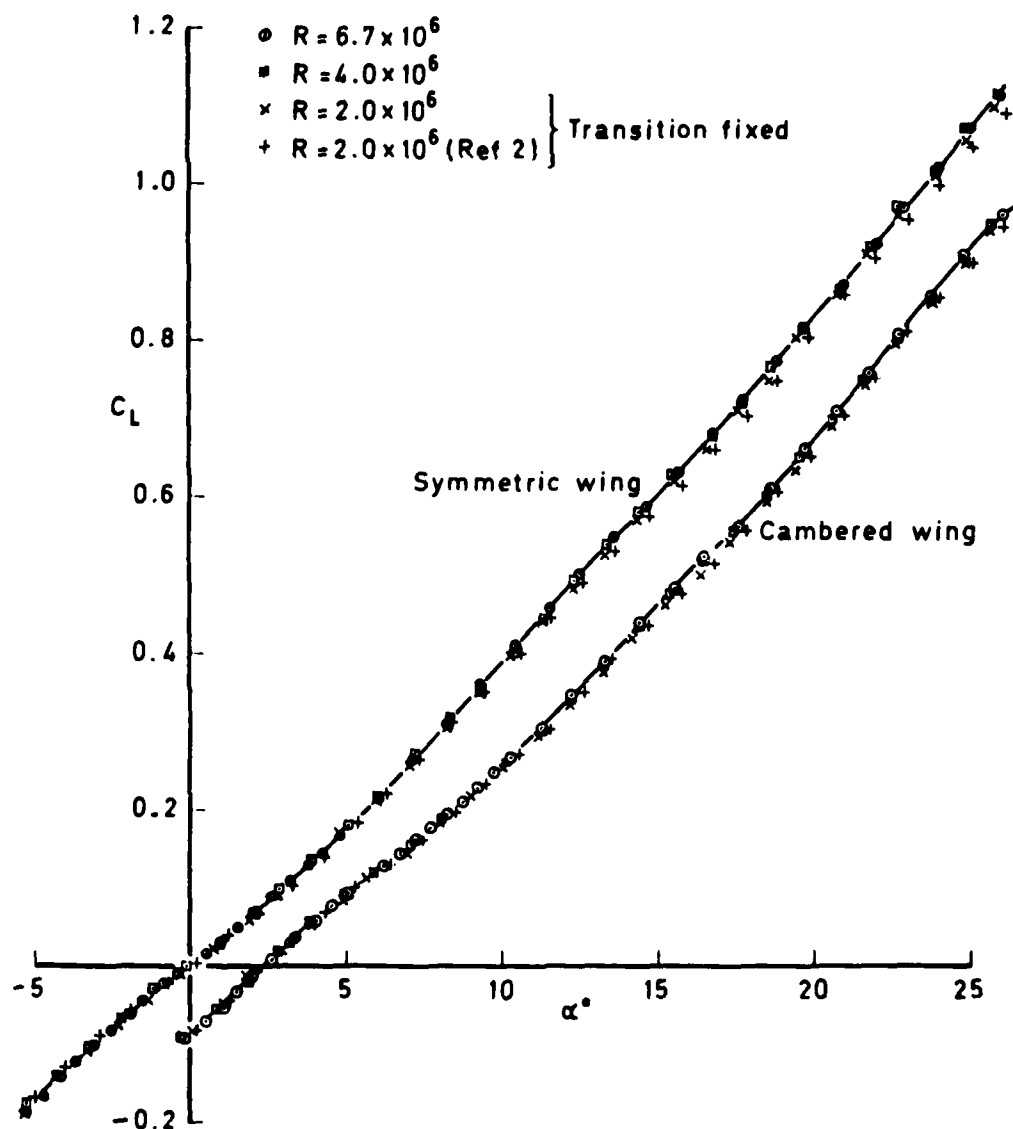


Fig 5 Comparison of lift characteristics at various speeds and Reynolds numbers

Fig 6

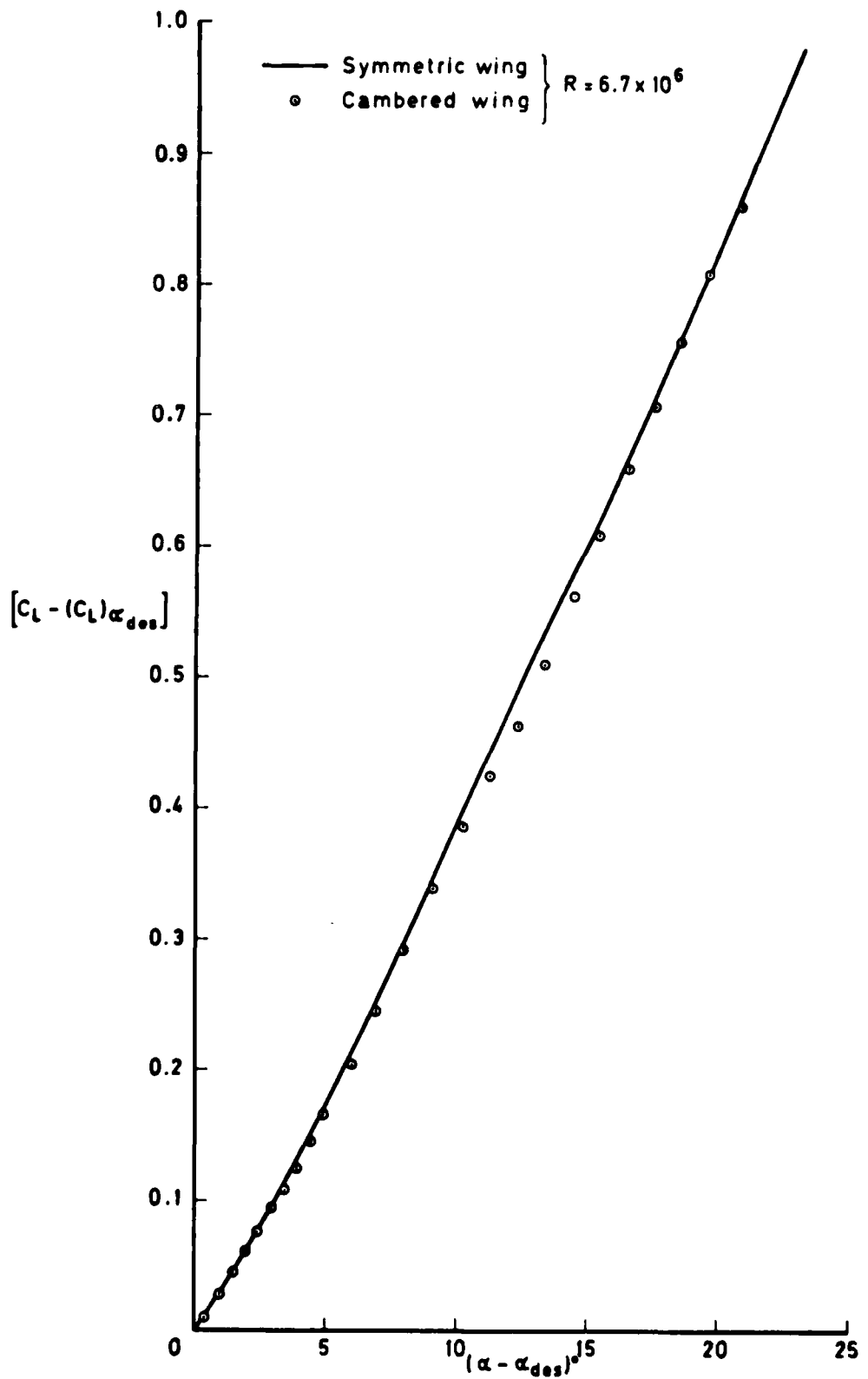


Fig 6 Collapse of lift data

Fig 7

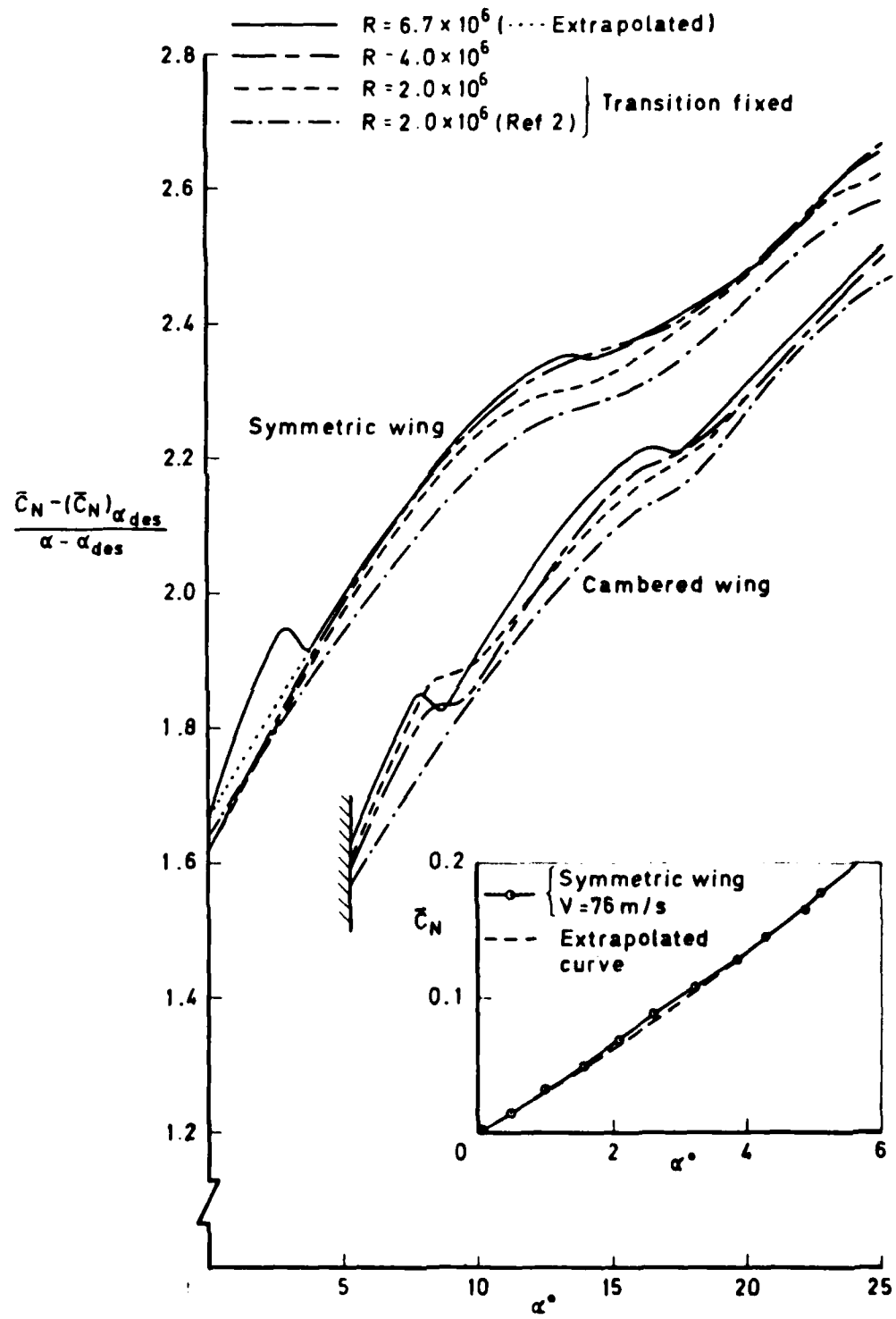


Fig 7 Analysis of normal force characteristics

Fig 8

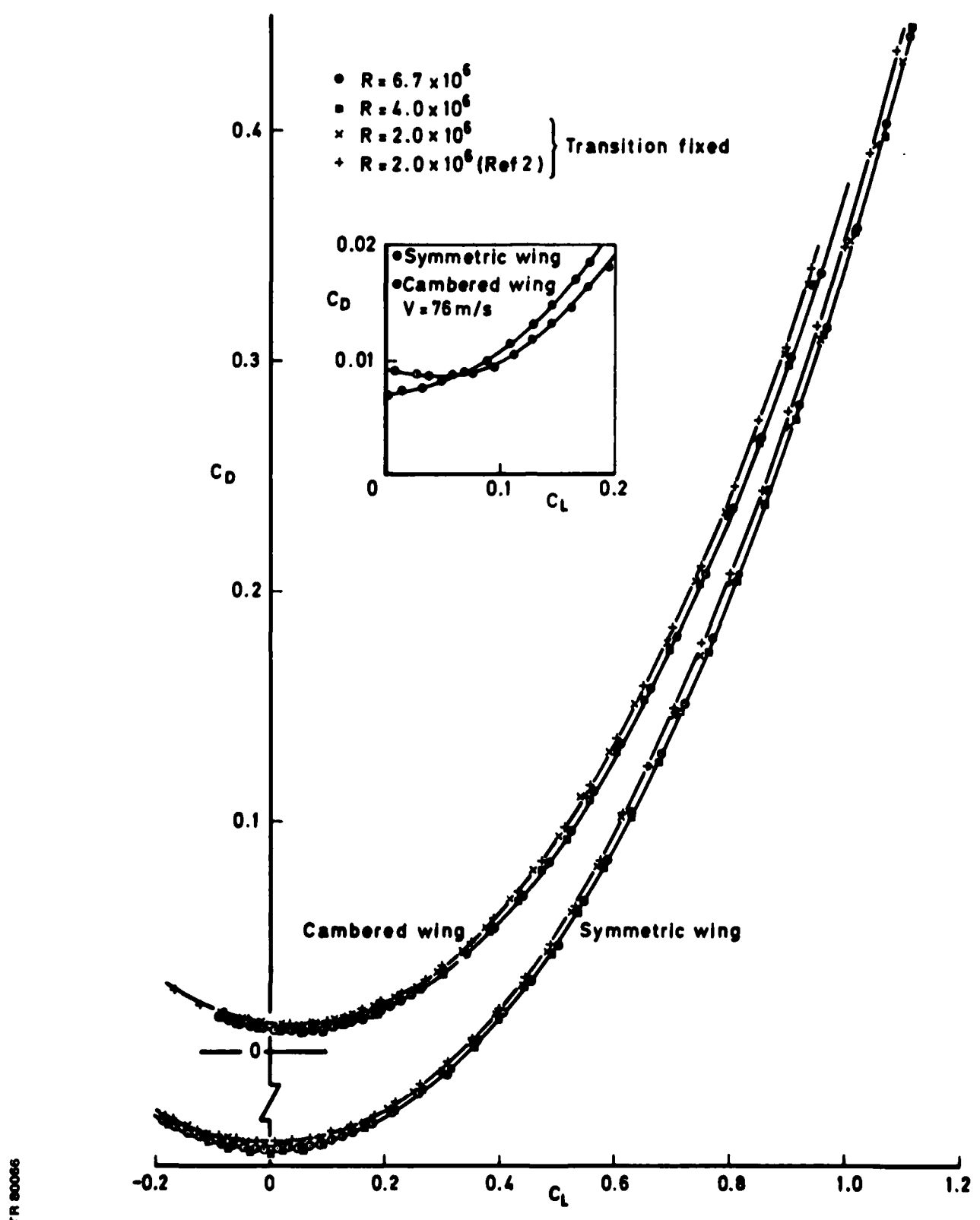
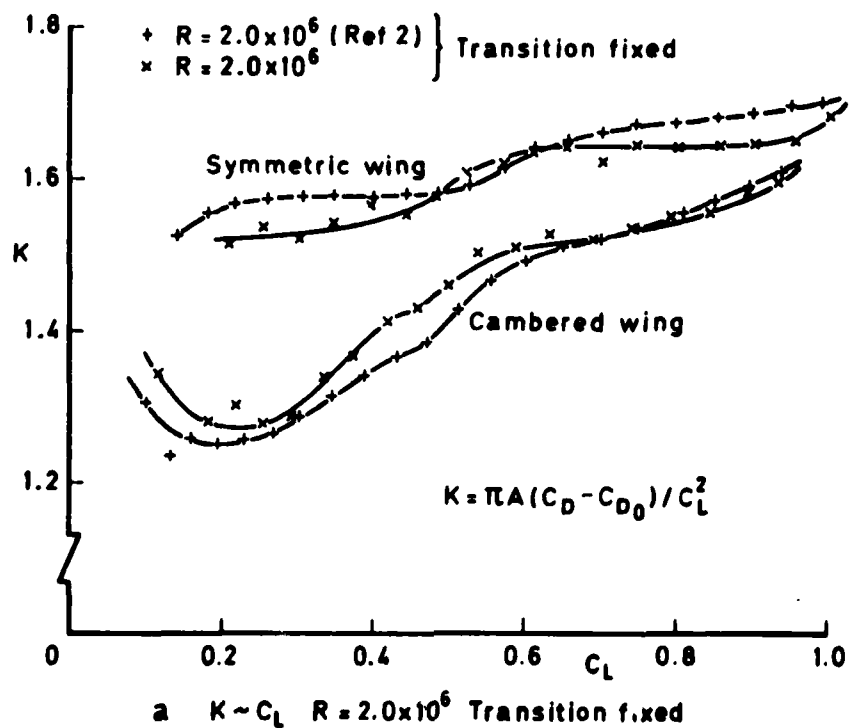
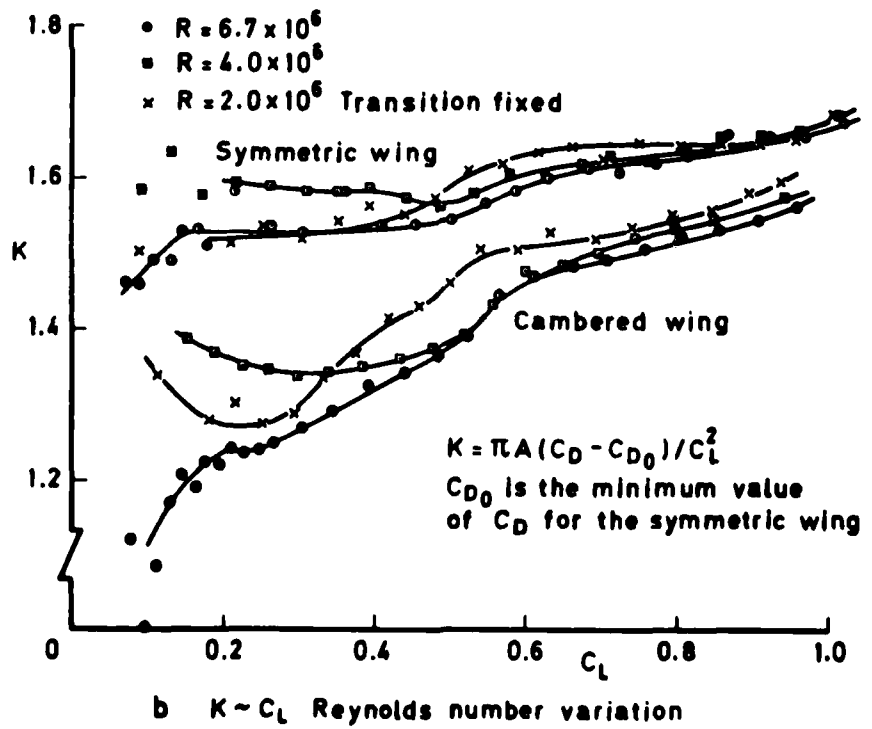


Fig 8 Comparison of drag polars

Fig 9a&b



a  $K \sim C_L$   $R = 2.0 \times 10^6$  Transition f.xed



b  $K \sim C_L$  Reynolds number variation

Fig 9a&b Lift-dependent drag factor  $K \sim C_L$

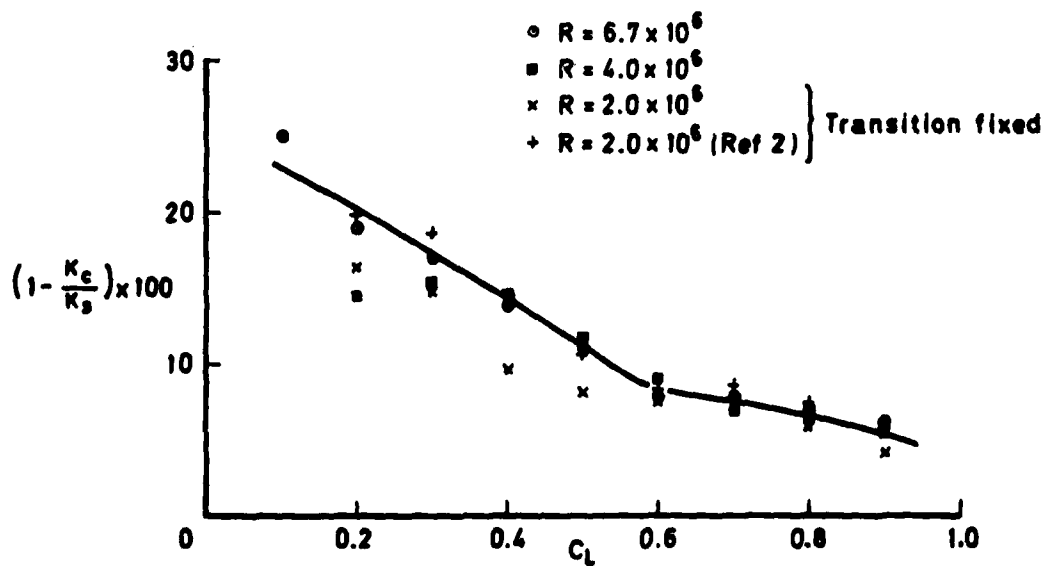


Fig 10 Reduction in  $K$  achieved by camber

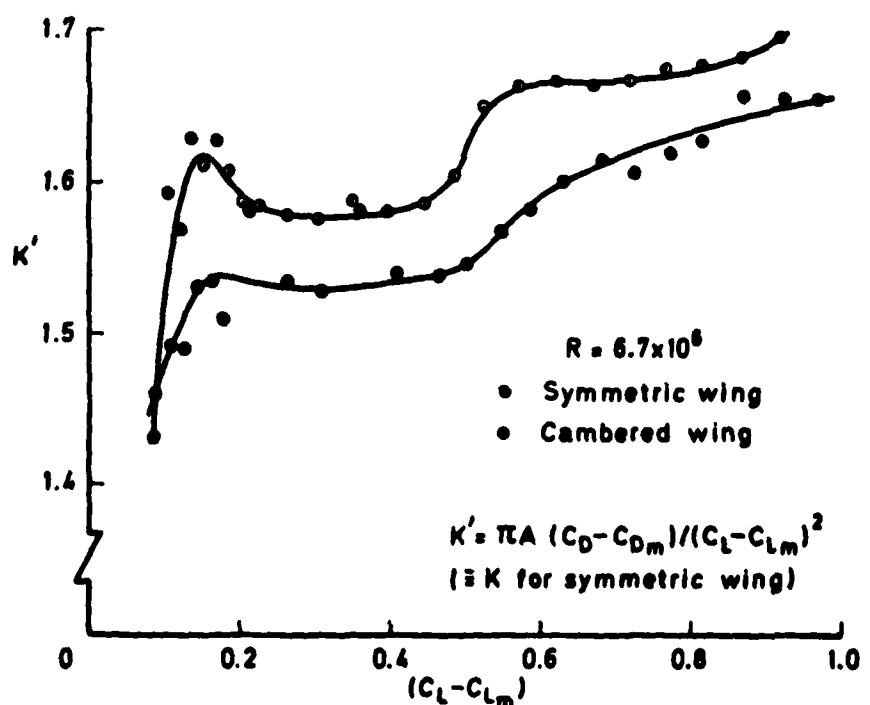


Fig 11  $K'$  characteristics

Fig 12a&b

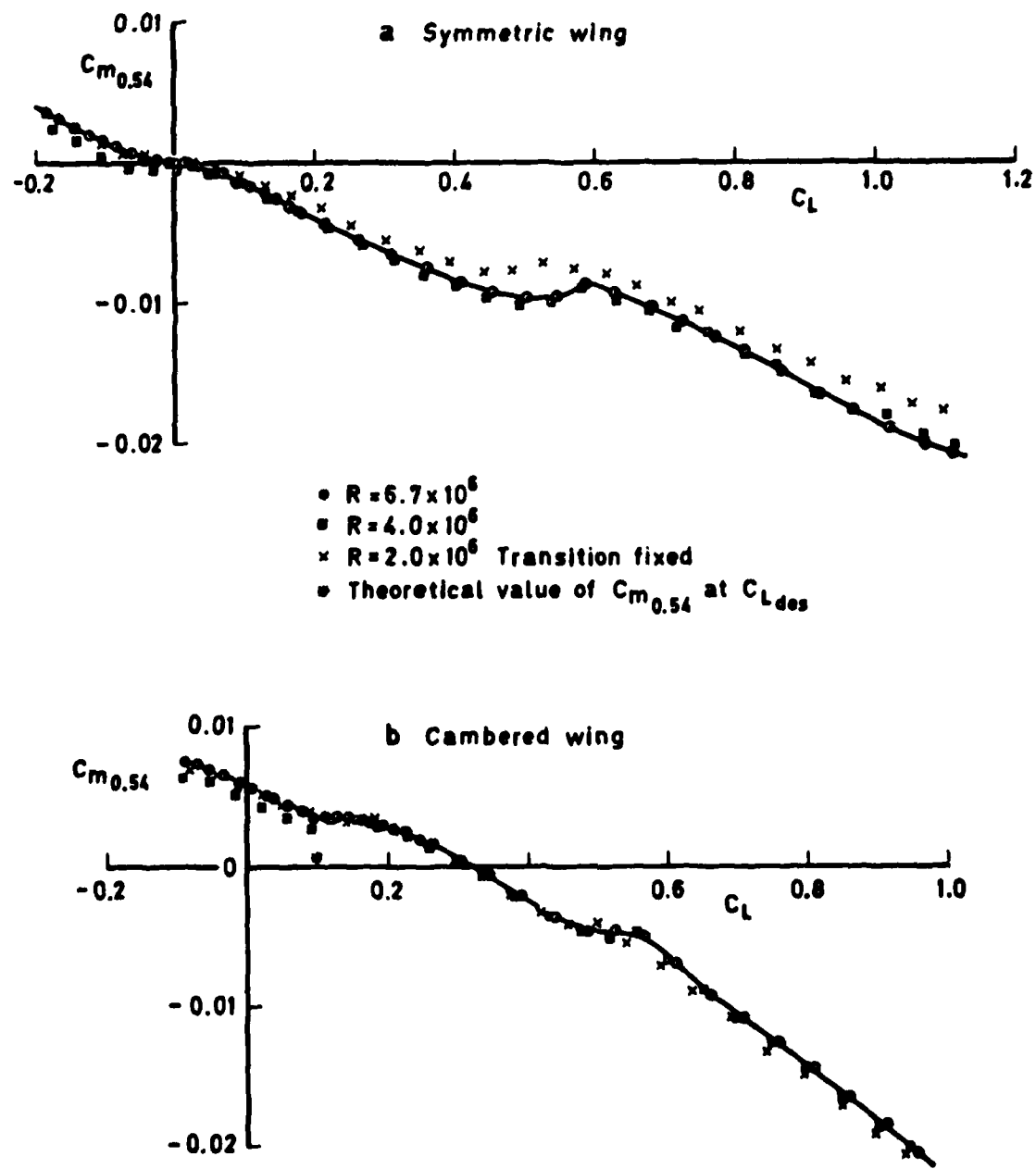
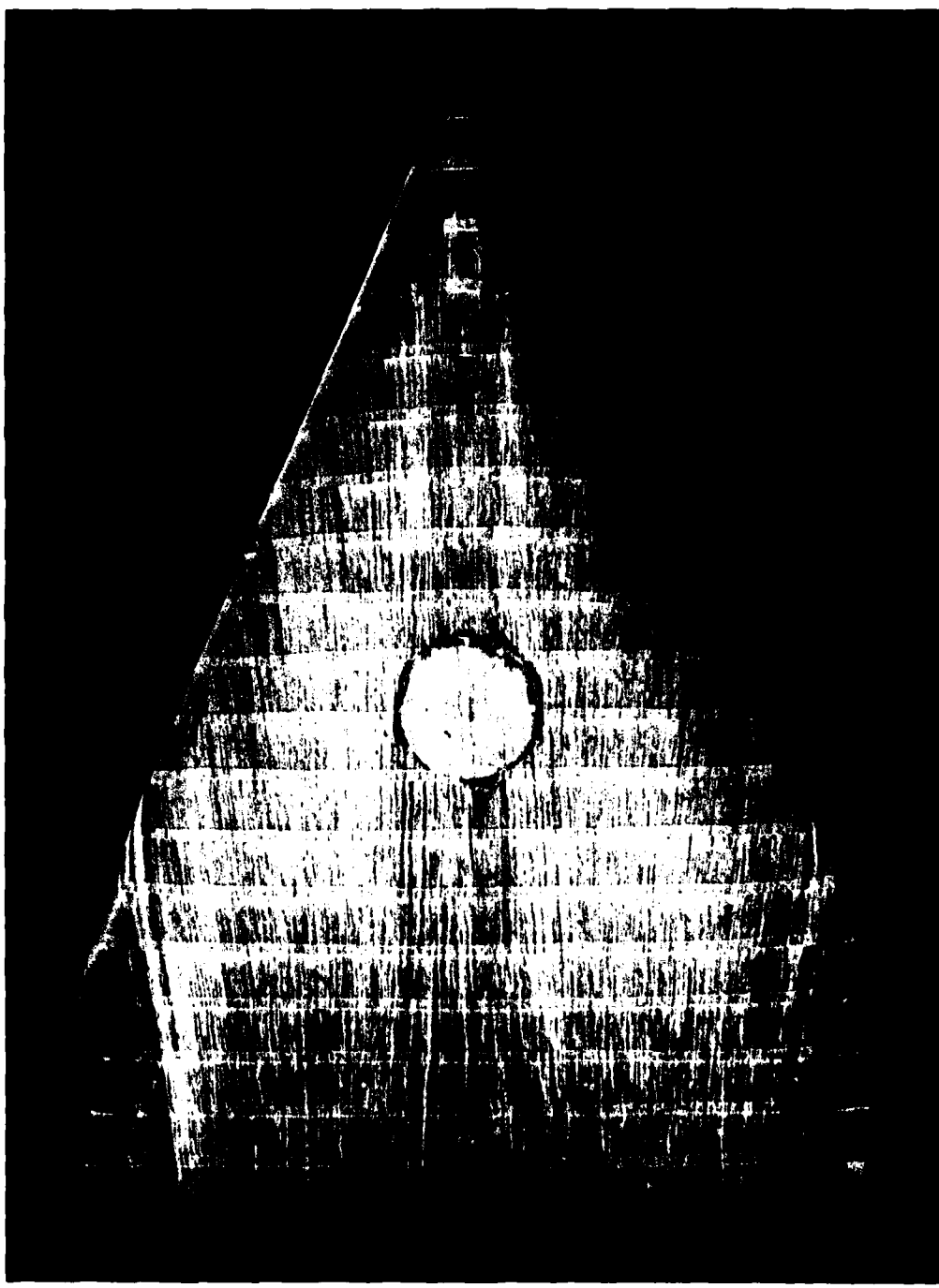


Fig 12a&b Pitching moment variation with lift

**Fig 13**



**Fig 13 Flow pattern on upper surface of the cambered wing  
 $R = 4.0 \times 10^6$ ,  $\alpha = 5.32^\circ$**

Fig 14

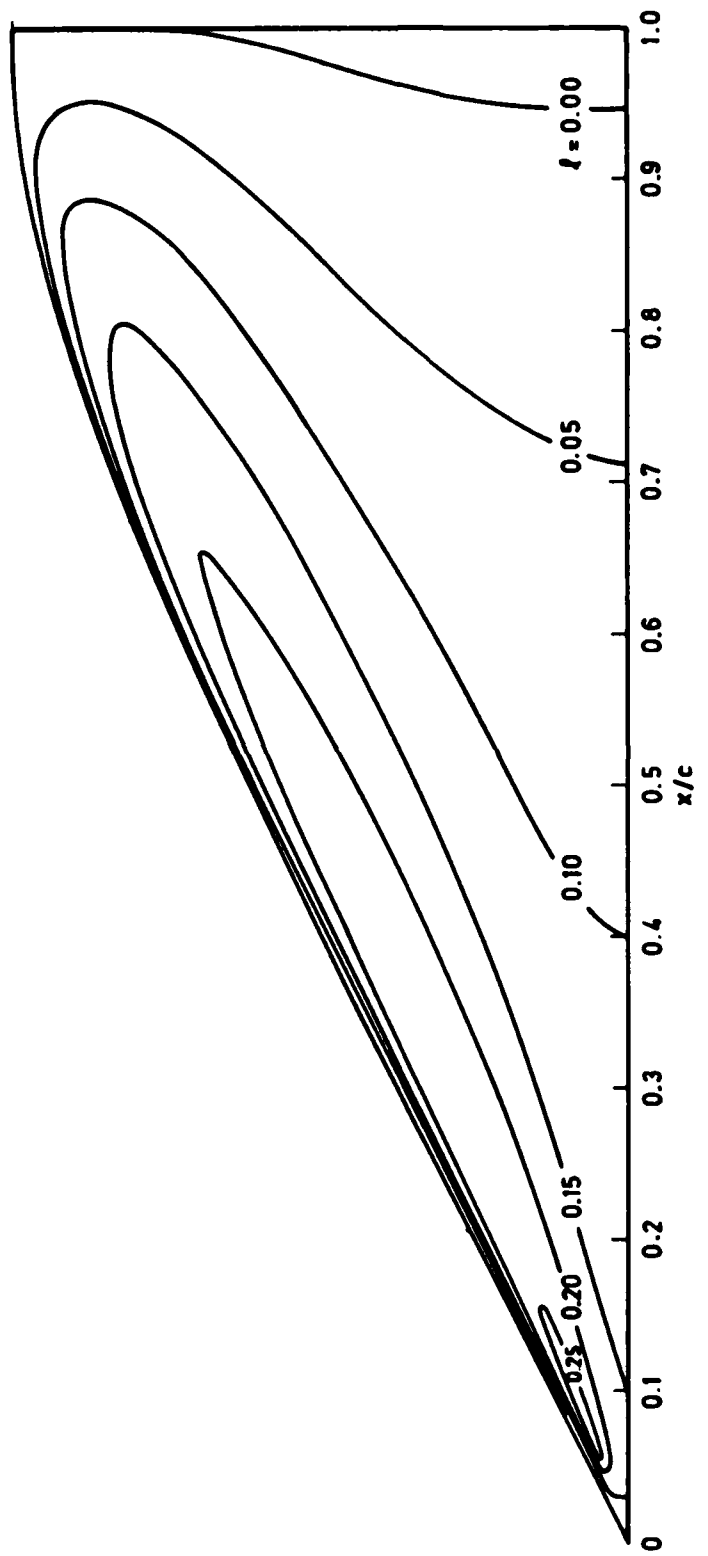


Fig 14 Theoretical loading distribution for attached flow on the cambered wing

Fig 15

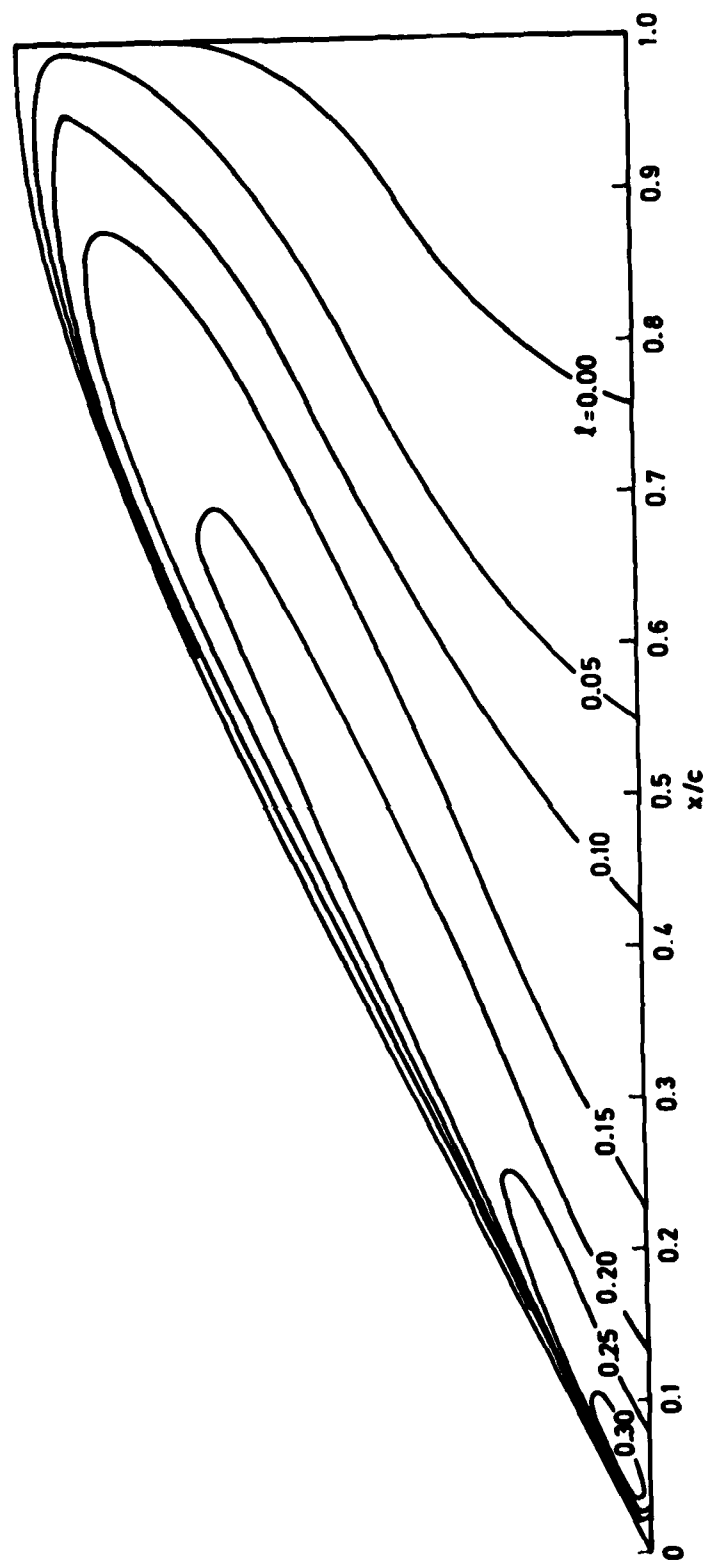


Fig 15 Experimentally determined loading distribution on the cambered wing at  $\alpha_{DES}$

Fig 16a

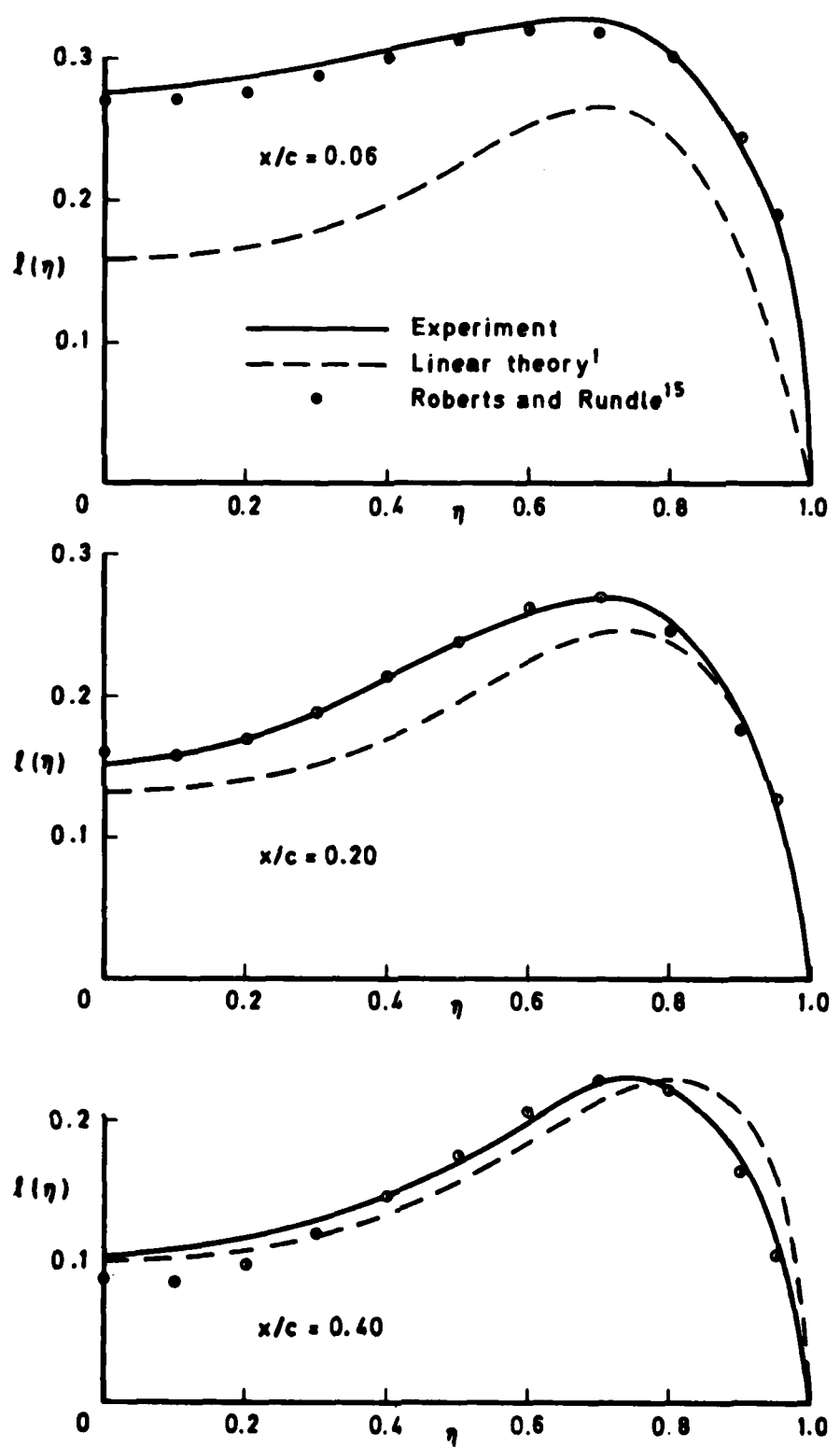


Fig 16a Typical spanwise loading distributions on the cambered wing  
 $\alpha = \alpha_{DES}$ ,  $R = 6.7 \times 10^6$

Fig 16b

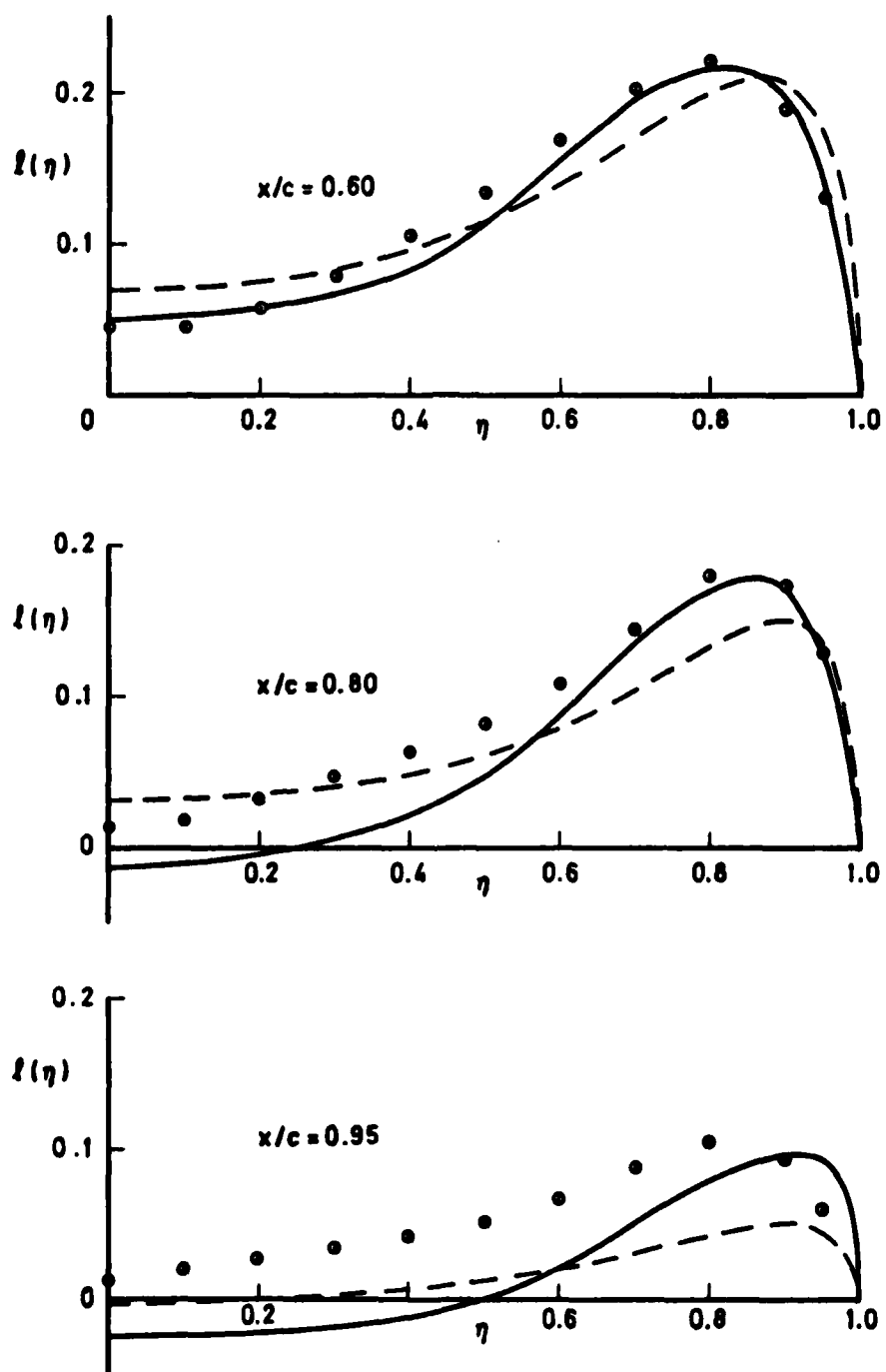


Fig 16b Typical spanwise loading distributions on the cambered wing  
 $\alpha = \alpha_{DES}$ ,  $R = 6.7 \times 10^6$

Fig 17a

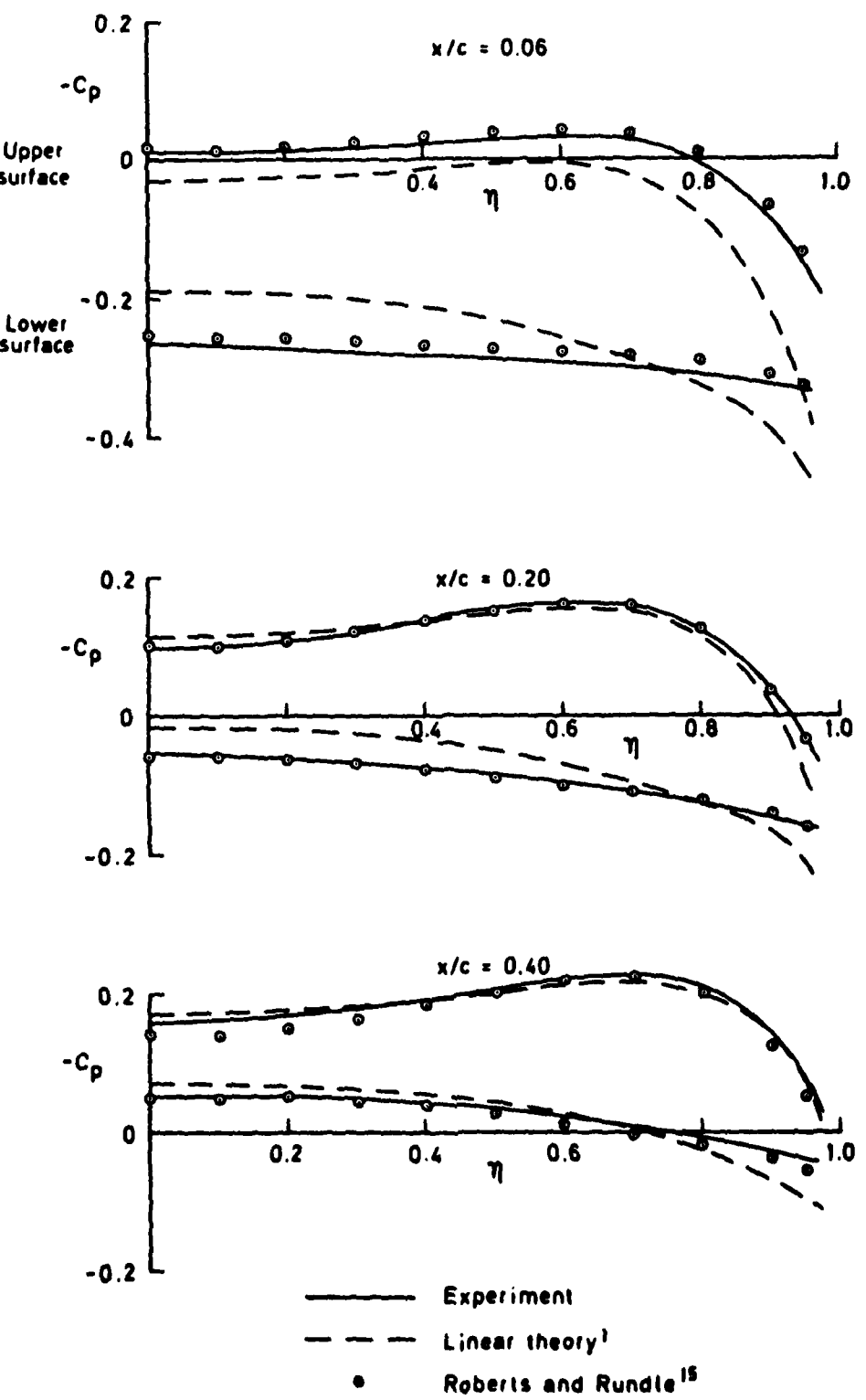


Fig 17a Typical spanwise pressure distributions on the cambered wing  
 $\alpha = \alpha_{DES}$ ,  $R = 6.7 \times 10^6$

Fig 17b

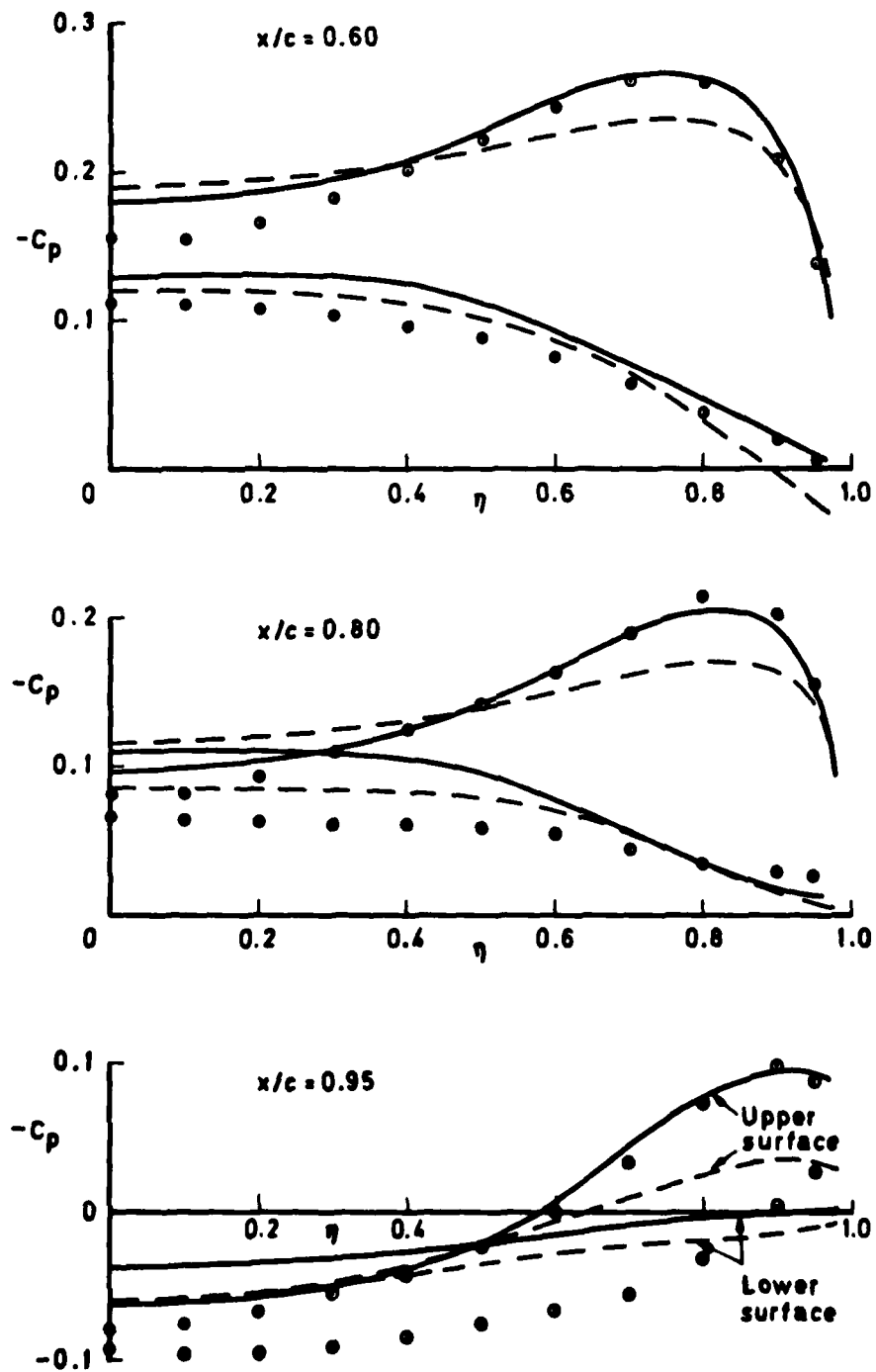


Fig 17b Typical spanwise pressure distributions on the cambered wing  
 $\alpha = \alpha_{DES}$ ,  $R = 6.7 \times 10^6$

Fig 18

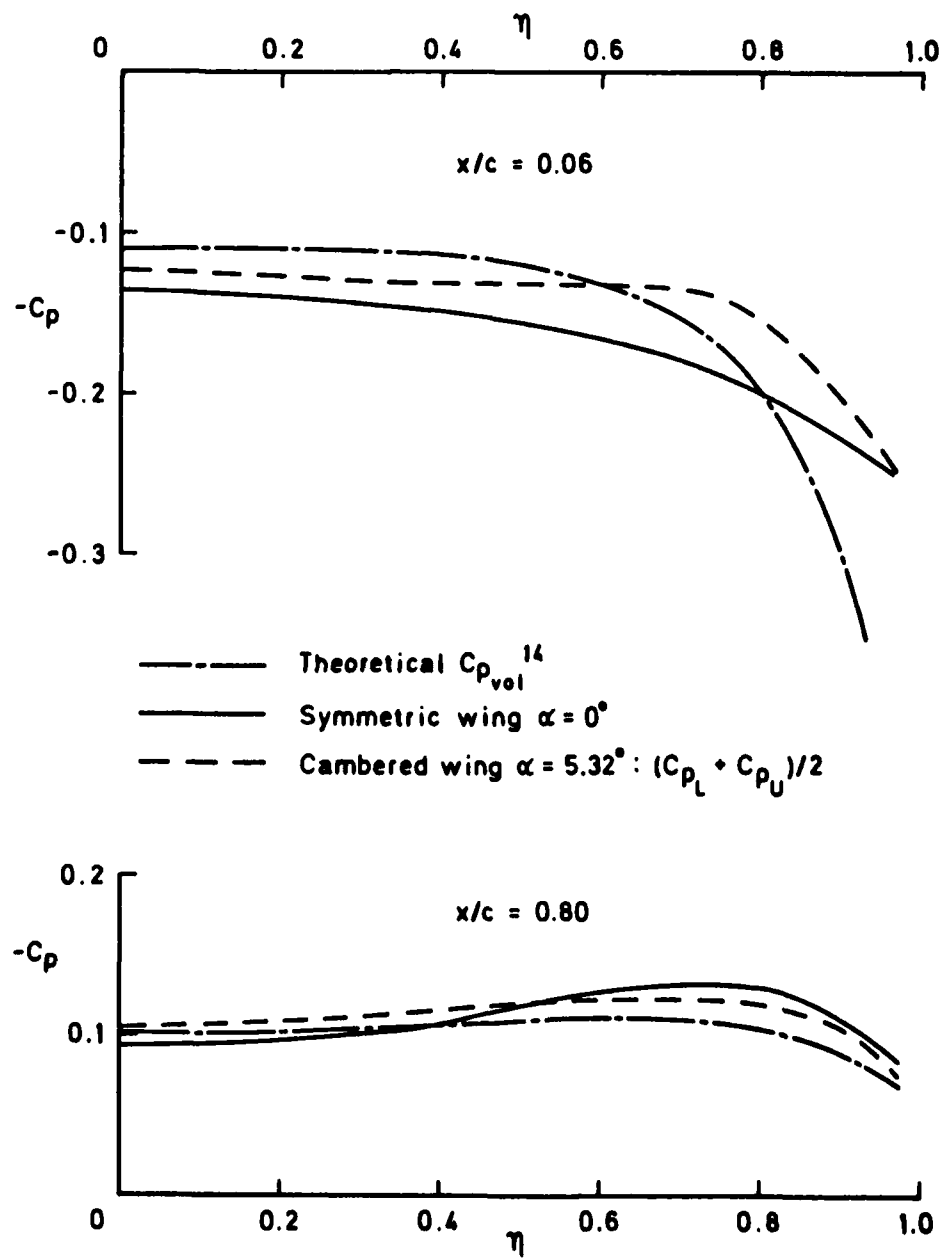


Fig 18 Comparison of measured, estimated and calculated pressure distributions due to volume

Fig 19a

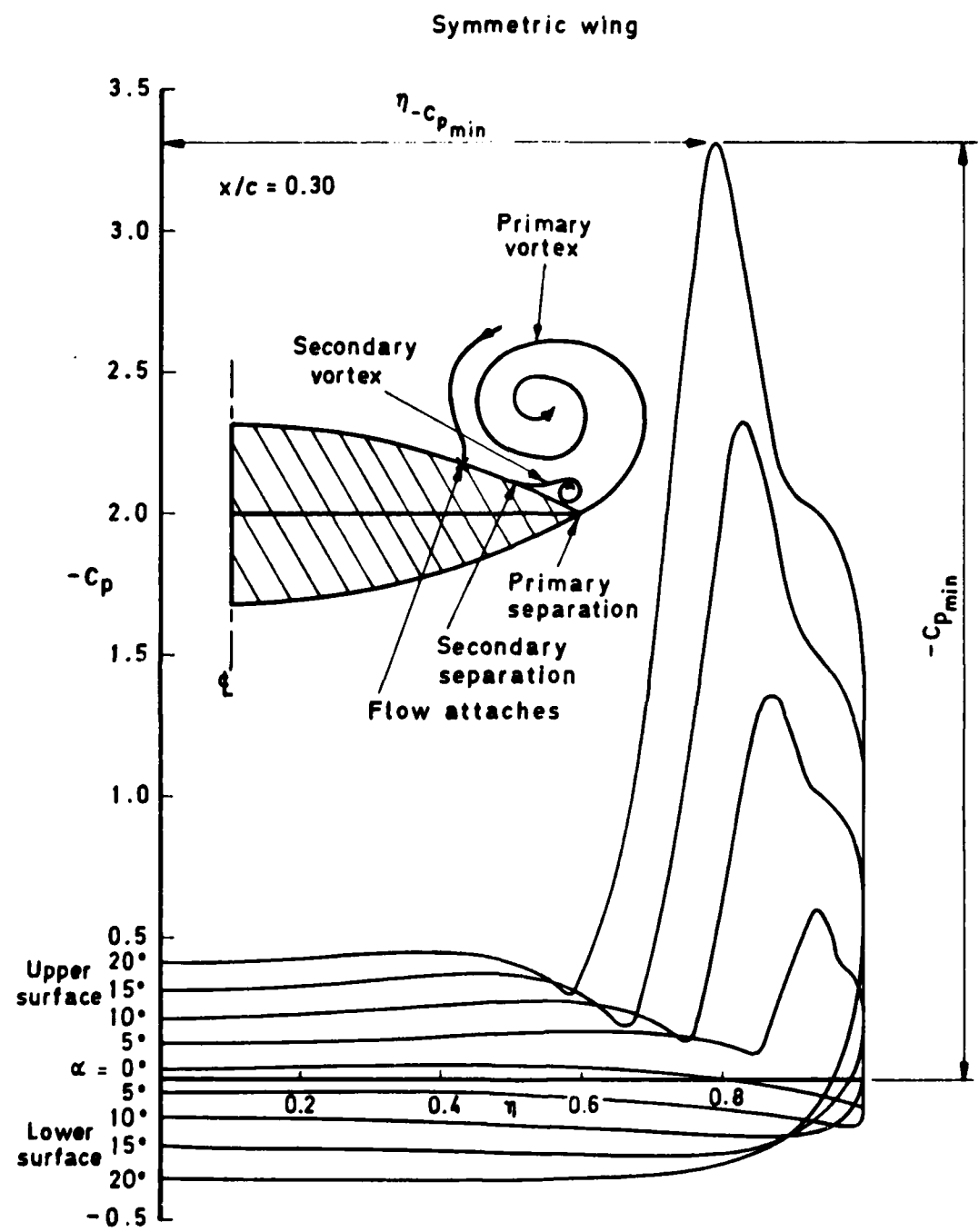


Fig 19a Variation of  $C_p$  distribution with incidence (symmetric wing,  $x/c = 0.30$ )

Fig 19b

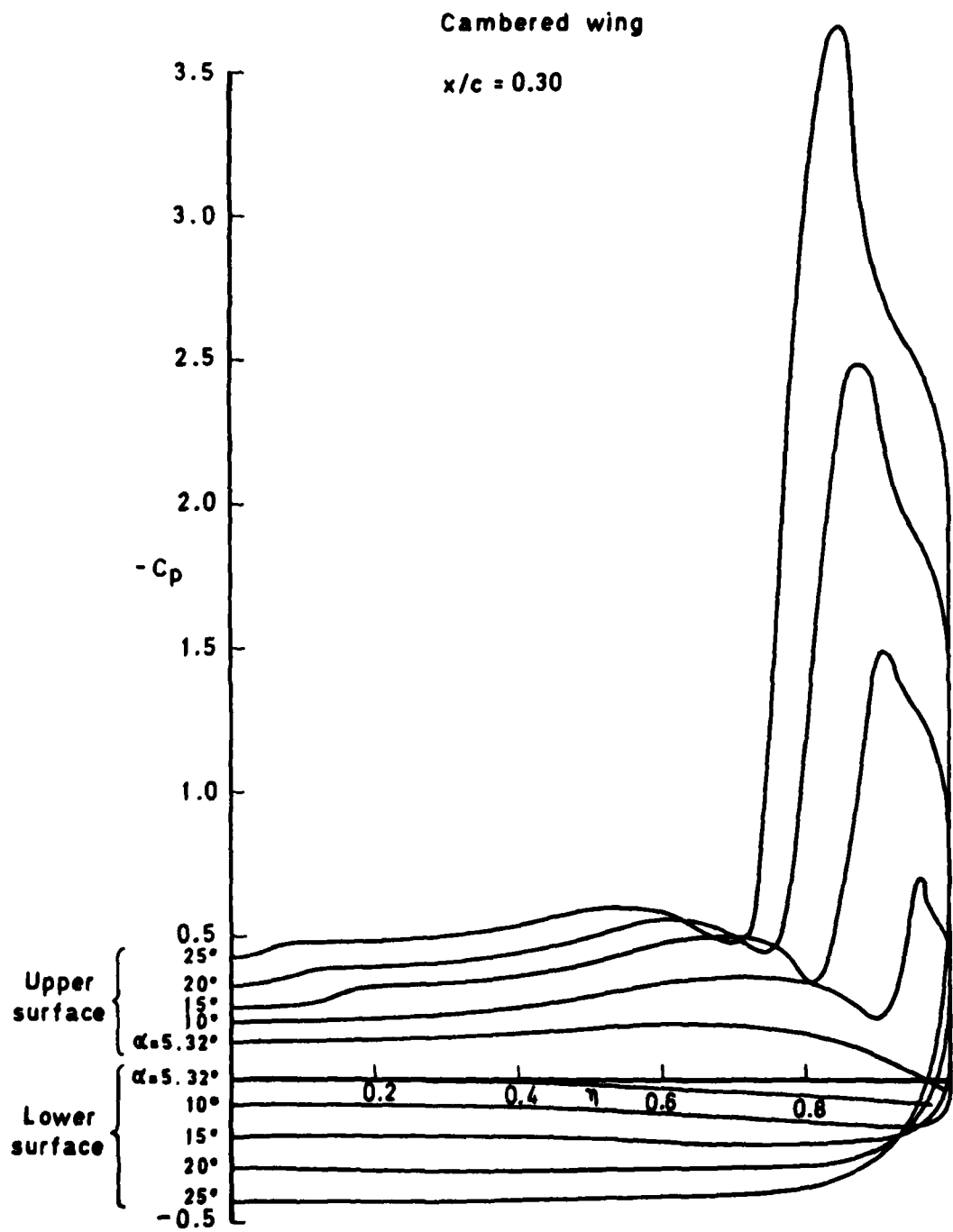
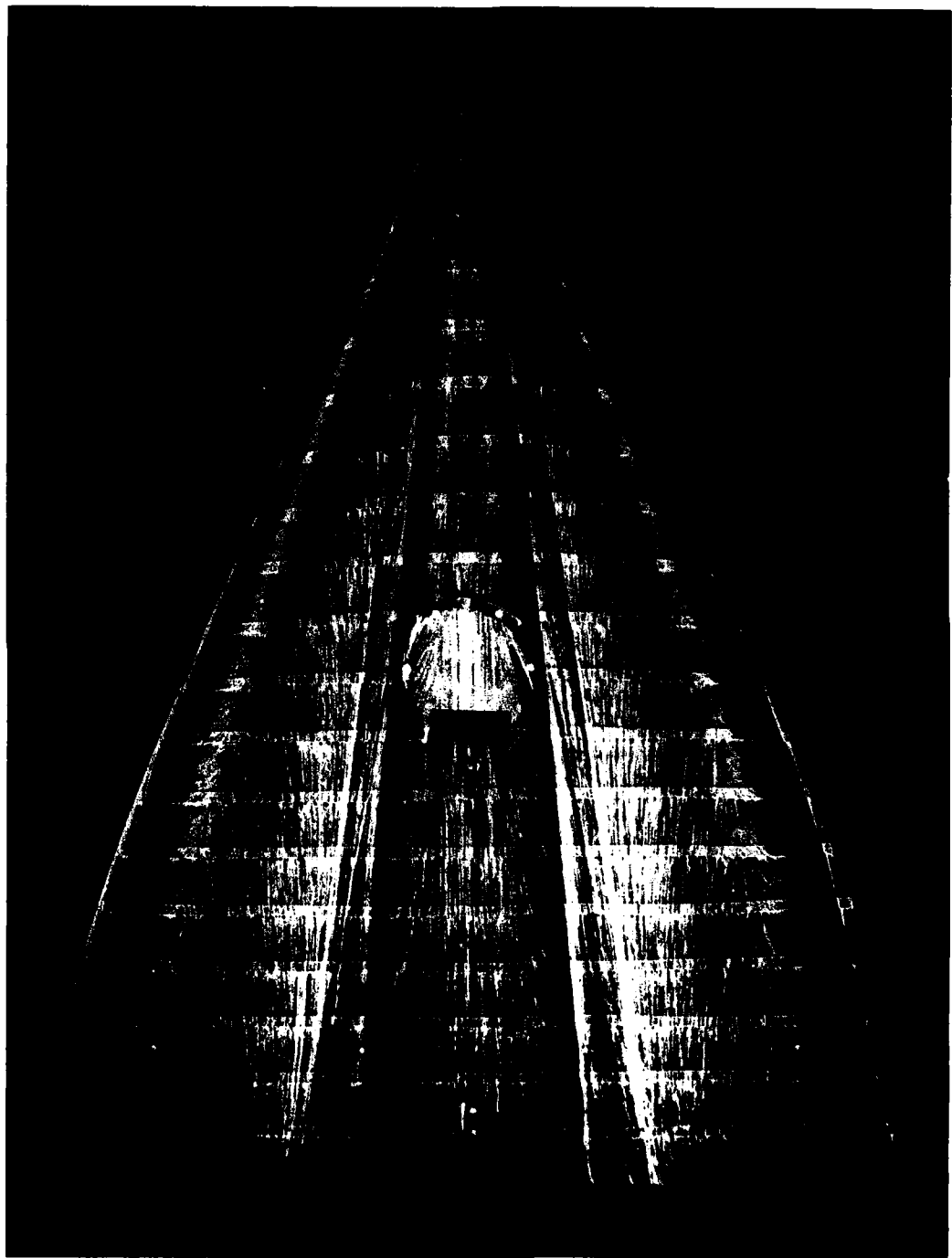


Fig 19b Variation of  $C_p$  distribution with incidence (cambered wing,  $x/c = 0.30$ )

**Fig 20**



**Fig 20 Flow pattern on upper surface of the cambered wing  
 $R = 4.0 \times 10^6, \alpha = 15^\circ$**

Fig 21

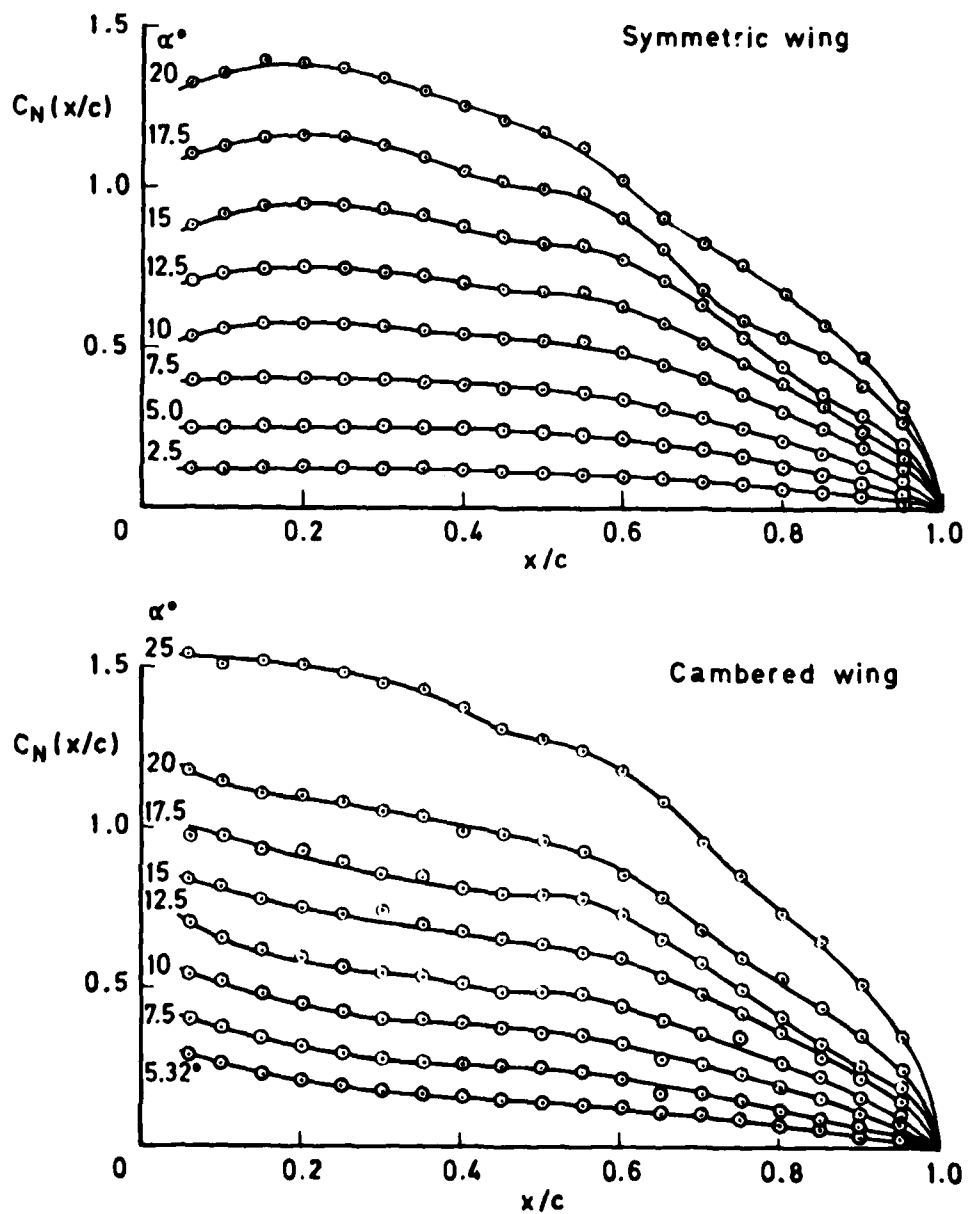


Fig 21 Local normal force characteristics

Fig 22

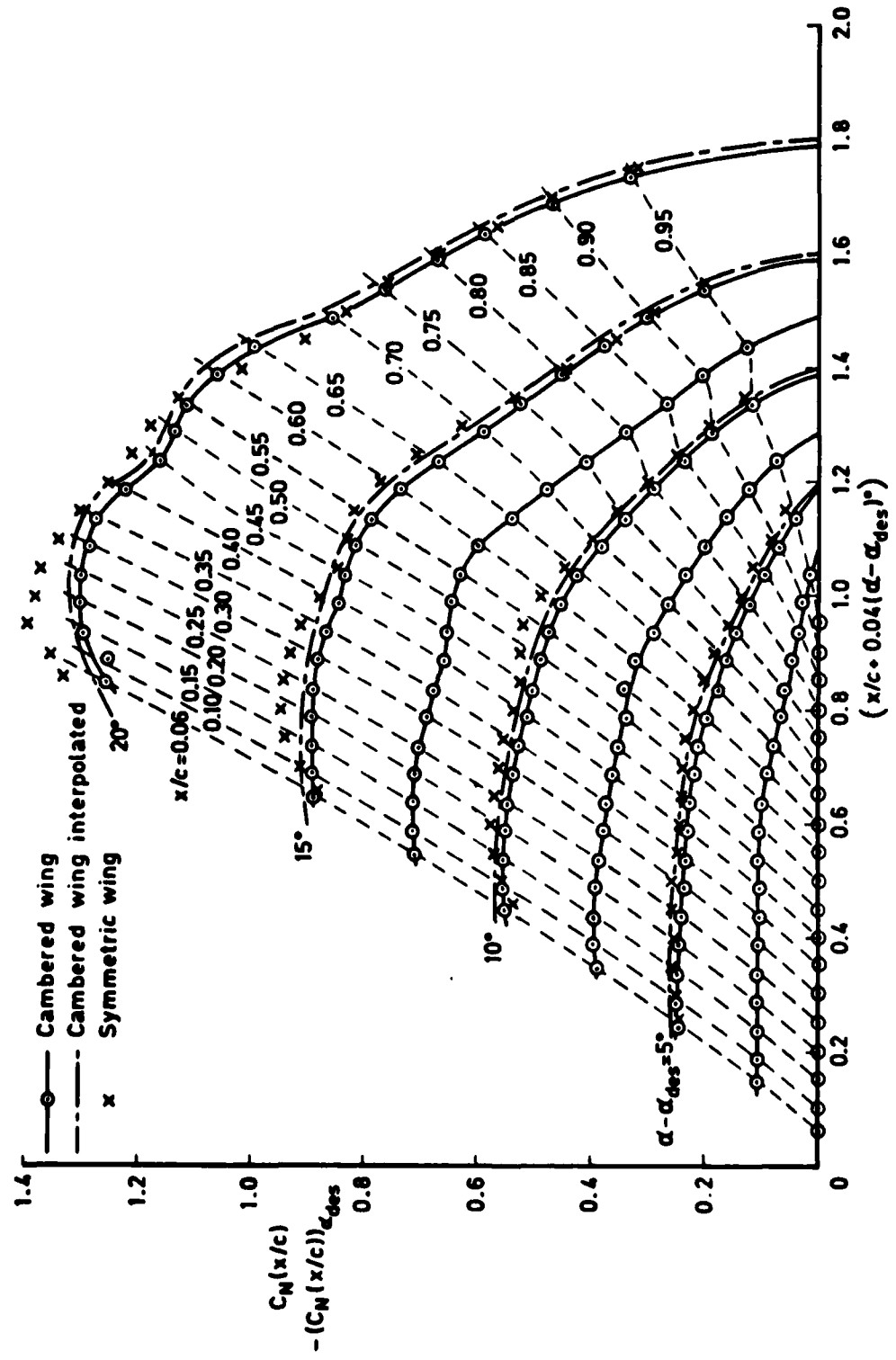


Fig 22 Effect of incidence on local normal force characteristics

Fig 23

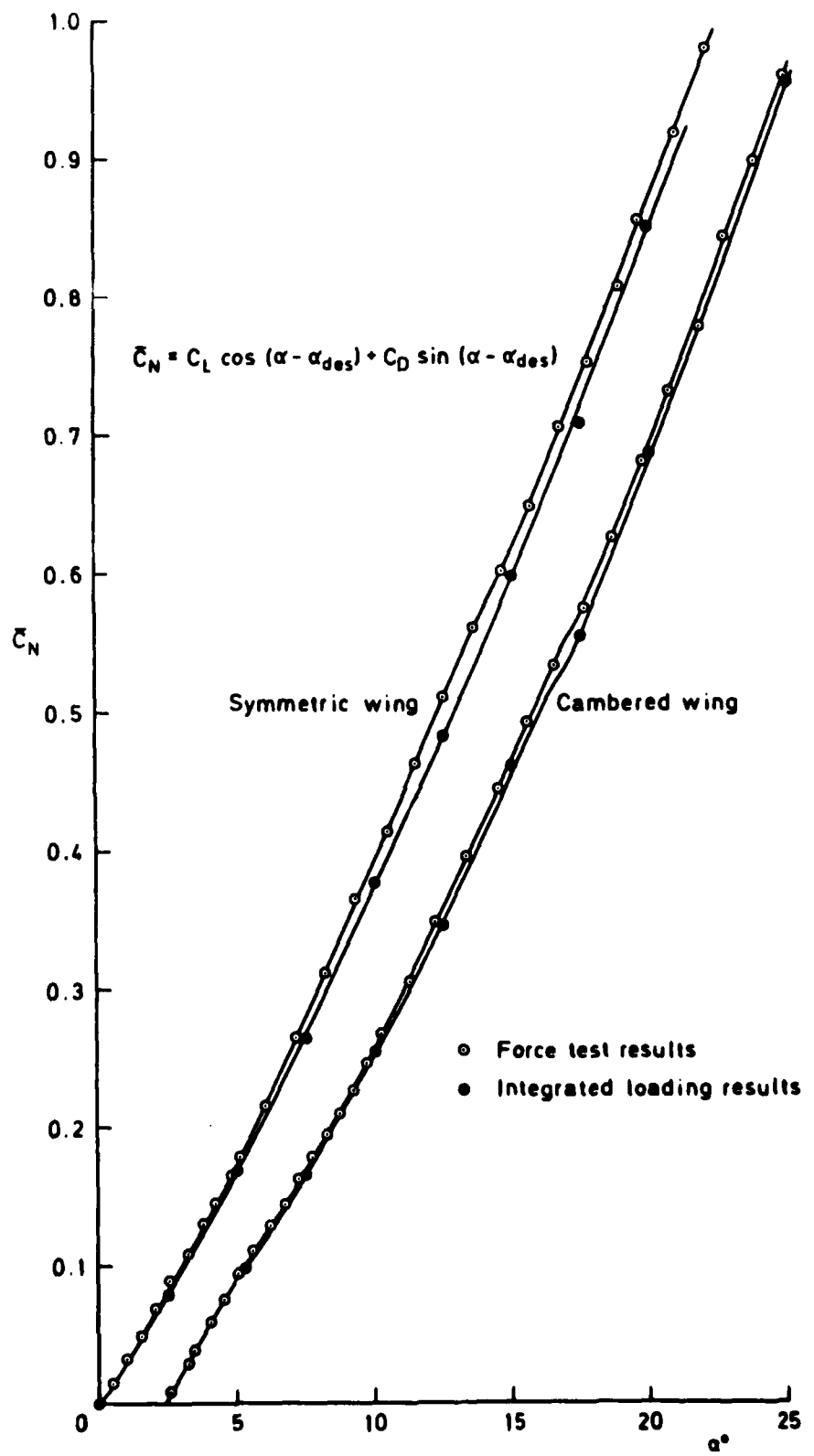


Fig 23 Comparison of normal force characteristics

Fig 24a&b

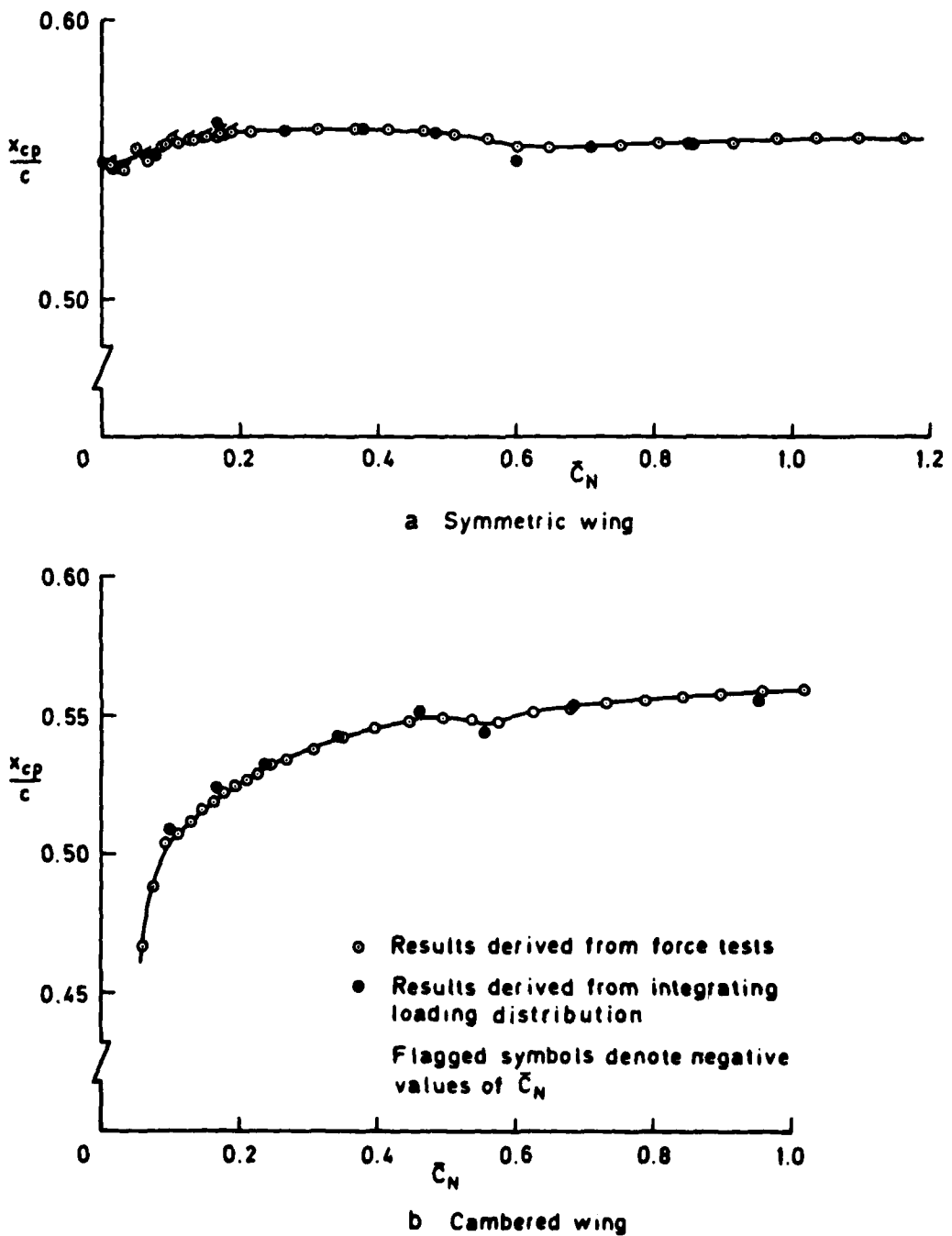


Fig 24a&b Comparison of centre of pressure position

Fig 25

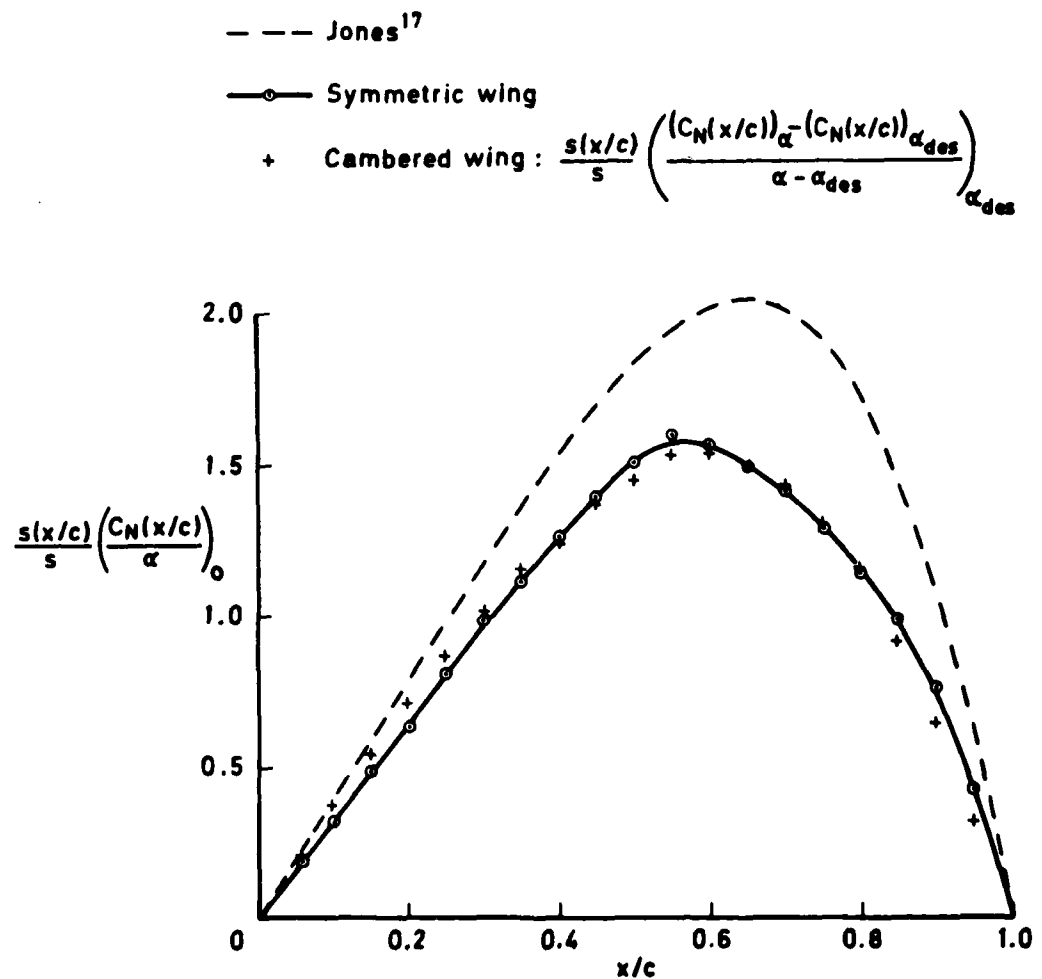


Fig 25 Comparison of linear part of local normal force coefficient

Fig 26

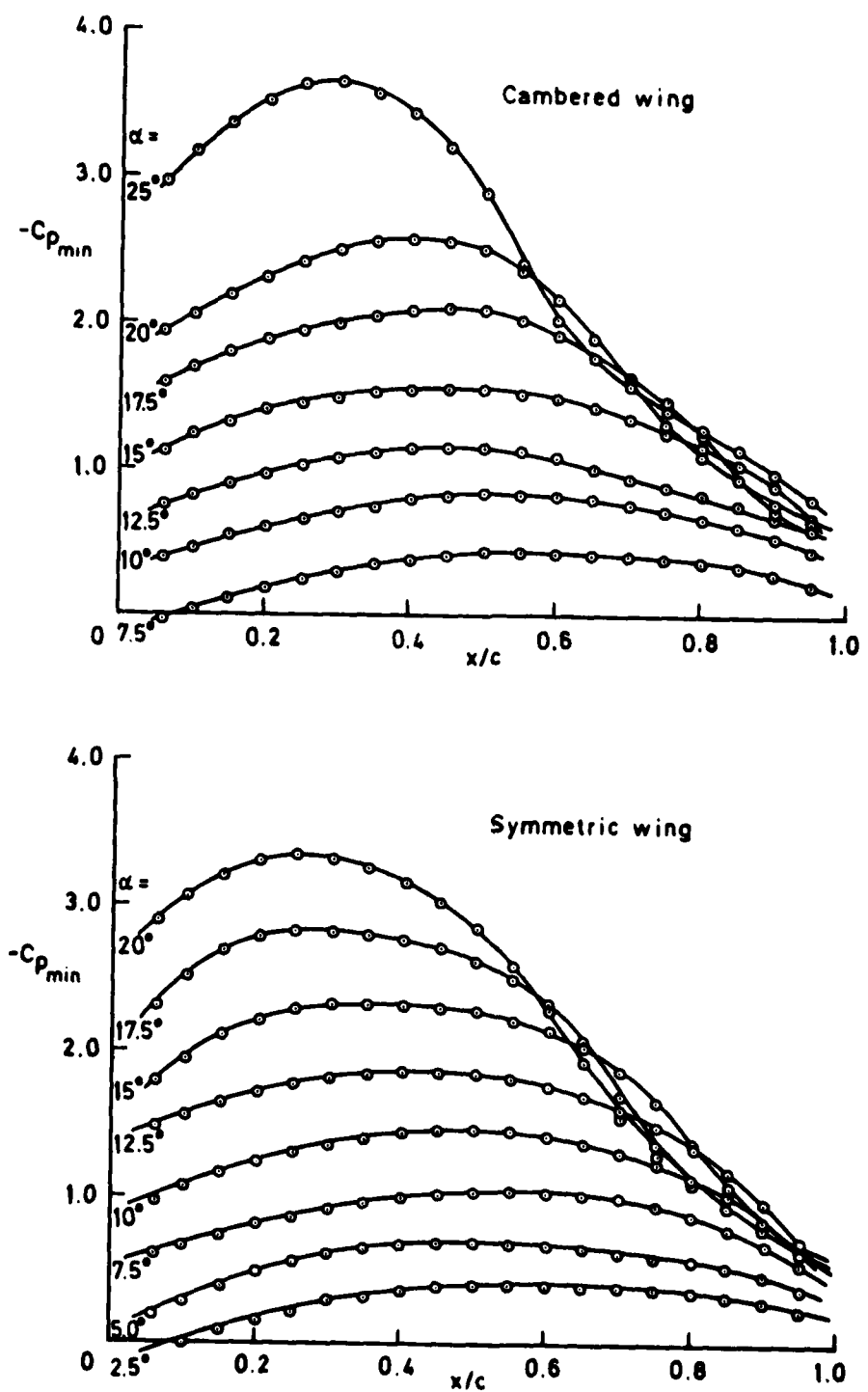


Fig 26 Peak suction on the two wings

Fig 27

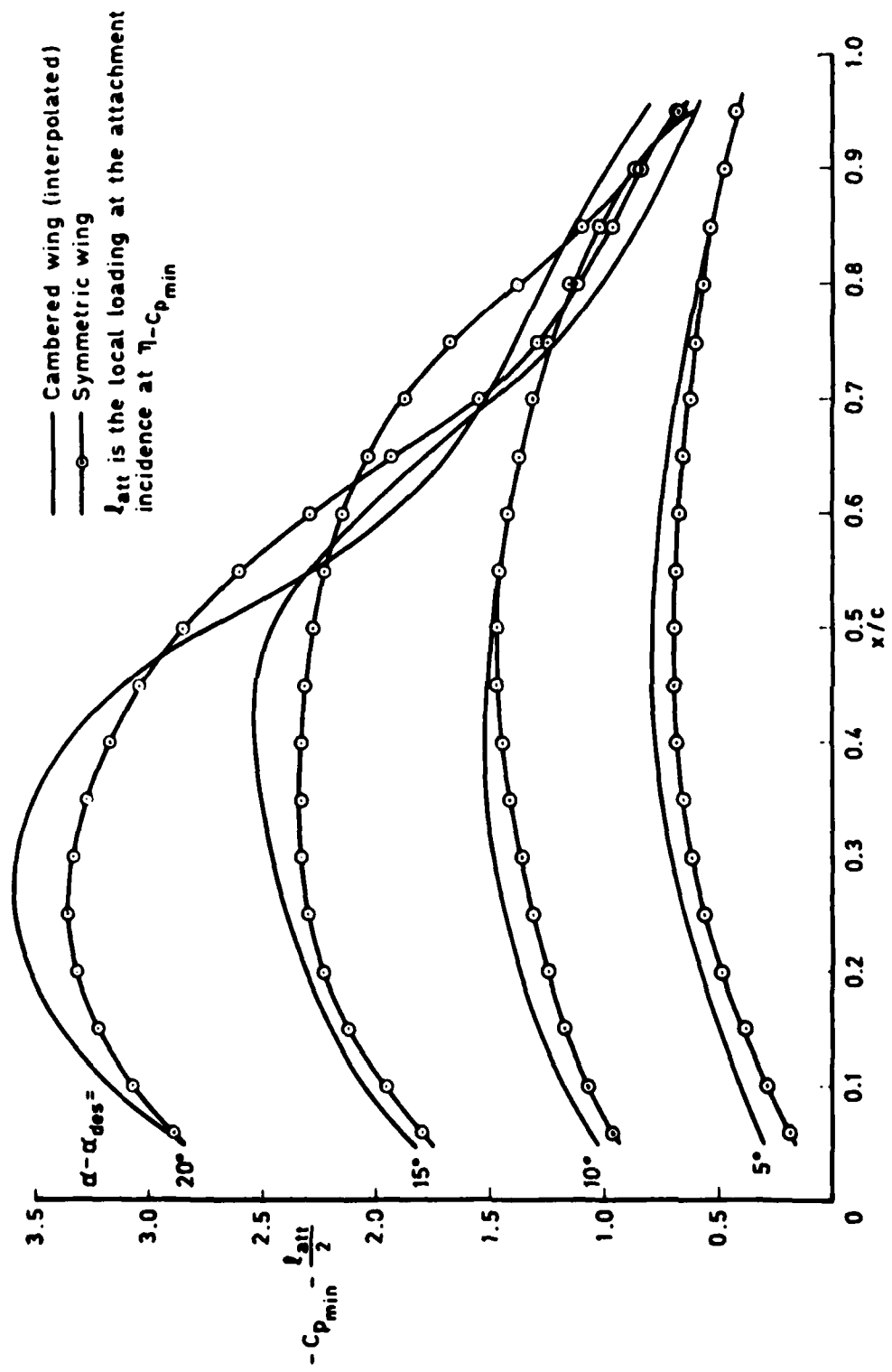


Fig 27 Comparison of peak suctions on the two wings

Fig 28

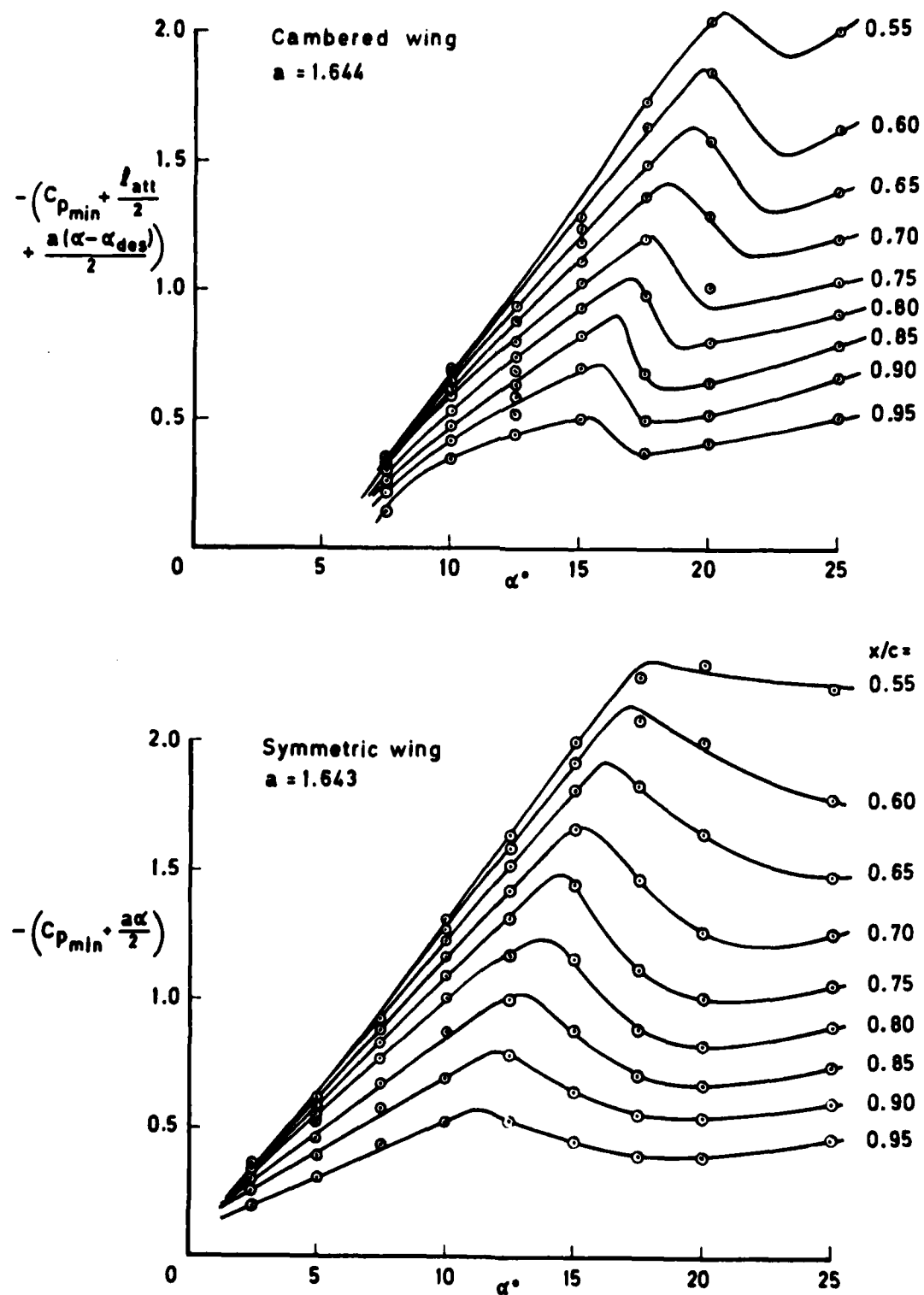


Fig 28 The development of  $-C_{p_{min}}$  with incidence

Fig 29

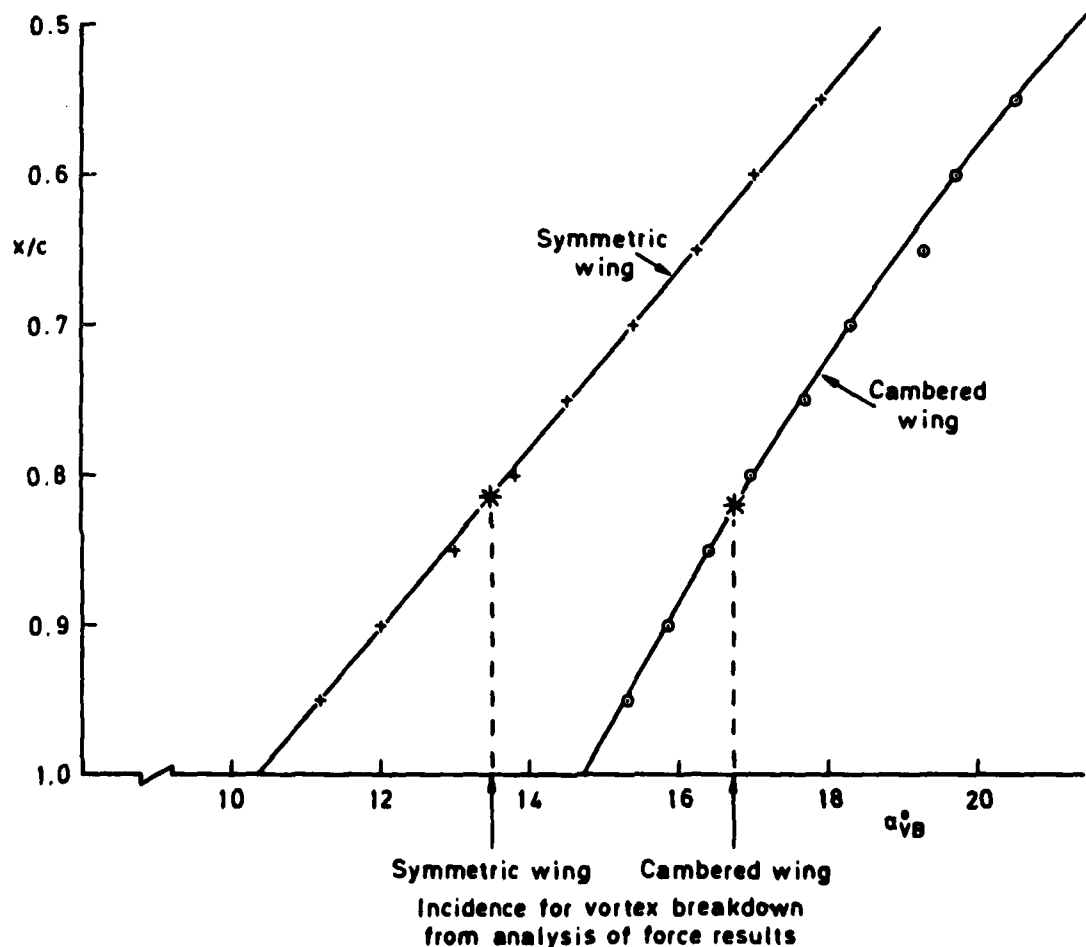


Fig 29 The variation of chordwise position of vortex breakdown with incidence

Fig 30a-c

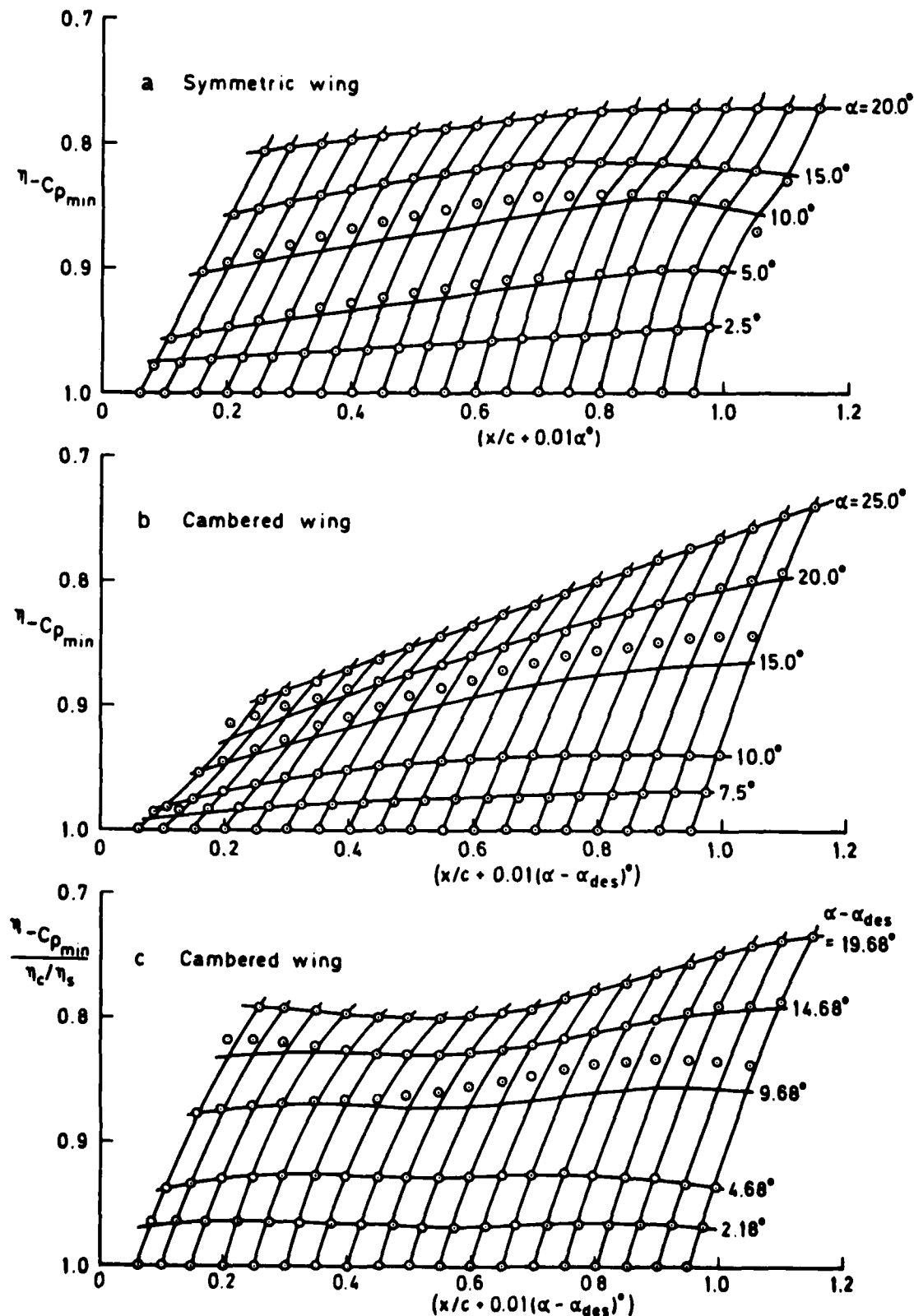


Fig 30a-c Spanwise position of the peak suction

Fig 31

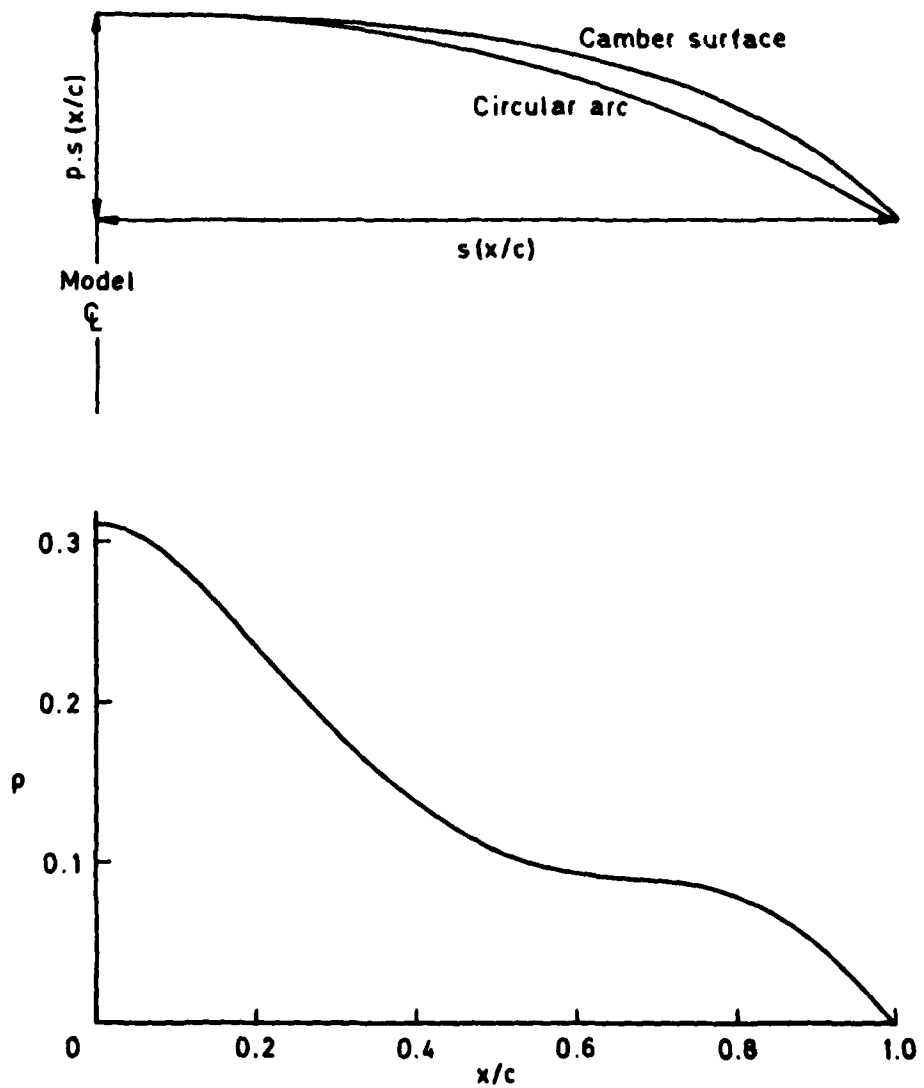


Fig 31 Definition and variation of approximating camber surface parameter  $p$

Fig 32

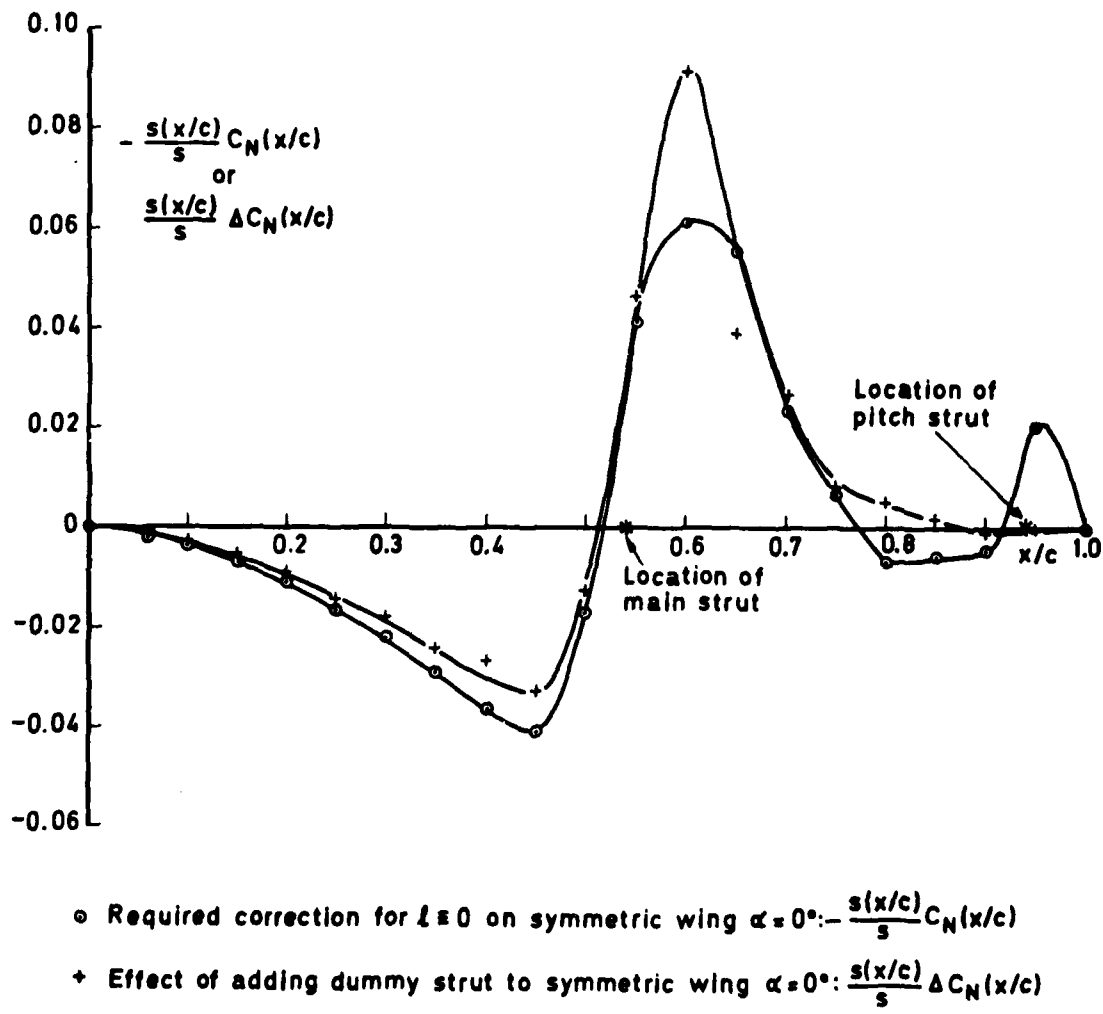


Fig 32 Correction to local normal force coefficient

Fig 33a&b

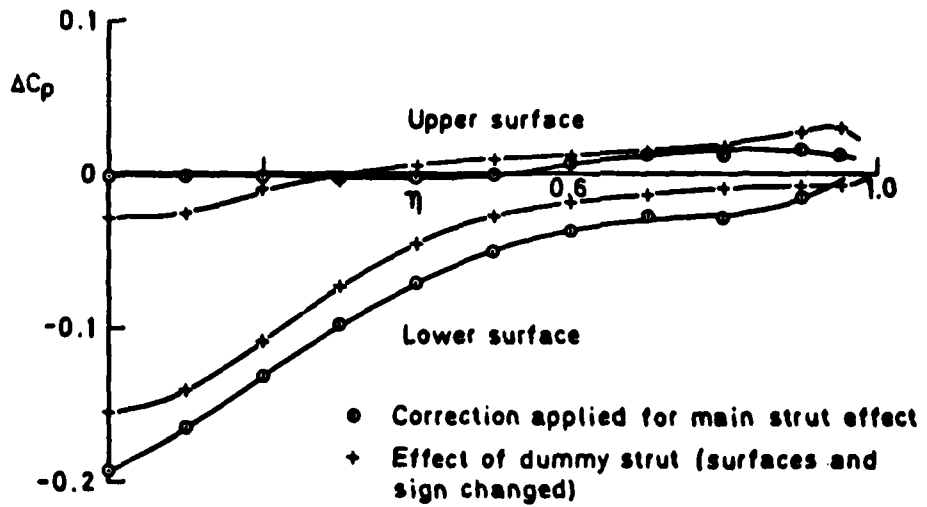


Fig 33a Correction applied to  $C_p$  for  $x/c = 0.45$

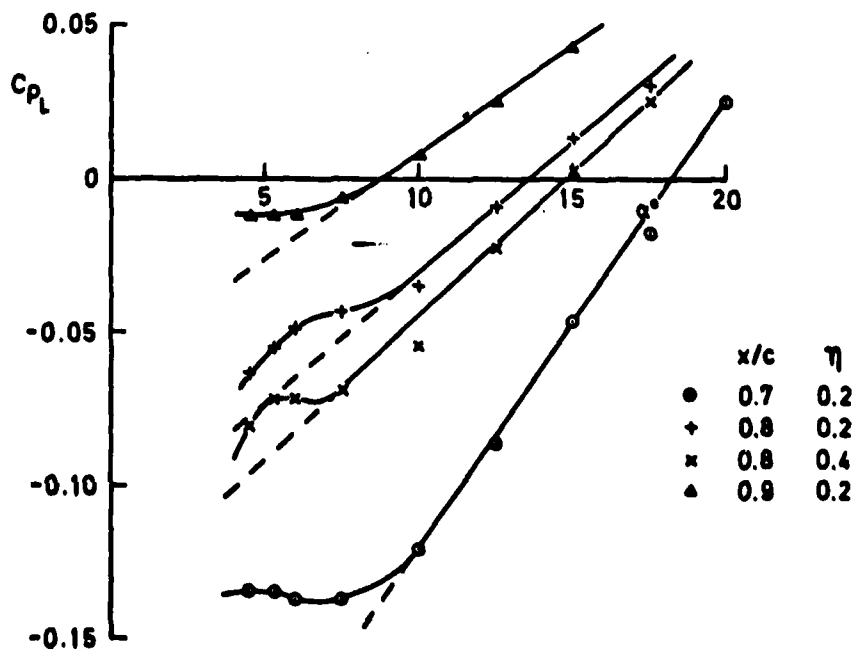


Fig 33b Typical behaviour of  $C_{pL}$  in wake of strut on the cambered wing

REF ID: A10000000000000000000

This form must contain true classified information. If it is necessary to enter classified information, the box  
must be checked and the classification set to Restricted, Confidential or Secret.

1. Report Reference (as used by DRIC)	2. Originator Reference RAE TR 50056	3. Agency Reference N/A	4. Report Security Classification/Marking UNLIMITED
5. Report Grade for Originator 7073000W	6. Originator (Corporate Author) Name and Location Royal Aircraft Establishment, Farnborough, Hants, UK		
5a. Sponsoring Agency's Code N/A	6a. Sponsoring Agency (Contract Authority) Name and Location N/A		
7. Title Low-speed measurements of the static pressure distribution and overall forces on a cambered and a symmetric mild gothic wing of aspect ratio 1.4			
7a. (For Translations) Title in Foreign Language			
7b. (For Conference Papers) Title, Place and Date of Conference			
8. Author 1. Surname, Initials Butterworth, P.J.	9a. Author 2 Dobney, D.G.	9b. Authors 3, 4 ....	10. Date May 1980   Pages 83   Refs. 20
11. Contract Number N/A	12. Period N/A	13. Project	14. Other Reference Nos. Aero 3482
15. Distribution statement (a) Controlled by - Unlimited (b) Special limitations (if any) -			
16. Description (Keywords) (Descriptors marked * are selected from TEST) Blender wings. Pressure distribution. Force measurement. Subsonic wind-tunnel tests.			
17. Abstract A cambered wing of aspect ratio 1.4 has been tested in a low-speed wind tunnel to determine its surface static pressure distribution at its designed, attached-flow camber for comparison with the theoretical loading. To enable the effects of camber on the separated-flow characteristics of this wing to be isolated, the corresponding symmetric wing was also included in the experiments and the results for the two wings are compared and empirical relations derived. The lift, drag and pitching moment characteristics of each wing have also been determined over a range of Reynolds number for comparison with the results of the theoretical analysis and those derived by integration of the measured pressure			